Finite Element Modeling of Vibrations in Canvas Paintings

Patricio Chiriboga

Finite Element Modeling
of Vibrations in
Canvas Paintings

Finite Element Modeling of Vibrations in Canvas Paintings

Proefschrift

ter verkrijging van de graad van doctor
aan de Technische Universiteit Delft,
op gezag van de Rector Magnificus prof. ir. K.C.A.M. Luyben,
voorzitter van het College voor Promoties,
in het openbaar te verdedigen op woensdag 27 maart 2013 om 10.00 uur

door

Patricio Gabriel CHIRIBOGA ARROYO

Mechanical Engineer
Escuela Politécnica Nacional, Quito, Ecuador
geboren te Quito, Ecuador

Dit proefschrift is goedgekeurd door de promotor:
Prof. dr. ir. R. Benedictus

Samenstelling promotiecommissie:

Rector Magnificus,	Voorzitter
Prof. dr. ir. R. Benedictus,	Technische Universiteit Delft, promotor
Prof. dr. N.H. Tennent,	Universiteit van Amsterdam
Prof. dr. J. Dik,	Technische Universiteit Delft
Prof. dr. ir. A. de Boer,	Universiteit Twente
Dr. A.A. de Tagle,	Rijksdienst voor het Cultureel Erfgoed
Dr. ir. W. Wei,	Rijksdienst voor het Cultureel Erfgoed
Prof. dr. T.J. Dingemans,	Technische Universiteit Delft, reservelid

Dr. ir. W. Wei heeft als begeleider in belangrijke mate aan de totstandkoming van het proefschrift bijgedragen.

To the best mom ever!

Contents

List of Figures

List of Tables

Nomenclature

Roman Symbols

A	Cross-section area of power screw	[mm^2]
Ay_1, Ay_2	Cross-section area of weft and warp yarns	[mm^2]
A_{ij}	Stretching stiffness coefficients	[N/mm]
B_{ij}	Coupling stiffness coefficients	[N]
C_{ij}	Stiffness coefficients	[MPa]
D_{ij}	Bending stiffness coefficients	[N.mm]
E	Young's modulus isotropic material	[MPa]
E_1, E_2	Young's modulus in weft and warp directions	[MPa]
$E_{45°}$	Young's modulus at 45°	[MPa]
E_ϕ	Young's modulus at an angle ϕ	[MPa]
F	Force	[N]
G	Shear modulus isotropic material	[MPa]
G_{12}	In-plane shear modulus for canvas plate	[MPa]
G_{13}, G_{13}	Transverse shear moduli for canvas plate	[MPa]
H_i, H_o	Exterior and interior width of beam section	[mm]
I	Moment of inertia of beam section	[mm^4]
J	Sampling interval	[s]
L	Length of beam in support frame	[mm]
M_x, M_y	Bending moment intensities per unit length	[N]
M_{xy}, M_{yx}	Twisting moment intensities per unit length	[N]
N_x, N_y	Normal force intensities per unit length	[N/mm]
N_{xy}, N_{xy}	Shear force intensities per unit length	[N/mm]
N_1, N_2	Yarn count in weft and warp	[#/cm]
P_f	Fiber packing factor in yarn	[—]
P	Surface load	[N]
Q_{ij}	Reduced stiffness coefficients	[MPa]
R	Electrical resistances in strain gauges	[Ω]

S_1, S_2	Weft and warp yarn spacing	[mm]
Sy	Yield strength	[MPa]
T	Torque in power screw to apply stretching	[N.mm]
W	Arbitrary scaled amplitude	[mm]
V_{RUC}	Volume of Representative Unit Cell	[mm³]
V_{f1}, V_{f2}	Volume fraction of weft and warp yarns	[—]
Vy_1, Vy_2	Volume of weft and warp yarns in RUC	[mm³]
V_{ex}, V_{out}	External and output voltages	[V]
Y	Distance measured on yarn removed from textile	[mm]
Y_o	Distance measured on yarn in textile	[mm]
Y_{max}	Maximum deflection in beam for support frame	[mm]

a, b	Length and width of painting and plate model	[mm]
c_1, c_2	Yarn crimp in weft and warp	[—]
d	Diameter of circular yarn	[mm]
d_r	Root diameter of power screw	[mm]
d_m	Mean diameter of power screw	[mm]
e, g	Width and height of lentil shaped yarn	[mm]
f	Frequency	[Hz]
f_{dr}	Driving frequency of acoustic excitation	[Hz]
f_o	Initial frequency of acoustic excitation	[Hz]
f_s	Sampling frequency for laser vibrometer	[Hz]
h	Thickness of painting and plate model	[mm]
i, j, k	Integer numbers	[—]
h_m	Assumed thickness for plate model	[mm]
h_n	Nominal thickness of the textile	[mm]
h_{e1}, h_{e2}	Effective thickness of plate for weft and warp	[mm]
l_1, l_2	Length of weft and warp yarns in RUC	[mm]
m, n	Wave numbers in x and y respectively	[—]
n_t	Number of engaged threads in power screw	[—]
$\bar{m}$	Mass per surface area	[gr/mm²]
p	Pitch of thread in power screw	[mm]
r	Textile fiber radius	[mm]
t	Time	[s]
u, v, w	Displacement components in x, y and z	[mm]
x, y, z	Cartesian coordinate system	[mm]

Greek Symbols

β_x, β_y	Rotations of plate relative to x and y	[rad]
γ_{xy}	Shear strain in x-y coordinates	[—]
γ_{12}	Shear strain in material coordinates	[—]
δ	Displacement	$[mm]$
ϵ_x, ϵ_y	Extensional strains in x and y coordinates	[—]
ϵ_1, ϵ_2	Extensional strains in material coordinates	[—]
ζ	Damping ratio	[—]
θ	Thread angle in power screw	[°]
$\kappa_x, \kappa_y, \kappa_{xy}$	Curvatures and twisting curvature	$[\text{mm}^{-1}]$
μ	Friction coefficient	[—]
ν	Poisson's ratio of isotropic material	[—]
ν_{12}, ν_{21}	Poisson's ratios in material coordinates	[—]
σ_1, σ_2	Stress components in material coordinates	[MPa]
σ'	von Mises stress	[MPa]
τ_{xy}, τ_{yx}	Shear stresses in x-y coordinates	[MPa]
τ_{12}	Shear stress in material coordinates	[MPa]
ϕ	Angle from principal material coordinate	[°]
Φ	Eigenmode	[mm]
ω	Angular frequency	[rad/s]

Abbreviations

CF	Concentrated Force
CLT	Classical Laminate Theory
DOF	Degrees of Freedom
FE	Finite Element
HPBW	Half-Power Band Width
MAC	Modal Assurance Criterion
RP	Reference Point
RUC	Representative Unit Cell
SD	Standard Deviation
SF	Safety Factor

Chapter 1

Introduction

"No permanent collection is ever rich enough to represent an artist, period or style." This quotation from the New York Times by Philippe de Montebello, the former director of the Metropolitan Museum of Art in New York [5], demonstrates the need for major museums to borrow important works from other museums in order to enhance their temporary exhibitions, and attract larger numbers of visitors and press coverage. This trend has dramatically increased the number of requests for loans, in particular of paintings, for exhibitions worldwide in recent years.

The transport of paintings to and from exhibitions requires appropriate procedures in order to reduce the risks and hazards involved in the transit process. Vibrations are one of the many factors which need to be considered when shipping a painting, others being, for example, humidity, temperature and light. The concern with vibrations is that they could cause cracking of paint layers or even paint loss from the canvas. Consequently, proper packing and handling of paintings are required in order to protect them. Although one of the main concerns for museums is vibration exposure during transport, the exposure of paintings in exhibitions or in storage to vibrations caused by nearby construction work, road traffic or loud concerts is also a concern.

Many of the decisions and precautions currently taken to mitigate the effect of vibrations, and define tolerable vibration levels are based on an insufficient understanding of the nature of the problem in the cultural heritage world. A key problem is that in the cultural heritage literature the terms "shock" and "vibration" are usually confused. Many investigators measure and account for shock as the most relevant cause of damage in paintings, ignoring all other vibration effects. This would seem to be somewhat intuitive because the damage produced by shock is usually immediate and evident, for instance, an

impact on the corner of the frame of a painting. In contrast, canvas vibrations such as those induced by road transport, produce small cyclic loads, far below the strength of the material. These loads could cause long-term, cumulative damage which is initially not visible. Furthermore, most previous studies performed measurements on everything except the object itself. Vibration data coming from the painting frame, packing case or museum wall provide little information about the actual behavior of the canvas. The main reason is that conventional measuring devices (accelerometers) may not be attached to the surface of interest, due to the potential damage caused by gluing an object to the canvas. Technically viewed, this would also increase the mass of the canvas locally, thus changing its dynamic behavior. Appropriate measurements could be performed on the canvas itself by using non-contact vibrometers, but mounting these is also not easy.

There is thus an insufficient understanding about the actual vibration behavior of the canvas and its relation to the damage produced in the paintings in the cultural heritage world. Systematic research in this area is needed in order to determine allowable vibration levels and provide guidelines to assist museums and conservators in the care of their collections. The ultimate objective of this work is to characterize and predict the damage produced on sensitive canvas paintings under vibration loading.

A "sensitive" canvas painting is defined for this study as one with cracked paint layers and aged materials. For the majority of traditional oil paintings on canvas, the surface is covered by transverse cracks (craquelure) forming a field of paint "flakes" which can become "loose" from the canvas. In this state the painting can be very susceptible to damage due to the brittleness of the paint layers and stress concentrations at the delamination crack fronts. The vibratory movement of the canvas produces cyclic opening and closure of the interfacial cracks causing them to grow progressively with each vibration event. This can eventually lead to paint loss and a decrease in the "readability" of the painting.

An investigation is being conducted by the Cultural Heritage Agency of the Netherlands, the former Netherlands Institute for Cultural Heritage, in order to develop a model capable of predicting the damage accumulation produced on sensitive canvas paintings by vibration loading. The ultimate goal is to provide guidelines to assist museums, collections, and art conservation institutions on assessing the risks involved in the exposure of their collections to vibration sources. The modeling tasks involve a characterization of the global vibration behavior of canvas paintings, and a characterization of the delamination growth in the paint layers to predict when, for example, a flake of paint is going to fall off.

The present investigation was focused mainly on developing a model to predict the global dynamic behavior of traditional oil on canvas paintings using Finite Element (FE) methods. Experiments were carried out to verify and optimize the model. This included measurement of the mechanical properties of the canvas and paint materials in order to obtain proper input material data for the model. The local damage model is beyond the scope of this project.

This investigation is presented in this thesis, which is arranged as follows: In Chapter 2 the existing literature is reviewed on the topics of canvas painting materials and techniques, mechanics and aging of paintings, vibration and modeling of paintings and textiles. Chapter 3 presents the development of the FE vibration model for canvas paintings. This includes a description of an initial analytical model on which the FE model is based and the assumptions for modeling the canvas textile as a homogeneous plate. Chapter 4 describes the test setup, equipment and procedure for the experimental verification of the FE model. In Chapter 5 the main experimental results are reported in conjunction with the results of model prediction in order to compare them. The interpretation of the results, model optimization and discussion are presented in Chapter 6. Finally, the main conclusions of this investigation and recommendations for future research are presented in Chapter 7. Appendix A contains a detailed derivation of the analytical model. A short introduction to the finite element method with emphasis on dynamics and vibrations is given in Appendix B. Appendix C describes the convergence analysis of a simple FE model towards the analytical solution. The tensile testing of paint films to measure the elastic moduli of the ground materials is found in Appendix D. The design details of the biaxial frame built to stretch the canvas specimens are discussed in Appendix E. A description of the relaxation tests that were carried out on canvas textiles are given in Appendix F. In Appendix G, the main mode shapes are shown with their corresponding analytical derivation in order to compare them with shearography results.

Chapter 2

Literature Review

Paintings are complex inhomogeneous structures composed of several materials which can change significantly with age. A wide variety of materials and techniques have been applied depending on the artist's period or style, making it difficult to characterize a general class of paintings. For this reason, the first part of this chapter presents a description of traditional materials and techniques used in paintings with special emphasis on oil on canvas. Then, the main mechanisms involved in the aging of paintings are described, with particular regard to vibrations. Finally, a review of the literature concerning modeling trends for paintings, textiles and thin structures is given. This thesis concentrates on modeling the vibration behaviour of aged canvas paintings.

2.1 Painting Materials and Techniques

A painting consists basically of a support and the paint layers that form the image. The support of a painting is the structural material upon which the paintings is made. The most common supports are canvas, wood panels, cardboard, and paper [6]. This thesis concentrates on canvas which is a very common support for oil paintings. Canvas is a heavy, strong textile manufactured by interlacing two sets of yarns that run perpendicular to each other, in the so-called weft and warp directions [7, 8]. The warp yarns are stretched on a loom and they are lifted alternately so that the weft yarns, carried by a shuttle, can be woven under and over the warp yarns. The manufacturing process produces crimp (waviness) in the weft and warp directions, and causes flattening of both yarns. However, the warp yarns are stretched and forced to bend around the weft yarns which causes the warp yarns to become more crimped and flattened than the weft yarns [9].

The yarns for canvas textiles are manufactured by spinning together natural plant fibers such as cotton, hemp or flax. Flax is used to make linen textile, which has been preferred for canvasses since early times. Flax fibers are thinner and longer than cotton, but the fiber tube has thicker walls producing a stronger and finer yarn. It is still used by artists for its high quality, durability, strength and light weight. It can be thin and tightly woven, and is suitable for use with oil paint [8, 10].

Several types of weave structures can be produced by interlacing the weft and warp in different ways. The ones that are usually used for painting supports are plain weaves, ribs and twill weaves [7]. Plain weaves (Fig. 2.1a) are the simplest, and are formed by weaving one warp with one weft yarn. This weaving method produces the tightest canvas because the yarns are closely woven [11]. Rib weaves (Fig. 2.1b) are simple modifications of plain weaves which are produced by interlacing two or more adjoining warp and weft yarns across each other. Twill weaves (Fig. 2.1c) are produced by interlacing the weft yarns over one or more warp yarns in a repetitive pattern that produces diagonal lines on the face of the textile [12].

a) Plain   b) Rib   c) Twill
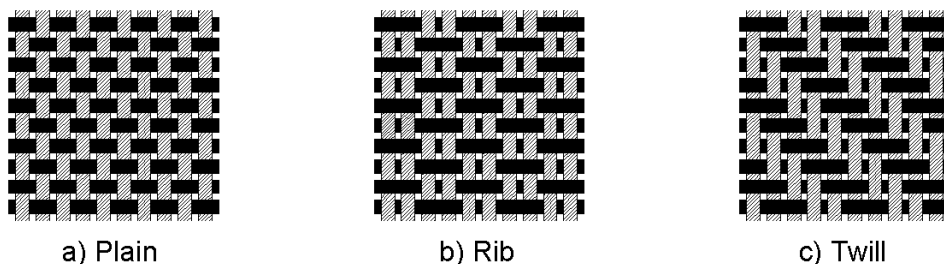
Figure 2.1: Basic weave types used for canvas supports.

In order to prepare a canvas for painting, it must be stretched across a wooden frame called a stretcher. The traditional method for stretching a canvas is depicted in Fig. 2.2. First the canvas is laid on the stretcher (Fig. 2.2a) with the threads of the canvas parallel to the wooden frame. One side of the canvas is tacked in the middle part of one of the stretcher bars (Fig. 2.2b). The opposite side is stretched with canvas pliers and tacked again (Fig. 2.2c). Canvas pliers have flat grips that do not tear the thread. The same process is repeated for the other pair of sides working out from the center along towards the corners (Fig. 2.2d). Finally, the corners are folded (Fig. 2.2e) and stapled to the back of the frame (Fig. 2.2f). For additional stretching or to tighten a slack canvas, wedges or keys can be driven into the corners of the stretcher [13–15].
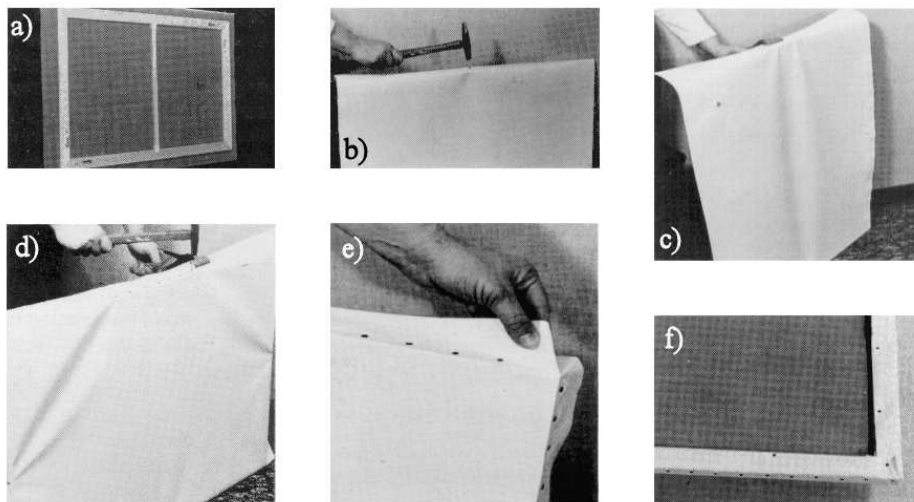
Figure 2.2: Canvas stretching process: a) lay canvas on stretcher; b) tack to one stretcher bar; c) pull and tack to opposite bar; d) repeat for other pair of bars and move towards corners; e) fold corners; f) staple to back [1].

The basic layers applied over the canvas support, once it has been stretched, are shown in Fig. 2.3a. First, it is usually coated with a preparatory layer called the ground. This layer produces a smooth uniform surface to paint on and it prevents paint from being absorbed by the porous canvas textile. The oil from the paint can also be drained towards the textile causing the paint to become brittle very rapidly. It is very common nowadays that a prepared canvas with a ground layer is purchased from a roll and stretched afterwards, or acquired pre-mounted on a stretcher.

The ground is composed of an adhesive layer (size) and filling materials. The adhesive layer provides strength for the bond between the canvas support and the filling materials. Traditional adhesives were usually made of animal glue, but currently, synthetic glue is used. The filling materials are applied to fill the pores of the support and provide a smooth flat surface. Some of the most common filling materials are gypsum, or chalk. An oil ground can also be used composed of a drying oil, generally linseed oil, and a white pigment. Lead white was traditionally used for this purpose, but has been substituted for titanium white or zinc white due to the toxicity of lead. Works on canvas have one to three filler layers, but two is the most common.

Once the ground layer is completely dry, the paint layers can be applied. Paints are composed of pigments and binders. Pigments are the coloring
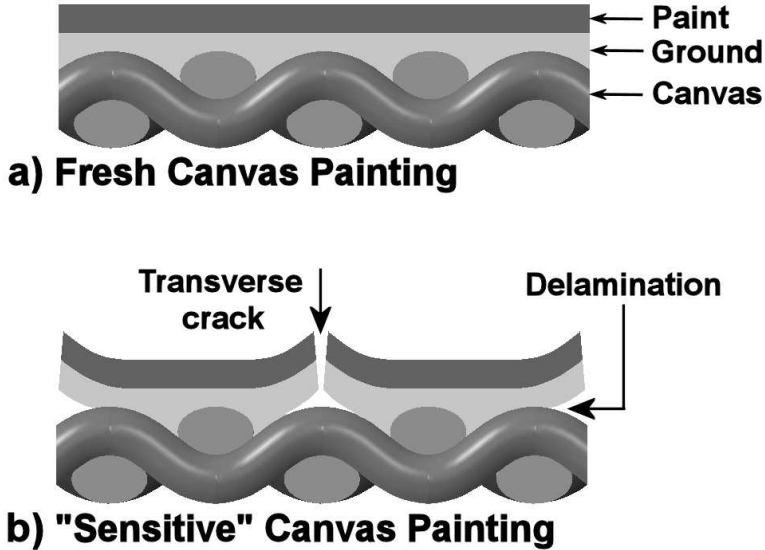
Figure 2.3: Cross-section view of the layers that form: a) a fresh canvas painting; b) a "sensitive" canvas painting.

substances that are suspended in the binding media that forms a solid paint film when dry. Common painting materials include oil and tempera paints, watercolour and modern acrylic paints. Oil paints have been traditionally used by artists for their good properties. They are composed of a high concentration of ground pigments suspended in a drying oil (usually linseed oil), forming a smooth, slow-drying luminous paint ideal for blending colors together. An optional varnish layer may be applied afterwards to protect the paint from discoloration by dirt and to give colors a saturated appearance [8, 15, 16].

2.2 Aging and Mechanical Behavior of Paintings

From the moment a canvas painting is made, the organic and inorganic materials that are put together in multiple layers begin to change and age. The rate at which the painting ages depends on the way it is constructed, the type of materials used and the care given to the work of art. There are several physical, chemical and biological factors that contribute to the structural change and aging of paintings. Mechanical damage produced by stresses in the painting is usually an end result of the factors mentioned above. The damage can take the form of transverse cracking (craquelure), delamination, and flaking of the paint film, see Fig. 2.3b.

When considering a canvas painting as a layered structure, each layer of material will have its own properties and will respond differently to environmental changes. This causes volumetric changes producing stresses in each layer because they are restrained by the adjacent materials. If the stresses exceed the ultimate strength of the material, then the paint film will crack, releasing the stresses.

There are three categories of cracks in paintings: drying cracks, age cracks and cracks produced by mechanical loads [17]. Early cracking of oil paint films that occurs during the drying process involves oxidation of the oil in contact with the atmospheric oxygen [18], and polymerization of the film producing stresses as the material hardens and tries to contract. An example of drying cracks is so-called mud cracking. Mud cracks usually occur on thick paint layers. The oxidation and polymerization takes place only in the surface, which dries and contracts first, while the subsurface is still fresh causing a concave cracking pattern similar to the one found in the cracking of mud [2], see Fig. 2.4a. Another example of drying cracks is called alligatoring, named after the cracking pattern which resembles the hide of an alligator, see Fig. 2.4b. Alligatoring occurs usually due to drying and shrinkage of an outer layer while the under-layer is still soft. Another possible cause of alligatoring is the poor adhesion of a high shrinkage paint layer over the substrate [8].

a) Mud Cracking   b) Alligatoring   c) Age Cracking
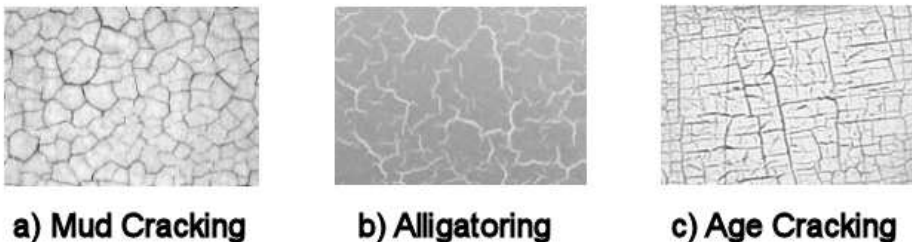
Figure 2.4: Drying Cracks: a) Mud Cracking [2] b) Alligatoring [3] c) Age Cracking [4]

As a paint film ages, physical and chemical factors such as light and furhter oxidation cause embrittlement of the material and an increase in the elastic modulus. Physical factors such as temperature and humidity are considered to be the main cause of age cracks, see Fig. 2.4c. There has been a considerable amount of research done on the mechanical response of paintings to temperature and humidity [19–23]. These studies show that temperature and humidity cycles would cause unequal dimensional changes in each material due to their different expansion coefficients. Since the materials are restrained by

the adjoining layers, they experience an increase in stresses. This may lead to cracking because the aged materials will develop higher stresses as their elastic modulus is higher and they are not capable of withstanding high deformations. The damage accumulates during aging due to the continuous fluctuation in the environmental conditions.

An important model developed by Mecklenburg [24] describes the stress redistribution in the deterioration process of paintings. Mecklenburg argues that for a stretched canvas painting, all the layers are in tension, which is carried mostly by the glue, ground and paint. Cracking from drying and embrittlement of the paint causes a partial release of stress in the paint and the canvas takes over the tension. The stress relocation and realignment causes out of plane displacement of all of the layers, a phenomenon called "cupping".

After transverse cracking, stress concentrations are formed at the paint film edges and the cracks may start growing through the interface (delamination) due to shear stresses caused by different (humidity or temperature) expansion coefficients between the paint and the substrate. When the shear stresses are higher than the interface strength, delamination between the paint film and the substrate occurs [25], see Fig. 2.3b. The ground and paint layers have similar mechanical properties, and will react as a single material when subjected to stresses. Thus, a transverse crack produced in the paint will usually go through the ground completely until it reaches the support before delamination occurs. However, delamination can also occur between the paint and ground in cases with poor adhesion between these layers [26].

In addition to damage caused by internal stresses, the application of external loads causes deformation of the canvas support producing stresses in the paint layers that may also lead to cracking. This type of damage generally occurs when the painting is being handled or transported. Examples include accidental impact of the frame, puncture of the canvas, rubbing of the painting surface, and vibration of the canvas. When the canvas slackens, it is common practice to insert wedges (keying-out) into the stretcher to re-stretch the canvas. This can cause cracking emerging from the corners perpendicular to the principal stress directions as described by Mecklenburg [19]. On rare occasions, the only way to transport large paintings is to remove them from the stretcher and roll them on wide cylinders. This may result in cracking if the paint is aged and brittle, or if the radius of curvature is not large enough (the painting is rolled too tightly) [27].

2.3 Vibration of Canvas Paintings

It has long been recognized that vibrations are one of the main factors which could be potentially damaging to works of art. The increase in loans and traveling exhibitions, and the concomitant need to transport them by road, rail, sea, and air; as well as the exposure to events near museums (such as construction, traffic, loud concerts, etc.) has caused a legitimate concern regarding the protection of works of art against shock and vibration from the museum field. The problem is that decisions about vibration exposure are taken without a solid understanding of the nature of the problem.

One of the main sources of information about the packing and transportation of paintings was brought together in the conference "Art in Transit" held in London in 1991 [28]. Participants recognized that the vibration of canvas paintings, as for any dynamic system, is characterized by natural frequencies and mode shapes. They acknowledged that resonant frequencies, especially the fundamental frequency, would be the potentially harmful ones for the object due to the large displacements associated with them [29, 30]. This suggested the need to characterize the natural frequencies in terms of the parameters that affect them, providing an understanding of the dynamics of a canvas painting system.

Many studies have measured and monitored shock and vibration levels on paintings and museum objects during transport and museum environments [31–34]. The main issue with virtually all of these studies is that they measure and are concerned only about shock, and fail to differentiate it from vibration (up to the point of using a single interchangeable term "shock/vibration"). A shock is a single sudden load of high amplitude that occurs in a short period of time which can produce immediate damage to the work of art. Examples are impacts caused by handling, packing or unloading of the object from a transport vehicle. On the other hand, vibrations refer to a series of low amplitude oscillations happening over longer periods of time, such as the ones produced by the engine of a vehicle, or by a road surface during transport. Vibrations, thus, produce long-term and cumulative damage which is usually not immediately visible. These "non-tangible" effects produced by vibrations tend to be overlooked by the art conservation literature as opposed to shock.

Further drawbacks in these art conservation studies are that all measurements are performed on locations adjacent to the objects, such as packing cases, museum walls and floors, but not on the object itself. Thus, the acquired data is not representative of the actual vibration levels and behavior experienced by the object. Additionally, the vibration data is usually analyzed in acceleration units (g's), which do not provide proper insight when trying to

find a relation to damage in the objects. Displacement units would be more intuitive since they can be related to stresses in the material. Furthermore, the influence of the frequency in the measured acceleration is not taken into account. That is, a certain acceleration level at a high frequency translates to a lower displacement than the same acceleration level at a low frequency. Therefore, the measured vibration damage levels are totally misleading, not to mention that these levels cannot be generalized for all materials and objects since they are measured only for specific ones.

Several solutions to mitigate vibration effects such as fabric lining, backing boards, air-ride suspension vehicles and foams for packing have been investigated [29, 35, 36]. Typical packaging methods for paintings consist of a protective external shell with interior cushioning foam or suspension straps or springs [37–40]. Given the lack of theoretical understanding of the vibration phenomenon in canvas paintings, the influence that these solutions have on the dynamic behavior of the system is not completely understood and the desired effect may not be produced. Additionally, the packing methods are usually designed to account for shock and not vibration.

As Green noted [35], immediate damage, such as that occurring from shock, is unlikely to happen from the vibration of the canvas due to the low stress levels involved. Instead, long term damage may occur through fatigue cracking of already cracked or loose paint. Some investigators [36, 41, 42] performed vibration measurements on fresh or un-cracked paintings and argued that vibrations do not represent a problem in terms of paint cracking. The problem in these cases is that the damage mechanism considered is the formation of transverse cracks (crack initiation) in the surface of the paint layers. This is a different mechanism than crack growth (delamination) along the interface, which is the main concern regarding pieces of paint falling off the canvas. The experiments thus did not simulate "sensitive" paintings.

The cumulative effect that vibrations have on canvas paintings was first recognized and studied by the Netherlands Institute for Cultural Heritage (ICN), now the Cultural Heritage Agency of the Netherlands (RCE). An investigation was conducted at the ICN (now RCE) to examine the effect of rock concerts taking place next to museums in the Museumplein. The results showed loss of paint fragments from tested paintings after 12 and 15 hours of rock music [43]. A similar problem was investigated on the square adjacent to the State Hermitage Museum in St. Petersburg. According to Johnson and Akbar [44], preliminary results from a scientific study performed by Grabar Art Restoration Institute in Moscow show that "every 10 concerts above 82 decibels add an extra year to the age of a work". Not only works of art and artifacts, but also historical buildings are susceptible to vibration damage. Another study

investigated the effect of loud music on the Hampton Court Palace building. The results show degradation in windows directly exposed to acoustic vibration [45]. Such studies demonstrate the cumulative effect of vibrations on the condition of an object.

2.4 Modeling of Canvas Paintings and Textiles

A canvas painting model is useful for predicting the behavior of the structure under vibration loading and determining the frequencies and amplitudes that can be potentially harmful for the painting. However, virtually no modeling work has yet been performed to describe the dynamics of canvas paintings. To the author's knowledge, Mecklenburg and Tumosa [46] have reported the only FE model for canvas paintings which are subjected to vibration and impact. They examined several mechanical properties of painting materials and used them as input for the FE model which was assembled using three different layers for the canvas, glue and paint. To account for the empty space between the yarns in the textile, an effective thickness of about 22% of the nominal thickness of the canvas textile was used when modeling it as a homogeneous material. This assumption was based on a volumetric analysis to measure the volume of the weft and the warp yarns separated from the textile. Based on the modeling results they concluded that vibrations are unlikely to produce damage on the paint. This, however, will only be true for fresh paintings with no pre-existing transverse cracks (craquelure), and not for sensitive paintings in which delamination damage and interface fracture toughness are an issue. Some additional drawbacks of this work were that the canvas was assumed to be isotropic, having an average modulus between the weft and the warp. Furthermore, there was a lack of free vibration and modal analysis, and the model predictions were not experimentally verified.

A static FE model of a canvas painting was developed in an investigation carried out by the ICN (now RCE) together with the Delft University of Technology in order to determine a suitable sewing method for the restoration of the slashed painting "Cathedra" [47]. The painting was originally made on a cotton canvas. It was later lined with linen bonded to the back of the canvas. For the model, both canvasses were treated as orthotropic lamina with an assumed thickness of 0.2 mm to model the bending stiffness of the textile. The paint layers were not explicitly modeled, though the mechanical properties of cotton + paint were used as input for the model. The out-of-plane deflection of the canvas due to two sewing methods was analyzed making assumptions about the original stress state in the painting and the material properties used. The painting was repaired using the results of this study.

Visitors considered the restoration a success since the slashes were not visible.

Similar to canvas paintings, the literature in the textiles field on the dynamic behavior of the structure is scarce. The vibration properties of textiles under uniaxial loading have been studied by Aubry [48]. In this investigation the textile is assumed to be a continuous membrane and the natural frequencies are predicted with a simple analytical model based on membrane theory. The experimental verification involved a rectangular textile specimen hung with a constant stretching load clamped at the bottom and a harmonic excitation (shaker) at the top clamp. The fundamental natural frequency was measured with a microphone near the surface at the middle of the specimen. However, the natural frequencies are not predicted with sufficient accuracy, and it is acknowledged that plate theory would provide a better description of the textile. Given that the mechanical properties of the textile were not taken into account in that model, the bending stiffness and the Poisson effect between the orthogonal yarn directions by a uniaxial load are not considered.

In the field of textiles, there is a large literature on modeling work. Two methods are generally used to model the mechanical behavior and deformation of textiles, modeling them as continuous or discontinuous structures. The former method treats the textile as a continuous thin sheet of material [49–52], while the later takes into account the microstructure of the textile explicitly modeling the constituent yarns [53, 54].

In static analyses using the continuum approach, the textile is treated in most cases as a thin homogeneous plate of orthotropic material used to simulate uniaxial and biaxial loading, and simple draping behavior [49–51]. Due to the small thickness of the textile, the stress components in the transverse direction are neglected and plane stress conditions are assumed. Given the orthogonal symmetry of the weft and warp material directions, the elastic stress-strain relations for an orthotropic material under plane stress conditions are applied. These relations are defined based on four independent mechanical properties which include two elastic moduli for the weft and warp directions, an in-plane Poisson's ratio and shear modulus. The elastic moduli are usually determined by tensile tests in the yarn directions. However, the determination of the Poisson's ratio and shear modulus is not straight forward and several assumptions are necessary. Another main issue is the difficulty in defining an effective cross-section area (thickness) for the case of a woven structure. The problem has been avoided in many cases by redefining the stress as the force per unit length of the textile. However, this causes an incompatibility with the conventional stress units (MPa) when the textile is not analyzed isolated. The continuum approach offers a simple basic framework to describe the behavior of complex structures as that of textiles. However, additional theoretical and

experimental work is necessary in order to develop a widely accepted modeling approach to describe the complex deformation in textiles [52].

In order to account for a more complete behavior of textiles considering nonlinear effects, friction and interaction between yarns, a discontinuous microstructural approach is necessary [53]. In this approach the yarns in the weave are modeled explicitly as straight or curved rods, beams or solid elements assembled with frictional connections at crossing points between weft and warp yarns [54]. However, this presents many difficulties for the analysis due to the intricate architecture of the weave and complex contact mechanics between the yarns. This method has been useful for predicting the mechanical properties of textiles from their constituent yarns as only a patch of textile is necessary for the analysis [55, 56]. However, in order to predict global scale deformations, the method is not computationally efficient due to the large number of yarns and connections present.

2.5 Concluding Remarks

The need for guidelines and recommendations to approach the problem of vibrations on sensitive canvas paintings has been of great concern due to the increase in vibration exposure events, and the obvious need to protect valuable collections from possible damage. However, based on the literature, there is still little understanding about the actual vibration behavior of paintings, partly because of their complex morphology and the limited amount of information available on their mechanical behavior in the cultural heritage field. Clearly, the need to develop a predictive model for the vibration of paintings is of critical importance in order to comprehend the main parameters involved and have a deep understanding of their dynamic behavior. The development of this model would be a solid stepping stone in the process of creating general guidelines to assist museums in decision making and protective measures against vibration damage. Moreover, this interdisciplinary project will shorten the gap between the art world and the engineering field.

Chapter 3

Modeling

The global dynamic response of a canvas painting to cyclic loading is an example of a forced vibration problem. Forced vibration occurs when a system is continuously excited by an externally applied oscillatory disturbance. However, the forced response of a painting will depend on its natural frequencies (eigenfrequencies), vibration modes (eigenmodes) and damping. These are intrinsic dynamic properties of the system that characterize the free vibration problem.

Free vibration occurs when an initial stimulus in the form of an initial displacement and/or an initial velocity is imparted to the system. In theory, the system will oscillate continuously at its natural frequencies and will exhibit vibration patterns called mode shapes. However, in practice, damping (e.g. friction) will cause loss of energy in the system until the motion stops [57]. The study of free vibration is essential to characterize and understand the behavior of a structure before describing its forced response. In fact, the dynamic response can be considered as being a combination of the eigenmodes [58].

The physical system can be described by mathematical equations in order to analyze it. However, analytical (exact) solutions to mathematical models can be obtained only for simple problems. Approximate numerical methods are required in order to analyze more complex structures such as in the case of canvas paintings. The Finite Element (FE) method is a numerical analysis technique for finding approximate solutions to engineering problems [59]. This is a very powerful and versatile method; however it must be used with careful engineering criteria.

A systematic procedure is followed in the present investigation in order to develop a FE model to characterize the dynamic behavior of canvas paintings. First, a simple analytical model to describe the free vibration behav-

ior of a painting is developed. This model provides an understanding of the
parameters involved in the dynamics of the structure, and is used to verify
the convergence of an equivalent FE model (see Appendix C). Subsequently,
assumptions and parameters are considered for the FE model to obtain an
appropriate representation of the real system. The predicted FE and experi-
mental eigenmodes are compared in order to improve and optimize the model.
Finally, once the FE model has been verified experimentally, it can be used to
predict the forced response of a painting.

3.1   Analytical Model

An analytical model was developed for the free vibration of a canvas painting
with a general layered structure as the one shown previously in Fig. 2.3a. The
rear and cross section views on a global scale of a typical canvas painting of
length a, width b, and thickness h are shown in Fig. 3.1. The stretcher is
considered to be infinitely stiff, that is, the deformation of the stretcher is
considered to be negligible compared to the deformation of the canvas.

On a global scale, the canvas painting can be modeled as a thin plate, Fig.
3.2, since the thickness is much smaller than the in-plane dimensions. The
plate is biaxially loaded with the line forces N_x and N_y (N/mm), representing
the tension that the canvas has when mounted on the stretcher as shown pre-
viously in Fig. 2.2. The modeled plate is considered to have simply supported
edges representing the simple contact supports provided by the stretcher bars
at the edges of the canvas. a, b and h correspond to the canvas dimensions in
Fig. 3.1 in the directions x, y and z respectively.

The painting itself is composed of several layers of material corresponding
to the canvas, ground and paint layers that are bonded together forming a
laminate as seen in Fig. 3.3. The thickness of each layer is small compared
to their in-plane dimensions, so that they can also be modeled as thin plate
elements [60]. Although the materials are highly inhomogeneous on a micro-
scopic scale, on a global scale they are assumed to behave as homogeneous flat
plates. Within the laminate, the plates are considered to be perfectly bonded,
the bonds are considered to be infinitesimally thin, and the layers cannot slip
relative to each other. The laminate therefore acts as a single thin plate [61].
The constitutive equations for the equivalent laminated plate can be derived
using Classical Laminate Theory.

The basic idea of thin-plate theory is to reduce a three dimensional problem
to an approximate two dimensional one. The definition of a plate as having one
dimension much smaller than the other dimensions results in simplifications
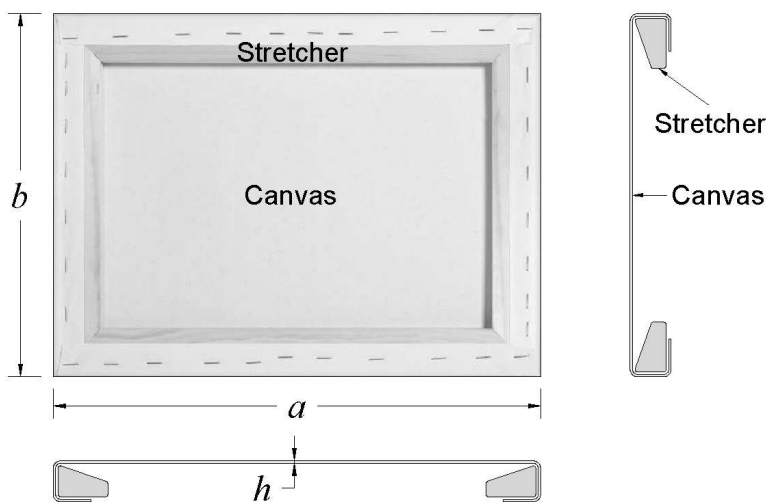
Figure 3.1: Rear and section views of a typical canvas painting on a stretcher.
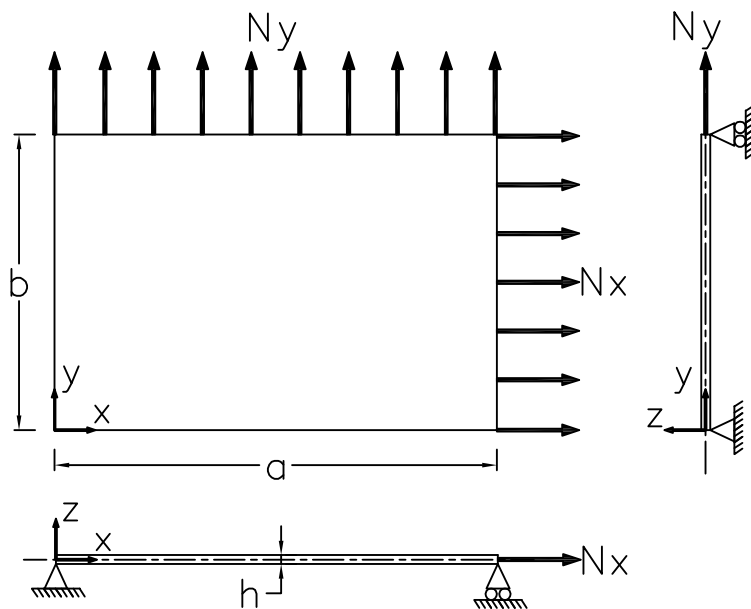
Figure 3.2: Simply supported plate subjected to biaxial loading.
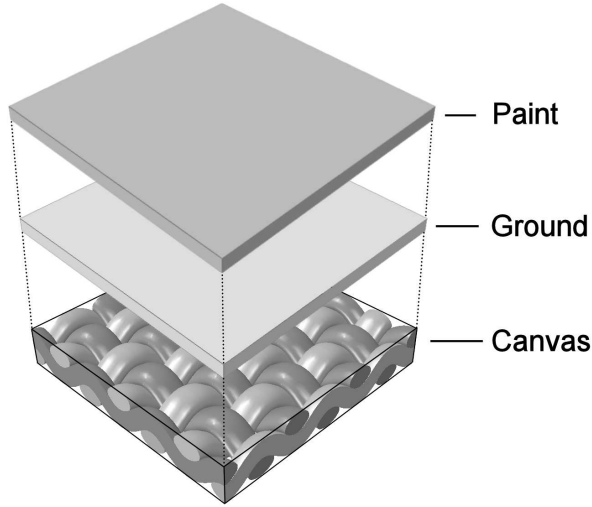
Figure 3.3: Exploded view of the canvas ground and paint layers forming a laminate.

that are called the Kirchhoff assumptions [62]:

- Lines normal to the mid-plane remain straight, normal and inextensional during deformation. As a consequence, shear strains may be neglected.

- The transverse normal stresses are small compared to the longitudinal normal stresses and may be neglected.

The fundamental laws that govern the dynamic behavior of the structure are fully described by the kinematic equations which relate the strains to the displacements, the constitutive equations that relate the stresses to the strains, and the dynamic equilibrium equations relating external forces to internal stresses. The two Kirchhoff assumptions are used to derive the kinematic and constitutive relations respectively, while the dynamic equilibrium equations are derived from equilibrium of forces and moments [63]. The detailed derivation of these expressions and the solution can be found in Appendix A. The resulting expression for the natural frequencies is given by

$$
\begin{aligned}
\omega_{mn}^2 = \frac{\pi^4}{\bar{m}} & \left[D_{11} \left(\frac{m}{a} \right)^4 + 2 \left(D_{12} + 2D_{66} \right) \left(\frac{m}{a} \right)^2 \left(\frac{n}{b} \right)^2 + D_{22} \left(\frac{n}{b} \right)^4 \right] \\
& + \frac{\pi^2}{\bar{m}} \left[N_x \left(\frac{m}{a} \right)^2 + N_y \left(\frac{n}{b} \right)^2 \right]
\end{aligned}
\tag{3.1}
$$

and the corresponding mode shapes are given by

$$w(x, y)_{mn} = W_{mn} \sin\left(\frac{m\pi x}{a}\right) \sin\left(\frac{n\pi y}{b}\right) \tag{3.2}$$

where W_{mn} represents the arbitrary scaled amplitude, and m and n represent the number of half waves in the x and y direction. Note that the frequencies are directly proportional to the pre-stretching biaxial loads N_x, N_y and the bending stiffness D_{ij} of the laminate, and inversely proportional to the mass $\bar{m}$ and the size a, b of the laminate.

3.2   Modeling the Canvas as a Homogeneous Plate

There are several parameters that must be defined in order to model the canvas textile as a homogeneous orthotropic plate. The mechanical behavior of the plate is defined by the thickness of the plate model (h_m) and the elastic constants $(E_1, E_2, \nu_{12}, G_{12})$. E_1 and E_2 are the elastic moduli for the weft and the warp respectively, ν_{12} is the Poisson's ratio, and G_{12} is the shear modulus. The sub indices $_1$ and $_2$ correspond to the weft and warp yarn directions of the weave. In this case, the weft $_{(1)}$ and warp $_{(2)}$ directions are assumed to be aligned with the plate coordinates x and y respectively (see Fig. 3.2). A number of assumptions need to be considered in order to determine each one of these properties based on the real textile characteristics. These assumptions are described in the following sections for each parameter and corresponding selected canvas textiles. The selected canvas textiles for modeling and testing, the reasons for their selection and their factory properties can be found in Section 4.2 of Chapter 4, Experimental Procedures.

Thickness

The canvas textile has an inhomogeneous micro-structure formed of woven yarns with a high percentage of empty space between them, see Fig. 3.4. Additionally, the yarns themselves have negligible bending stiffness compared to their stretching stiffness. The textile thus also exhibits a low bending stiffness, as well as a relatively high stretching stiffness. When modeling the canvas as a homogeneous plate, the plate model must therefore reproduce the stretching and bending behavior of the textile.

The bending stiffness of the plate is largely dependent on the value of the equivalent thickness assumed (h_m). (As an analogy, a thick string would be harder to bend than a thinner one). If the nominal thickness of the textile is
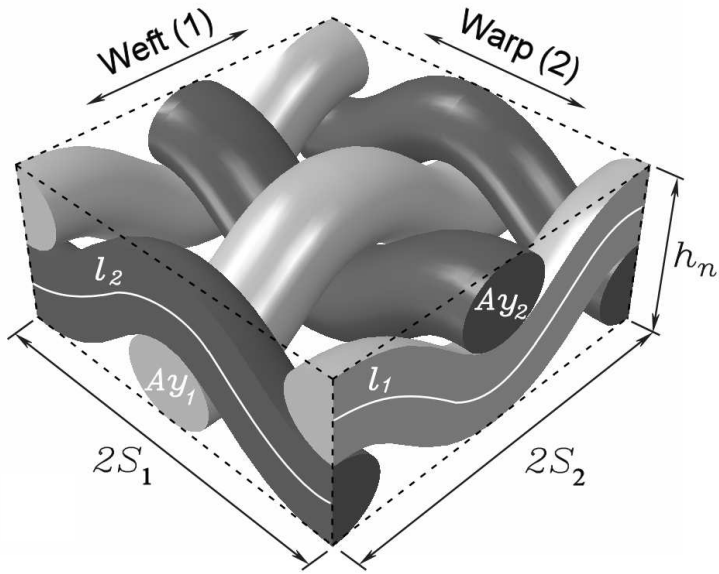
Figure 3.4: Representative unit cell (RUC) of a plain weave textile.
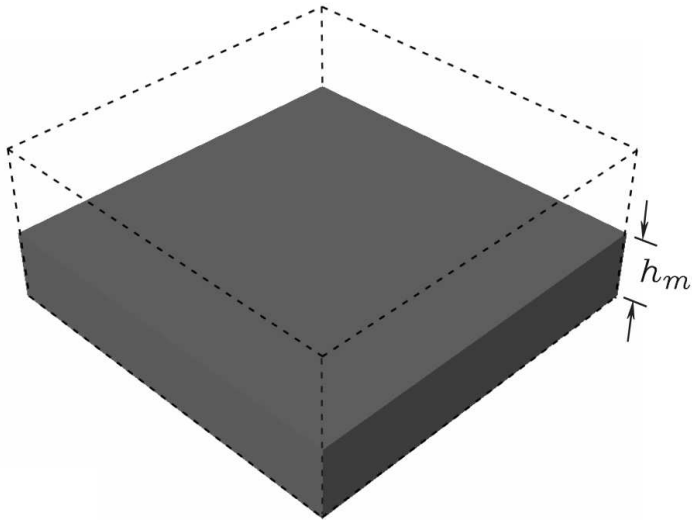
Figure 3.5: Modeled canvas plate with reduced thickness.

considered for the plate model, the bending stiffness of the model would be higher than the actual bending stiffness of the textile due to the voids in the textile. Therefore, an effective thickness of the model plate is required in order to account for the empty spaces in the weave and model the bending stiffness correctly, see Fig. 3.5. This effective thickness of the plate is determined by assuming conservation of volume in the textile and in the equivalent plate. This depends on the yarn volume fraction in the textile. The volume fraction of the weft and warp yarns in the weave is determined by defining a representative unit cell (RUC) that repeats itself throughout the entire weave, see Fig. 3.4. Note that there are two weft yarns and two warp yarns in the RUC. S_1 and S_2 represent the spacing between the yarns, and h_n is the nominal thickness of the textile. The total volume of the RUC is given by

$$V_{RUC} = 4\,S_1\,S_2\,h_n \tag{3.3}$$

The volume fraction of the weft yarns is defined by

$$V_{f1} = \frac{2\,Vy_1}{V_{RUC}} \tag{3.4}$$

where Vy_1 is the volume occupied by one weft yarn in the RUC and is calculated by multiplying the cross-section area of the yarn Ay_1 times the length of the yarn l_1 in the RUC.

$$Vy_1 = Ay_1\,l_1 \tag{3.5}$$

The cross-section area of the yarn is similar to a lentil as shown in Fig. 3.6a. The originally circular yarns are flattened in the textile due to the weaving process. To calculate the approximate cross-section area of the yarn, it is assumed to have a circular shape (Fig. 3.6b). Therefore, the area is given by $Ay = \pi d^2/4$, where the diameter of the equivalent circle, d is assumed to be the average of the e and g dimensions of the lentil shape $d = (e + g)/2$. Areas of yarns were measured on the images of cross-section samples of the textile taken under the microscope with a program called Image J. Image J is a public open source software for editing, processing and analysis of images in Java platform [64]. The approximated area was shown experimentally to be in agreement with the actual measured area of the yarn.

The yarn dimensions of the selected textiles were measured under the optical microscope. For this, textile samples of 1 cm^2 were embedded in polyester resin and a smooth cross section was obtained using consecutive polishing discs, see Fig. 3.7. Ten measurements of the dimensions e and g of the lentil
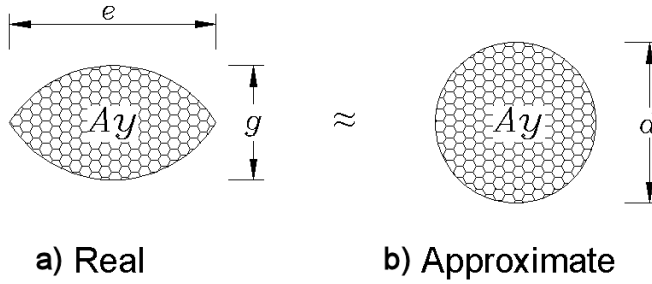
Figure 3.6: Real lenticular cross-section of yarn and approximate circular cross-section.

shaped yarn for the weft and warp were taken. The average values and the standard deviation are given in Table 3.1 together with the approximated circular diameter d.
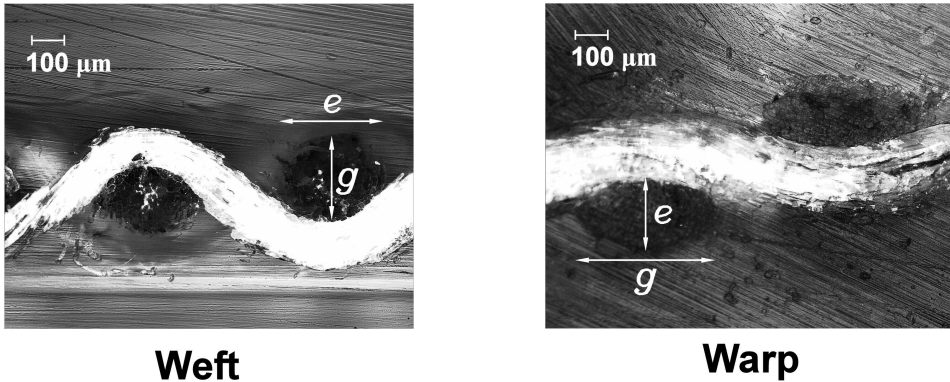
Figure 3.7: Yarn weft and warp cross-sections for Rijn linen

In order to consider only the volume occupied by the fibers in the yarn, a packing factor is defined. The fibers are assumed to be long, circular and to have hexagonal close-packing as shown in Fig. 3.8a.

The packing factor is calculated by considering the triangular element shown in Fig. 3.8b. There is one fourth of the circular area of the fibers in the total area of the triangle. Thus the packing factor is given by

$$P_f = \frac{\pi \, r^2/4}{\sqrt{3} \, r^2/2} = \frac{\pi\sqrt{3}}{6} = 0.907 \tag{3.6}$$

Table 3.1: Dimensions of real yarn and circular yarn approximation

| Material | Direction | Real | | | | Approx. |
		$e[mm]$	SD	$g[mm]$	SD	$d[mm]$
Rijn Linen	Weft	0.352	0.046	0.250	0.027	0.301
	Warp	0.574	0.070	0.196	0.028	0.385
Waal Linen	Weft	0.278	0.023	0.167	0.016	0.223
	Warp	0.406	0.028	0.115	0.012	0.261
Amazone Linen	Weft	0.373	0.054	0.262	0.018	0.317
	Warp	0.500	0.058	0.167	0.022	0.333
Cotton	Weft	0.364	0.016	0.298	0.025	0.331
	Warp	0.236	0.016	0.175	0.014	0.206
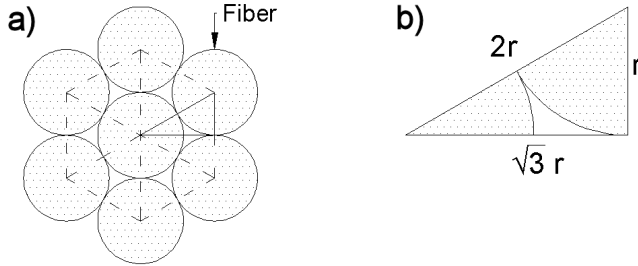
Figure 3.8: Hexagonal close-packing of the fibers in a yarn.

Hence, the area of the yarn is multiplied by the packing factor

$$Ay = \frac{\pi d^2}{4} P_f \qquad (3.7)$$

It can be observed in Fig. 3.4 that the length of the yarn inside the RUC depends on the waviness or undulation of the yarn in the textile. This waviness is called the crimp of the yarn and it is produced in the weaving process when yarns are forced to bend around each other. The value for the crimp is defined as the ratio between the excess in length of the yarn over the length of the cloth [65]. Thus, the crimp in the weft direction for the RUC under consideration is given by

$$c_1 = \frac{l_1 - 2 S_2}{2 S_2} \qquad (3.8)$$

Therefore the length of the weft yarn in the RUC is given by

$$l_1 = 2\,S_2\,(1 + c_1) \tag{3.9}$$

Substitution into Eq. 3.5 yields

$$Vy_1 = 2\,Ay_1\,S_2\,(1 + c_1) \tag{3.10}$$

Replacing Eq. 3.10 and Eq. 3.3 into Eq. 3.4 yields

$$V_{f1} = \frac{4\,Ay_1\,S_2\,(1 + c_1)}{4\,S_1\,S_2\,h_n} \tag{3.11}$$

Simplifying terms and considering that the yarn spacing is equal to the inverse of the yarn count, $S_1 = 1/N_1$, results in the following expression for the weft yarn volume fraction:

$$V_{f1} = \frac{Ay_1\,N_1\,(1 + c_1)}{h_n} \tag{3.12}$$

Similarly, the expression for the warp yarn volume fraction is

$$V_{f2} = \frac{Ay_2\,N_2\,(1 + c_2)}{h_n} \tag{3.13}$$

Thus, in order to determine the volume fraction of the textiles, the nominal thickness values (h_n) and the crimp values (c_1, c_2) of the selected textiles were measured experimentally.

Measurements of the nominal thickness (h_n) of the textiles were performed using a caliper. The average values and standard deviation of ten measurements performed for each material are given on Table 3.2

Table 3.2: Measured textile thicknesses

Material	$h_n[mm]$	SD
Rijn Linen	0.562	0.010
Waal Linen	0.396	0.010
Amazone Linen	0.369	0.011
Cotton	0.453	0.011

The crimp in the weft (c_1) and warp (c_2) of the selected textiles was measured by the relation between the length of the yarn in the textile sample,

and the length of the yarn after it has been removed from the textile. Crimp measurements were performed according to the ASTM Standard D3883 [66]. According to these standards, the crimp is expressed as a percentage value given by

$$c = \frac{Y - Y_o}{Y_o} \times 100 \tag{3.14}$$

where Y_o is the distance between two marks on a yarn in the textile sample, and Y is the distance between the same marks on the yarn after being removed from the textile, see Fig. 3.9. The distance measurements of the yarn removed from the fabric were performed by straightening the yarn (without stretching it) by hand to remove the undulations of the yarn due to the weaving process. The resulting crimp measurements are given in Table 3.3.
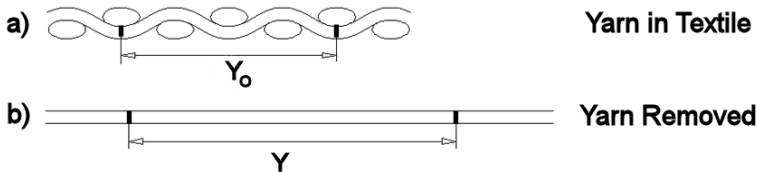
Figure 3.9: Yarn length in the textile sample (a) and removed from the sample and straightened (b)

Table 3.3: Crimp measurements in weft and warp directions

Material	Direction	Crimp [%]	SD
Rijn Linen	Weft (c_1)	0.92	0.30
	Warp (c_2)	19.60	0.57
Waal Linen	Weft (c_1)	1.68	0.30
	Warp (c_2)	18.88	0.30
Amazone Linen	Weft (c_1)	0.96	0.15
	Warp (c_2)	15.04	0.41
Cotton	Weft (c_1)	5.92	0.30
	Warp (c_2)	19.84	0.41

The calculated values for the weft and warp yarn cross-section areas and volume fractions of each of the textile samples tested are given in Table 3.4. The area of the yarns was calculated with Eq. 3.7 and the volume fractions were calculated with Eqs. 3.12 and 3.13, where the values for the yarn count

(N_1 and N_2) are given in the following chapter in Table 4.1, the crimp values (c_1 and c_2) are given in Table 3.3, and the nominal thickness h_n is given in Table 3.2.

Table 3.4: Yarn section area and volume fraction

Material	Direction	$Ay[mm^2]$	Vf
Rijn Linen	Weft	0.065	0.168
	Warp	0.106	0.382
Waal Linen	Weft	0.035	0.208
	Warp	0.048	0.334
Amazone Linen	Weft	0.072	0.314
	Warp	0.079	0.493
Cotton	Weft	0.078	0.374
	Warp	0.030	0.326

The plate model must reveal equivalent stretching and bending behavior in both the weft and warp directions as the real textile. Assuming that when stretching forces or bending moments are applied in the weft direction, only the stiffness of the yarns in the weft direction play a role (see Fig. 3.10a). The same assumption is considered for the warp yarns (see Fig. 3.10c). Therefore, an equivalent plate with the same volume fraction is considered for each yarn direction as shown in Fig. 3.10b and 3.10c.

The volume fraction of the equivalent plate in the RUC is given by

$$V_{fi} = \frac{V_{plate\ i}}{V_{RUC}} = \frac{4S_1\ S_2\ h_{ei}}{4S_1\ S_2\ h_n} \qquad i = 1, 2 \qquad (3.15)$$

Thus, the effective thickness of the plates for the weft and warp are obtained by multiplying the nominal thickness of the textile by the volume fraction on each direction given by

$$h_{ei} = V_{fi}\ h_n \qquad i = 1, 2 \qquad (3.16)$$

The yarn volume fractions are calculated with Eqs. 3.12 and 3.13. This yields two different effective thicknesses for the weft and the warp direction respectively. However, a plate can only have one thickness, therefore the overall value of the thickness for the plate model h_m of the canvas is taken as the average between h_{e1} and h_{e2}.

The measured, effective and model thickness values are given in Table 3.5. The effective thicknesses (h_e) for the weft and warp directions are calculated
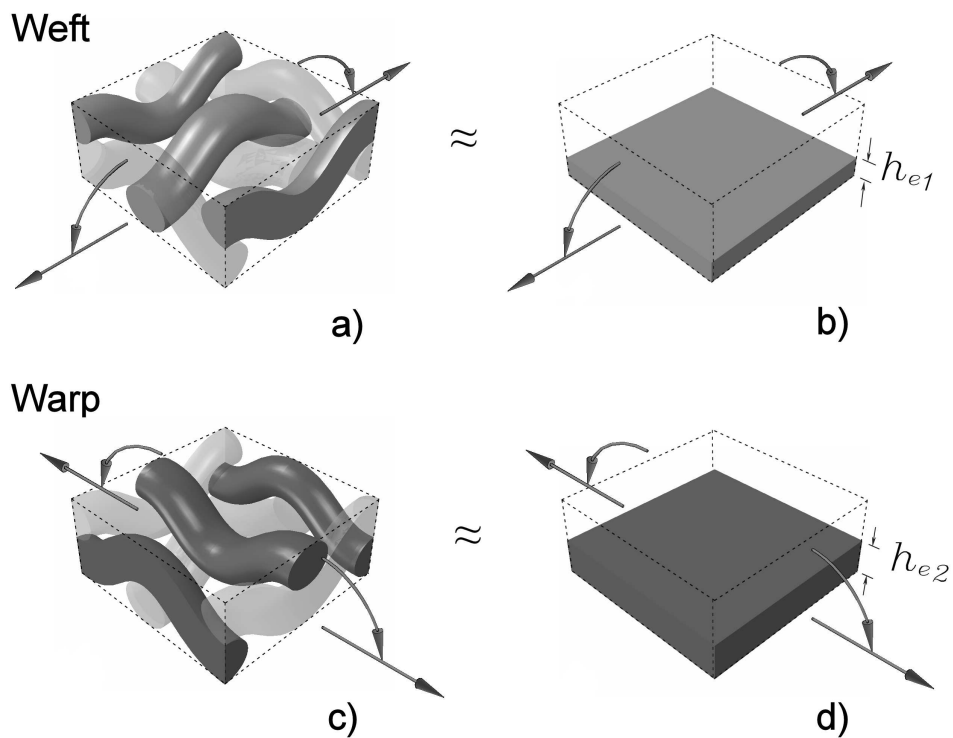
Figure 3.10: Effective thickness of the equivalent plates for the weft and warp directions.

with Eq. 3.16 and the thickness used for the plate model (h_m) is taken as an average of both.

Table 3.5: Measured, effective and model thicknesses

Material	Direction	$h_n[mm]$	$h_e[mm]$	$h_m[mm]$
Rijn Linen	Weft	0.562	0.094	0.155
	Warp		0.215	
Waal Linen	Weft	0.396	0.082	0.107
	Warp		0.132	
Amazone Linen	Weft	0.369	0.116	0.149
	Warp		0.182	
Cotton	Weft	0.453	0.169	0.159
	Warp		0.148	

Elastic Moduli

The elastic moduli of the selected canvas textiles were measured using tensile tests carried out in the weft and warp directions. The tensile tests were performed in a universal tensile testing machine Zwick with 1 KN loadcell capacity. The testing procedure was followed using ASTM standards designation D1682-64 [67]. The dimensions of the specimens were 200 mm x 40 mm. 5 mm of yarns were unraveled from the edges of the specimens to avoid edge effects. The specimens were tested to break with a uniform cross-head speed of 20 mm/min and a pre-load of 5 N, see Fig. 3.11.

The tensile forces are considered to act only on the yarns in the direction in which the test is performed. Therefore, the stresses were calculated as the measured force over the effective yarn cross-section area of the textile. This effective cross-section area was determined by multiplying the width of the textile sample (30 mm) by the effective thickness h_e on the weft and warp directions given in Table 3.5.

The stress-strain curves obtained for the weft and warp directions of the selected canvas textiles are shown in Figs. 3.12 through 3.15. The initial region in the curves reflects the fiber friction and uncrimping effects. The curve is fairly linear in this region with a relatively low stiffness since the material presents a low resistance to stretching as the yarns are straightening out. Note that the initial region of the curve for the weft direction is smaller with a higher stiffness than for the warp. This occurs since the weft yarns are nearly straight in the weave, and the yarn elongation takes place rapidly. On the other hand,
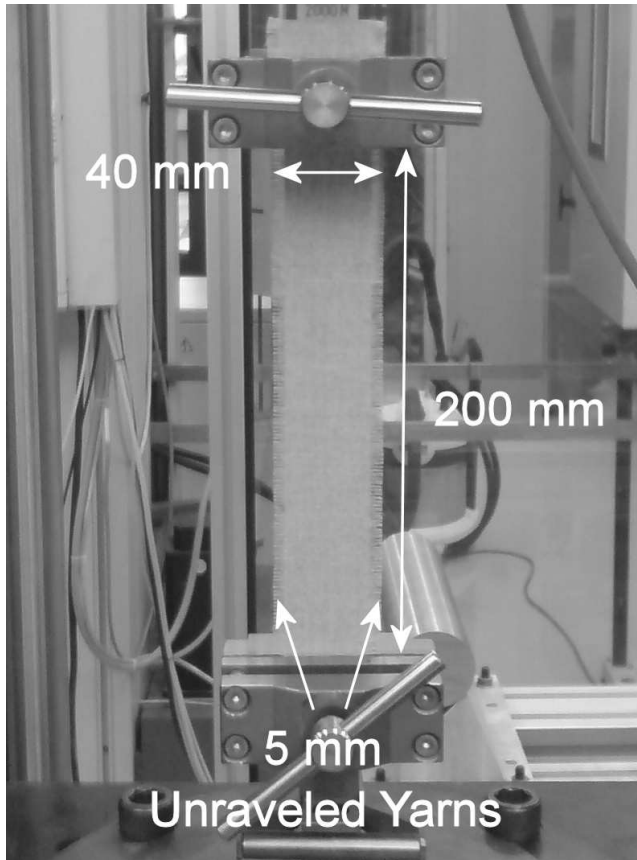
Figure 3.11: Clamped tensile test specimen and dimensions

the warp has substantially more crimp, so the yarn straightening (uncrimping) occurs gradually until it reaches the yarn elongation region.

Once the crimp is overcome, the actual elongation of the yarns takes place and there is a considerable increase in stiffness. Note that the beginning of the yarn elongation region is in agreement with the measured crimp values given in Table 3.3. For example, for Rijn linen, a crimp value of 0.92 % for the weft and 19.60 % for the warp was measured. It can be seen in the corresponding stress-strain curve for Rijn linen (Fig. 3.12) that the yarn elongation (second linear part of the curve) begins after these crimp values are reached.

The moduli of elasticity considered for the model correspond to the slope of the initial linear part of the stress-strain curve, see Fig 3.12 as an example. The E moduli values for the weft (E_1) and the warp (E_2) directions for the selected materials are given in Table 3.6 with the corresponding standard deviation. The initial elastic modulus was considered for the model assuming that the biaxial tensile loads applied to pre-stretch the canvas are low and within the initial region of the stress-strain curves in which only friction and crimp play a role and no yarn elongation takes place.

The assumption of selecting the initial elastic modulus for the model is valid for aged paintings with a slack canvas since the tension has relaxed over time. Immediately after a canvas has been stretched, it experiences a great amount of relaxation which continues until it reaches a much lower steady value. Many artists wet the canvas and re-stretch it repeatedly to prevent relaxation and remove most of the crimp producing a tight canvas initially. However, after drying, the tension will return to a much lower steady value no matter how many times this process is repeated [68]. The canvas relaxation behaviour was studied experimentally and it is described in Appendix F. It should be noted that wetting the canvas and re-stretching it several times will greatly increase the loads and can cause permanent deformation and enlargement of the canvas. Since the dimensions of the stretcher remain the same, this will produce a slack canvas after it has relaxed over time unless the dimensions of the stretcher are expanded by keying it out.

Recently stretched canvasses with high stretching loads would mean a shift in the region under consideration in the stress-strain curve moving it away from the initial linear region. In this case, a higher elastic modulus should be considered. Permanent deformation of the canvas during stretching will cause hardening of the textile. Therefore, even after relaxation or complete unloading of the canvas, a higher elastic modulus should be considered. If the canvas is then re-stretched, it will have similar regions in the stress-strain curves. However, the initial linear region would have a higher E modulus due to hardening.
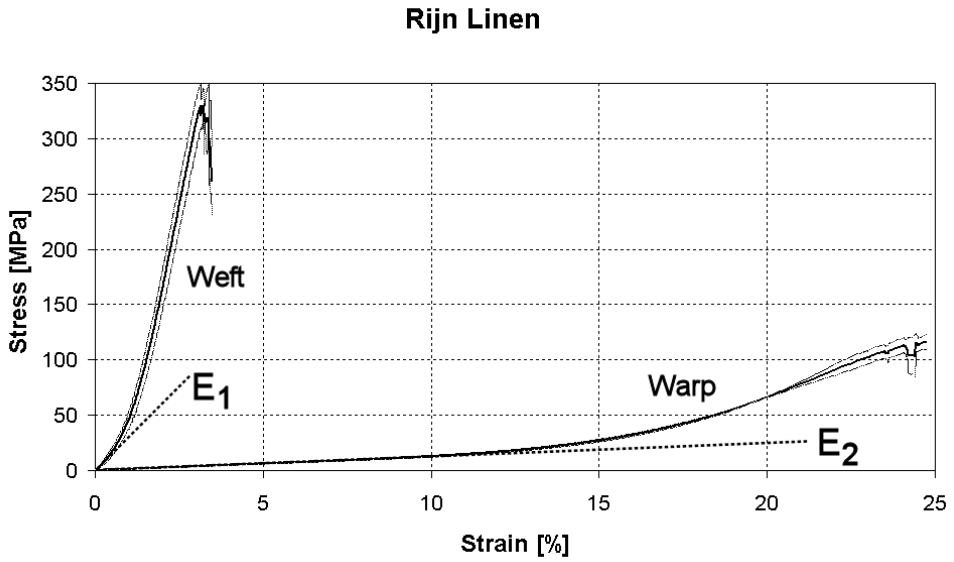
Rijn Linen

Figure 3.12: Stress-strain curve for weft and warp of Rijn linen
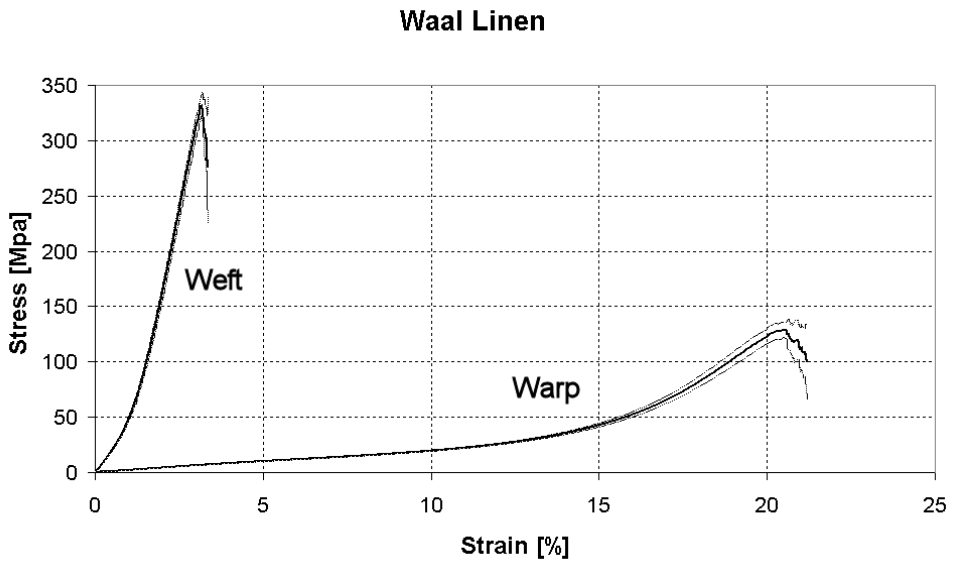
Waal Linen

Figure 3.13: Stress-strain curve for weft and warp of Waal linen
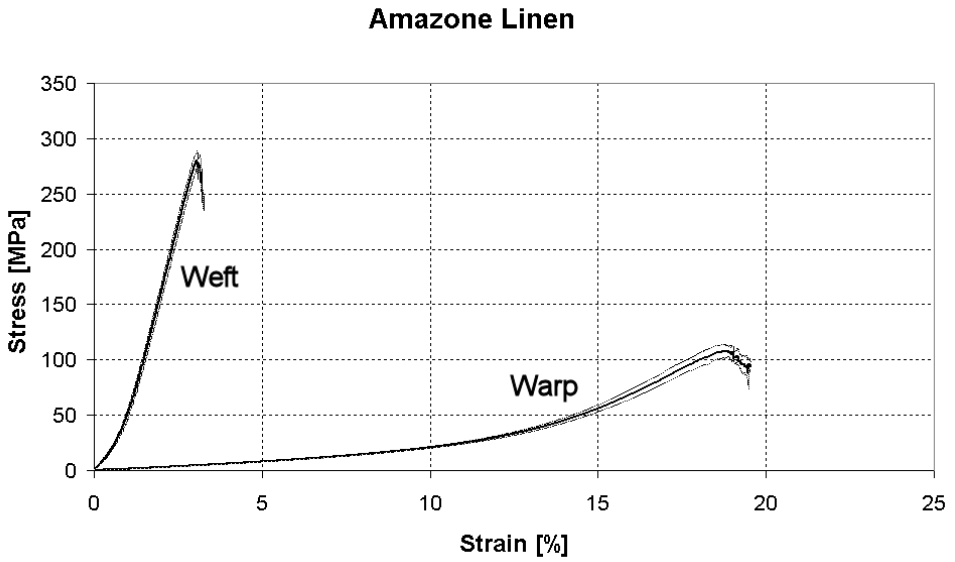
Amazone Linen

Figure 3.14: Stress-strain curve for weft and warp of Amazone linen
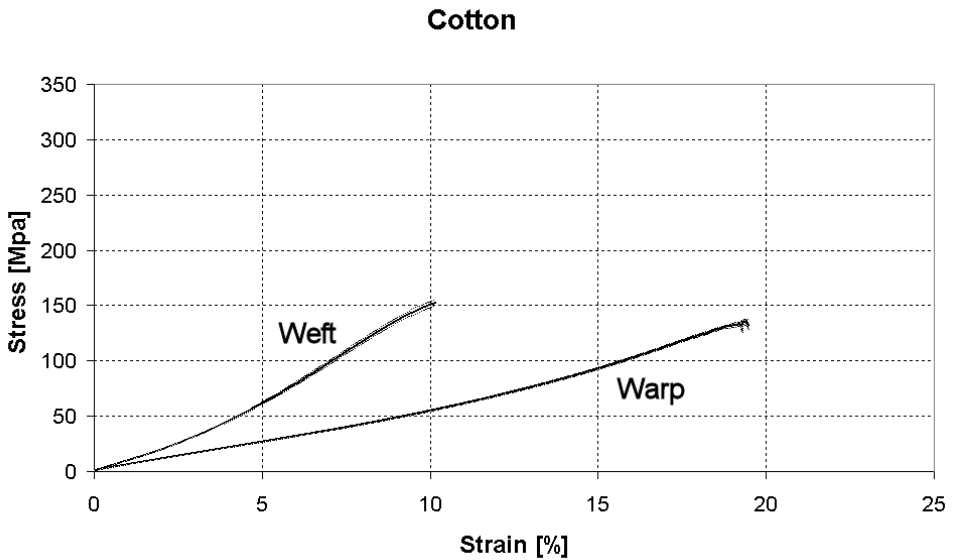
Cotton

Figure 3.15: Stress-strain curve for weft and warp of cotton

Table 3.6: Elastic moduli

Material	Direction	E [MPa]	SD
Rijn Linen	Weft (E_1)	3302	775
	Warp (E_2)	128	6
Waal Linen	Weft (E_1)	3937	204
	Warp (E_2)	207	4
Amazone Linen	Weft (E_1)	3670	422
	Warp (E_2)	158	4
Cotton	Weft (E_1)	939	97
	Warp (E_2)	632	13

An aged canvas would exhibit similar stress-strain behavior (the same regions) but with different values than a new canvas. The aged canvas would be stiffer, more brittle and with a lower ultimate strength than an identical type of canvas in a new state [69], as schematized in Fig. 3.16. An aged painting with a slack canvas would have low tensile loads lying on the initial linear region of the aged stress-strain curve. Therefore the assumption of the initial elastic modulus is still valid, however with the corresponding aged values. Furthermore, on an aged painting, there would be virtually no effect of the paint layers on the tension of the canvas since they are all cracked and the canvas is carrying all the tension.
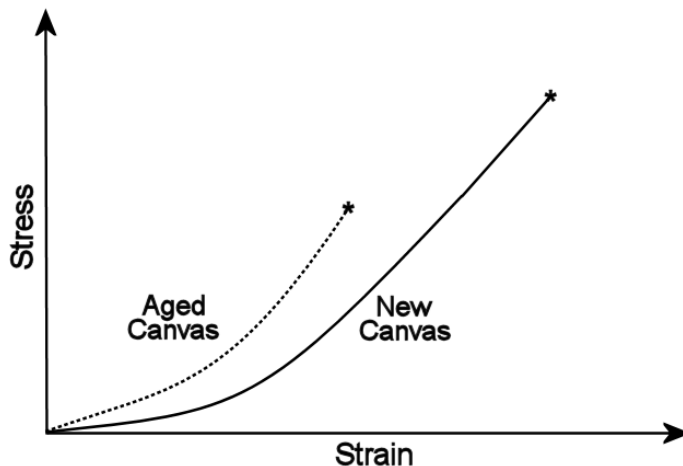
Figure 3.16: Schematic representation of the stress-strain curve for an equivalent new and aged canvas.

In this thesis, new canvasses have been modeled and tested as a starting point. The adequate artificial aging of canvas textiles is a complex process in order to obtain realistic values for different periods of natural aging. For the vibration model, there would not be a significant difference in considering an aged or a new canvas. Only the right E modulus for the initial region of the corresponding stress-strain curve should be assumed. However, for a fatigue analysis the mechanisms for aged and brittle materials would be different than new materials, and thus aged materials would be necessary in that case.

According to the literature, the tension per unit length that a canvas would have would be around 100-300 N/m [68,70] on average. Considering the maximum value of 300 N/m, the corresponding stresses and strains were calculated with the thickness and E moduli values for the selected canvas textiles. All stress and strain values, given in Table 3.7, can be seen to lay within the initial linear region of the stress-strain curves. Therefore, the assumption of the initial elastic modulus is once again justified.

Table 3.7: Stresses and strains calculated for a maximum load of 300 N/m

Material	Direction	E [MPa]	$h_e[mm]$	σ [MPa]	ϵ [%]
Rijn Linen	Weft (E_1)	3302	0.094	3.19	0.09
	Warp (E_2)	128	0.215	1.40	1.09
Waal Linen	Weft (E_1)	3937	0.082	3.66	0.09
	Warp (E_2)	207	0.132	2.27	1.09
Amazone Linen	Weft (E_1)	3670	0.116	2.59	0.07
	Warp (E_2)	158	0.182	1.65	1.04
Cotton	Weft (E_1)	939	0.169	1.77	0.19
	Warp (E_2)	632	0.148	2.03	0.32

Poisson's Ratio

The Poisson's ratio for the textiles has been estimated through a model proposed by Grosberg [71]. In this model, an expression for the Poisson's ratio is obtained as a function of the yarn crimp in the weft (c_1) and warp (c_2) direction by

$$\nu_{12} = -\frac{1 - c_1\sqrt{c_2}}{1 - c_2\sqrt{c_1}} \qquad (3.17)$$

The assumptions made to derive this expression were that the extension of the yarns and the yarn compression can be considered to be negligible during stretching. These assumptions are applicable at low stretching loads where the un-crimping of the yarns takes place and there is no yarn elongation.

The measured crimp values (from Table 3.3) and the corresponding Poisson's ratio (ν_{12}) values calculated with Grosberg's model (Eq. 3.17) for all canvas textiles are given on Table 3.8. Additionally, from the reciprocal theorem of Betti [72] the Poisson's ratio (ν_{21}) was calculated with

$$\nu_{21} = \nu_{12} \frac{E_2}{E_1} \tag{3.18}$$

Table 3.8: Crimp measurements and calculated Poisson's ratios

Material	Direction	Crimp [%]	ν_{12}	ν_{21}
Rijn Linen	Weft (c_1)	0.92	-1.015	-0.039
	Warp (c_2)	19.60		
Waal Linen	Weft (c_1)	1.68	-1.018	-0.054
	Warp (c_2)	18.88		
Amazone Linen	Weft (c_1)	0.96	-1.011	-0.044
	Warp (c_2)	15.04		
Cotton	Weft (c_1)	5.92	-1.023	-0.689
	Warp (c_2)	19.84		

Note that all the Poisson's ratios have a value of approximately -1. This means that if a textile sample is stretched in the weft direction, it will expand in the warp direction with nearly the same amount of strain. Materials that exhibit this unusual behavior are called auxetic materials [73]. On the contrary, the majority of materials have Poisson's ratio values between 0 and 0.5 meaning that if the material is stretched in one direction it will tend to contract in the other transverse directions.

In order to investigate the Poisson effect on canvas textiles, tensile tests were performed on strips of Rijn linen while a series of pictures were taken at the center of the specimen using a CCD camera at a constant frame rate throughout the tensile test. The average strains at the center of the specimens were measured using Digital Image Correlation (DIC) throughout the width (X), and the length (Y) which corresponds to the loading direction. The DIC was performed using a tool developed by Lemmen [74] at the Delft University of Technology.
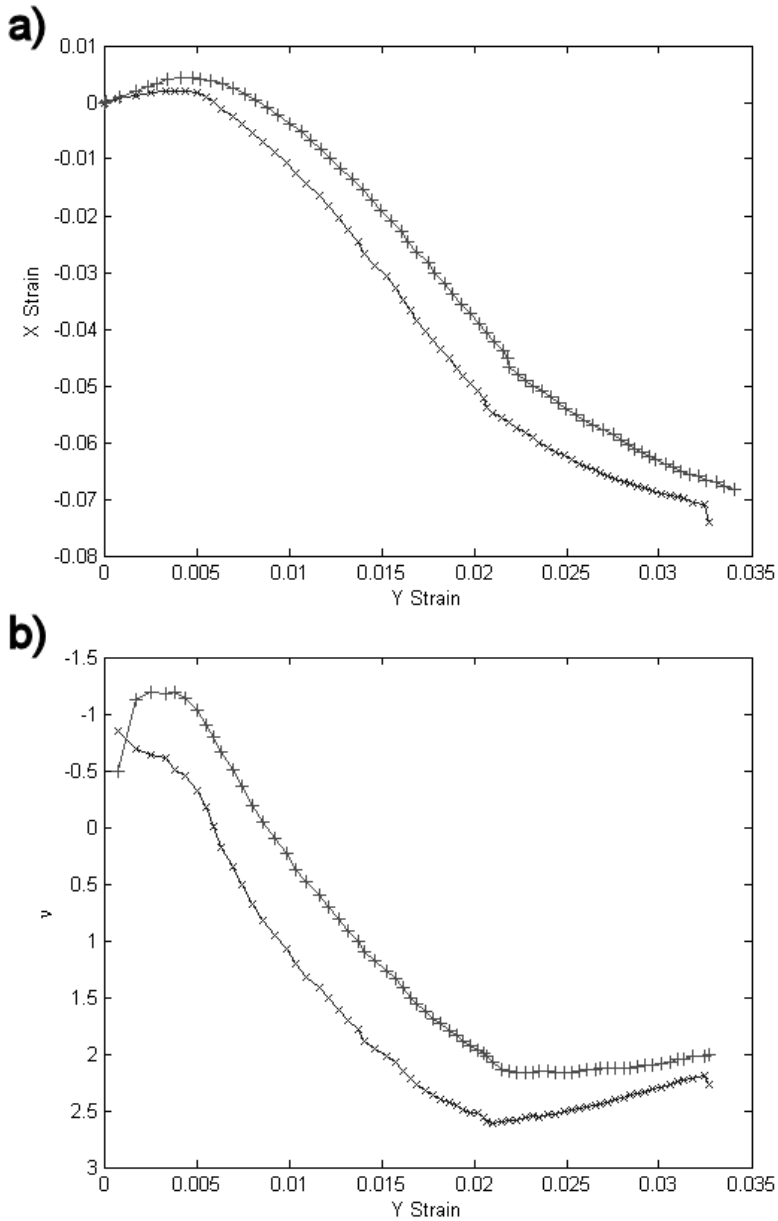
Figure 3.17: a) Transverse and longitudinal strains measured with DIC during a tensile test in the weft. b) Poisson ratio vs. longitudinal strain throughout a tensile test in the weft.

The results obtained for the X and Y strains are shown in Fig. 3.17a. The figure shows the amount of the horizontal strain (X Strain) through the width of the specimen as a function of the vertical strain (Y Strain) where the specimen is being loaded on the longitudinal direction during the tensile test. Note that there are initially tensile strains produced through the width of the specimen which later become compressive strains.

The Poisson's ratio was calculated as $\nu = -X\,Strain/Y\,Strain$ and plotted against the strain in the Y direction as shown in Fig. 3.17b. The results show that the Poisson's ratio is not constant with respect to the strain. There are three main regions which can be identified. In the first region there is a positive strain in the transverse direction which causes the Poisson ratio to be negative. In the second region there is compression in the transverse direction of the specimen and the Poisson's ratio takes a positive value. In the final region the Poisson ratio takes a more uniform value while the specimen is loaded.

Fig. 3.18 shows images from the CCD camera at specific moments in each of these regions at b) Y Strain = 0.005, c) Y Strain = 0.015 and d) Y Strain = 0.03. The reference image with no tension is shown in Fig. 3.18 a). The false colors and colorbar show the transverse X Strain of the specimen measured with DIC. The first region (Fig. 3.18b) with a positive X strain and thus a negative Poisson's ratio (within < 0.01 extensional strain) corresponds to the initial linear part of the stress-strain curve. This behavior can be explained because there is a micromechanical reorientation of the yarns at low loads right before being stretched. It can be observed that the values in this initial region are in agreement with the value predicted by Grosberg's model given on Table 3.8. Once the yarns are reorganized and uniformly loaded there is compression in the transverse direction of the specimen (negative X strain) and the Poisson's ratio takes a positive value (Fig. 3.18c). This occurs in the uncrimping region corresponding to the non-linear part of the stress-strain curve. There is an apparent macromecanical Poisson effect in which the yarns are not actually getting thinner, but the gaps between them get smaller as they straighten out and introduce more crimp in the unloaded transverse yarns. The third region (Fig. 3.18d) corresponds to the actual yarn elongation in which the diameter of the yarn decreases to preserve volume. In this phase, there are no gaps between the yarns and the material starts behaving more like a compact solid. On the stress-strain curve, it corresponds to the final linear region before yarn breakage. It can be observed that in this region the Poisson ratio takes a more uniform value while stretching.

The Poisson's ratio used for the canvas model was the value obtained with Grosberg's model. The assumptions are that the stretching loads are low with

a negative Poisson effect in agreement with the measured values. Additionally the Poisson's ratio is assumed to have a constant value at low strains.

Shear Modulus

The measurement of the shear modulus of textiles is not straight forward. The main reason is that they buckle easily under low shear forces, making it difficult to measure directly. The shear modulus was first estimated with an experimental method, described by Jones [75], for the determination of the stiffness properties of orthotropic plates. The experiment consists of performing uniaxial tensile tests at $45°$ with respect to the principal material directions. The shear modulus G_{12} is determined by

$$G_{12} = \left(\frac{4}{E_{45°}} - \frac{1}{E_2} - \frac{1}{E_1} + 2\frac{\nu_{21}}{E_2} \right)^{-1} \qquad (3.19)$$

given as a function of the E moduli in the two principal material directions, the Poissons's ratio, and the modulus measured at $45°$. This theoretical expression is derived from transformation relations to determine the apparent engineering constants for an orthotropic plate which is stressed in non-principal material directions. The apparent moduli of the plate stressed at an angle ϕ to the principal material direction vary with ϕ as

$$\frac{1}{E_\phi} = \frac{1}{E_1}cos^4\phi + \left(\frac{1}{G_{12}} - \frac{2\nu_{12}}{E_1} \right) sin^2\phi\, cos^2\phi + \frac{1}{E_2}sin^4\phi \qquad (3.20)$$

This relation is obtained from a coordinate transformation in the stress-strain relations of an orthotropic lamina (see Eq. A.8) from one coordinate system to another which is rotated an angle ϕ. The details of this derivation can be found in Jones [75].

Tensile tests at $45°$ were performed on strips of canvas to measure the apparent modulus in this direction. The cross-section area used to normalize the forces was chosen as the effective thickness of the plate model (h_m given in Table 3.5) times the width of the specimen. The measured values of $E_{45°}$ for all the selected materials are given in Table 3.9 together with the corresponding calculated values for G_{12} obtained with Eq. 3.19.

The results show significantly lower values for $E_{45°}$ as compared to the values for E_1 and E_2, which in turn yields low shear moduli values calculated with Eq. 3.19. Preliminary FE simulations show that with these values the
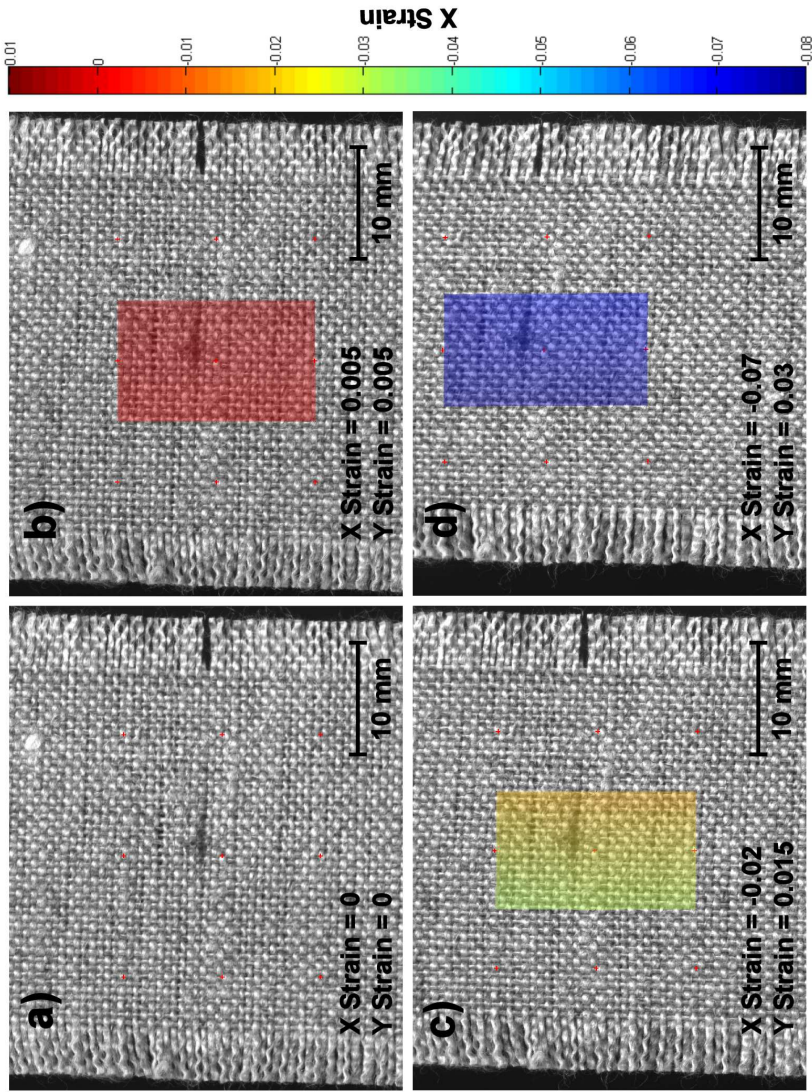
Figure 3.18: Transverse X strain shown in false color, measured with DIC at the center of the specimen during a tensile test in the weft direction Y. The numerical values for both X and Y strains are given as a reference. a) Reference image with no tension. b) Positive X strain of 0.005 for a tensile Y strain of 0.005. c) Negative X strain of -0.02 for a tensile Y strain of 0.015. d) Negative X strain of -0.07 for a tensile Y strain of 0.03.

Table 3.9: Shear moduli using Jones method

Material	$E_{45°}$[MPa]	G_{12}[MPa]
Rijn Linen	32	8.5
Waal Linen	31	8.1
Amazone Linen	17	4.4
Cotton	180	57.5

natural frequencies of the canvas are significantly overpredicted. Reconsidering Eq. 3.19, it can be observed that the shear modulus is highly dependant on the E modulus at 45° and that E_1 and E_2 play a minor role. In other words, it is assumed that under tensile forces at 45° the shear stiffness in the textile is dominant. However, there are several experimental issues that must be considered when measuring $E_{45°}$. The stiffness at 45° is dependent on the length to width ratio of the specimen since for lower ratios, the number of clamped yarns that interact between the top and bottom clamp increases. Thus, lower aspect ratios would be desirable to capture the actual shear behavior in the textile. However, in this case, there is a high clamping effect where the lateral contraction would be restrained by the clamp. Additionally, for an orthotropic material which is loaded in non-principal material directions, there is coupling between normal stresses and shear strains. If the specimen is restrained at the ends, as it is clamped in a tensile testing machine, it will be restrained from shear deformation causing twist towards the specimen's edges. For these reasons, a different approach was considered to estimate the values for the shear modulus.

A model was taken from the literature in order to predict the value for the shear modulus of the canvas plate from the other orthotropic mechanical properties. This model is taken from a refined theory for orthotropic elastic rectangular plates first developed by Huber. The description of the theory can be found in Panc (1975) [76], where both bending and transverse shear effects are considered, as opposed to classical plate theory in which the influence of transverse shearing strains is neglected. The structural plates which generally have elements with different geometric composition, such as stiffened or reinforced plates, are replaced by equivalent orthotropic plates with constant thickness and with the same stiffness properties as the original one. This theory can be used for plates which are symmetric to the mid-plane [77].

The refinement in the theory is performed on the governing differential equation for orthotropic rectangular plates (see Eq. A.22). Huber proposed that the analysis of the orthotropic plate can be simplified if the following relationship holds

$$D_{12} + 2D_{66} = \sqrt{D_{11}D_{22}} \tag{3.21}$$

In this case, the analysis of the plate can be replaced by that of an isotropic plate [78]. Although this relation may not hold exactly, it can be used to derive an approximate expression for the in-plane shear modulus G_{12} as a function of the elastic moduli and Poisson's ratios given by the following expression

$$G_{12} = \frac{\sqrt{E_1 E_2}}{2(1 + \sqrt{\nu_{12}\,\nu_{21}})} \tag{3.22}$$

Comparison of this expression with the isotropic case

$$G = \frac{E}{2(1 + \nu)} \tag{3.23}$$

shows that Eq. 3.22 can be obtained by replacing the geometric mean values $\sqrt{E_1 E_2}$ and $\sqrt{\nu_{12}\,\nu_{21}}$ into the shear modulus and Poisson's ratio of the isotropic equation [76]. It should be noted that Eq. 3.22 is introduced as a first approximation for G_{12} based on purely theoretical considerations.

The relationship between the transverse shear moduli G_{13} and G_{23} given by

$$\frac{G_{13}}{G_{23}} = \sqrt{\frac{E_1}{E_2}} \tag{3.24}$$

is derived in Panc [76] from the reciprocal theorem of Betti $\frac{\nu_{12}}{E_1} = \frac{\nu_{21}}{E_2}$.

The calculated shear moduli values are given in Table 3.10. The in-plane shear modulus G_{12} was calculated with Eq. 3.22 by replacing the E moduli (Table 3.6) and Poisson's ratios (Table 3.8). The transverse shear value G_{13} was assumed to be equal to G_{12}, and Eq. 3.24 was used to calculate G_{23}.

Table 3.10: Shear moduli using Huber model

Material	G_{12}[MPa]	G_{13}[MPa]	G_{23}[MPa]
Rijn Linen	271	271	53
Waal Linen	366	366	84
Amazone Linen	315	315	65
Cotton	209	209	172

The shear moduli calculated with Huber's model given in Table 3.10 have values which are closer to the E moduli values in the weft and warp directions given in Table 3.6, considering that they both originate from the same mechanisms of yarn interactions and friction. Preliminary FE simulations show that with the shear moduli values obtained with Huber's model, the natural frequencies of the canvas get much closer to the experimental values as compared to the frequency values obtained with Jones method. The effect of the shear modulus in the natural frequencies is described in detail in the Discussion Chapter 6.

Bending Stiffness

The bending stiffness is a very important factor which determines the out of plane vibration behavior of the canvas painting. For an orthotropic plate, the bending stiffness coefficients in the weft and the warp directions are given by [79]

$$D_{11} = \frac{E_1}{12(1 - \nu_{12}\,\nu_{21})}h^3 \qquad D_{22} = \frac{E_2}{12(1 - \nu_{12}\,\nu_{21})}h^3 \qquad (3.25)$$

where E_1 and E_2 are the elastic moduli for the weft and the warp respectively, ν_{12} and ν_{21} are the Poisson's ratios and h is the effective thickness of the plate.

Heart Loop Bending tests were performed to measure the actual bending stiffness coefficients of canvas textiles in order to verify whether the chosen parameters for the model (E_1, E_2, ν_{12} and h) yield representative bending stiffness values. The testing procedure described in ASTM standard D1388-96 [80] was followed. In this test, strips of textile for the weft and the warp direction were folded into a heart-shaped loop as shown in Fig. 3.19. The loop was hung vertically under its own weight and the length of the loop was measured. From this measured length, the bending stiffness can be calculated. For details about this calculation, the reader is referred to the ASTM standard D1388-96 [80]. The measured bending stiffness coefficients are given in Table 3.11 together with the bending stiffness values calculated from Eqs. 3.25.

These results show that the bending stiffness coefficients are very low. The bending stiffness in the weft direction is higher than in the warp direction due to the considerably higher elastic modulus in the weft. The measured values are on the same order of magnitude of the calculated values using orthotropic plate theory. The calculated bending stiffnesses for the weft direction are within the standard deviation from the tests for all textiles. On the other hand, the calculated values for the warp direction have up to a factor of two difference compared to the measured bending stiffness for some materials. This
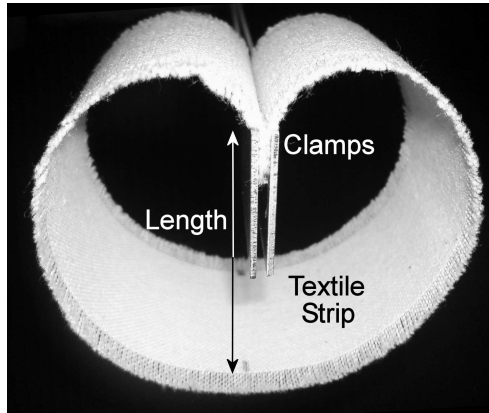
Figure 3.19: Heart loop bending test

Table 3.11: Measured and calculated bending stiffness

Material	Direction	Measured $D[N.mm]$	SD	Calculated $D[N.mm]$
Rijn Linen	Weft	1.234	0.480	0.905
	Warp	0.094	0.015	0.058
Waal Linen	Weft	1.553	0.842	1.205
	Warp	0.029	0.010	0.087
Amazone Linen	Weft	1.247	0.333	0.991
	Warp	0.027	0.008	0.047
Cotton	Weft	0.822	0.314	1.064
	Warp	0.455	0.180	0.716

difference is caused due to the assumption in uniform thickness in plate theory. In the real textile, the bending stiffness in the weft and warp will depend on the number of yarns in the direction under consideration. The different yarn count produce a different effective thickness for the weft and warp direction as discussed previously at the beginning of this section. However, the effect that the difference in measured and calculated bending stiffness coefficients has on the vibration behaviour of the plate is negligible. This was verified with Eq. 3.1 by replacing the bending stiffness coefficient D_{22} by a value a factor two higher which causes only a change of less than 0.01 Hz for the fundamental frequency.

3.3   Finite Element Model

Geometry and Mesh

The 3D model of the vibration of canvas paintings was developed using the FE analysis software package ABAQUS Version 6.8. An overview of the FE method can be found in Appendix B. The painting was modeled as a biaxially loaded cruciform, Fig. 3.20, using the same geometry of the specimens described in Experimental Procedures Section 4.2.

The geometry was meshed with quadrilateral shell elements type S4 with 4 nodes in the corners and an approximate size of 10x10 mm. The vibration zone (center quadrilateral area excluding the cruciform "arms") of the cruciform thus has 1600 (40x40) elements for a 400 x 400 mm specimen, and 1200 (40x30) elements for a 400 x 300 mm specimen (see Fig. 3.20). The number of elements in the vibration zone was chosen as a compromise between an accurate representation of the waveform for the highest mode shape and a low computational time.

The degrees of freedom (DOF) of the FE model are defined at nodal positions where the elements are connected between each other. A rule of thumb is to have at least 9 relevant degrees of freedom per half wave in the x and y directions of the plate [81]. Considering that the mesh must be fine enough to describe mode shapes up to (4, 4) for this case, a total of 36 DOF are required along each direction. Every node has 2 relevant DOF (out-of-plane displacement and rotation) for the x direction and 2 relevant DOF for the y direction; therefore a minimum of 18 nodes (19 elements) are required per edge. Due to the symmetric nature of the problem, it is convenient that the number of elements per edge is even so that nodes are located on the nodal mode shape lines with zero displacement.

In order to simulate the regions where the specimen is clamped, four rigid body constraints were created on the edges of the arms of the cruciform (see Rigid Edges in Fig. 3.20). The material in the clamps will not deform; therefore it will behave as a rigid body. In each rigid body in the model there is one point at which the loads and boundary conditions are applied called a reference point (RP). The reference points (RP$_1$, RP$_2$, RP$_3$, RP$_4$) associated to each rigid body are located at the center of the edges as seen in Fig. 3.20. The loads are applied at the reference points as concentrated forces CF1 and CF2 in the weft and warp directions respectively.
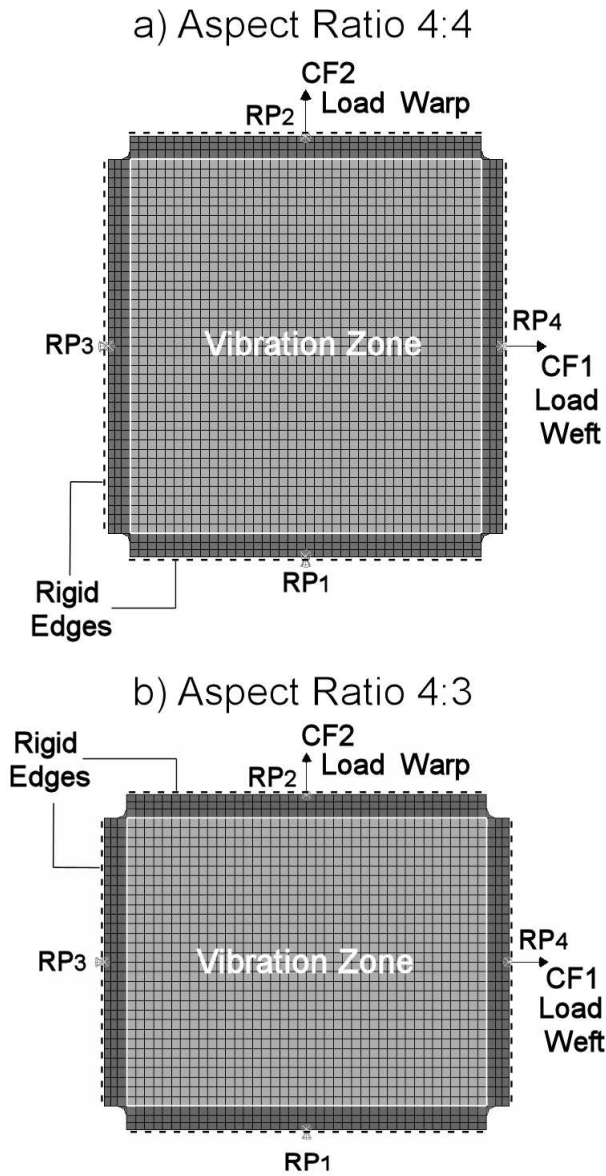
Figure 3.20: Geometry and mesh of FE models for canvas paintings with 4:4 and 4:3 aspect ratios. RP_1, RP_2, RP_3, RP_4 are the reference points to which loads and boundary conditions for the rigid body edges are applied. CF1 and CF2 are the concentrated forces applied in the weft and warp directions respectively.

Materials and Sections

Three different layups were modeled to simulate the tested layer configurations and analyze the influence of each layer. Fig. 3.21 shows a schematic representation of the real and modeled section layups which include a canvas with (a) no ground (canvas alone), a canvas with (b) ground (prepared canvas), and a canvas with a (c) cracked ground.
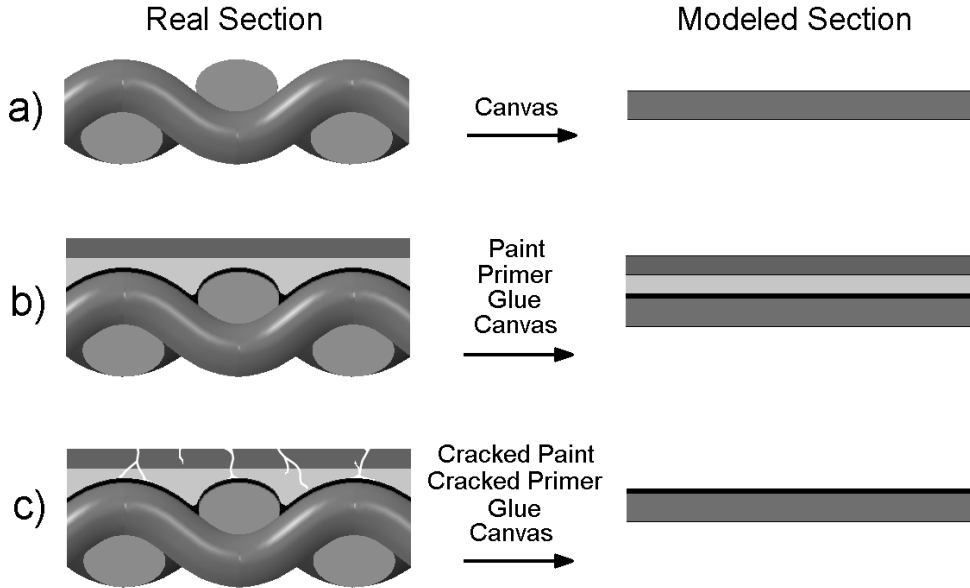
Figure 3.21: Real and modeled sections for a canvas with (a) no ground, (b) ground, and (c) cracked ground (cracked paint not shown; mass density is combined with canvas mass density, see text).

The canvas alone (no ground) was modeled as a single homogeneous shell section. The properties of the section for each one of the canvas textiles are shown on Table 3.12. The shell thickness values were determined from the yarn volume fractions as described previously on Section 3.2. The mass per unit surface area of the shell ($\overline{m}$) was obtained from the values provided by the manufacturer shown in Table 4.1. However the density must be defined in [tonne/mm^2] for unit consistency with the rest of the model. This can be explained, for example, by performing dimensional analysis in the second term of Eq. 3.1 for the natural frequencies of a plate

$$\omega_{mn}^2 = +\frac{\pi^2}{\overline{m}} \left[N_x \left(\frac{m}{a}\right)^2 + N_y \left(\frac{n}{b}\right)^2 \right] \tag{3.26}$$

The corresponding units for the frequency ω $[s^{-1}]$, the force per length N_x $[N/mm]$, and dimensions a $[m]$, are substituted in Eq. 3.26.

$$\frac{1}{[s]^2} = \frac{1}{\bar{m}} \left[\frac{[N]}{[mm]} \left(\frac{1}{[mm]} \right)^2 \right] \tag{3.27}$$

Solving for $\bar{m}$, replacing Newtons by $[Kg \cdot m/s^2]$, and converting meters $[m]$ into millimeters $[mm]$ yields

$$\bar{m} = \frac{[Kg \cdot m/s^2][s]^2}{[mm]^3} = \frac{1000 \, [Kg] \, [mm]}{[mm]^3} = \frac{[tonne]}{[mm]^2} \tag{3.28}$$

Thus, the values for $\bar{m}$ in Table 3.12 are obtained by multiplying the manufacturer values in Table 4.1 ($[gr/m^2]$) by 10^{-12}.

Table 3.12: Section properties for the canvas plate

Material	h_m [mm]	$\overline{m} \times 10^{-10}$ [tonne/mm^2]
Rijn Linen	0.155	2.75
Waal Linen	0.107	2.10
Amazone Linen	0.149	2.10
Cotton	0.159	3.50

The canvas material was defined as an orthotropic lamina and was assumed to show linear elastic behavior. Under plane stress conditions the values of E_1, E_2, ν_{12}, G_{12}, G_{13} and G_{23} are required to define an orthotropic lamina in Abaqus [82]. The values used for the elastic properties of the canvas plate derived in Section 3.2 are summarized in Table 3.13 for each of the selected canvas textiles.

Table 3.13: Orthotropic plane stress material properties for the canvas plate

Material	E_1 [MPa]	E_2 [MPa]	ν_{12}	G_{12} [MPa]	G_{13} [MPa]	G_{23} [MPa]
Rijn Linen	3302	128	-1.015	271	271	53
Waal Linen	3937	207	-1.018	366	366	84
Amazone Linen	3670	158	-1.011	315	315	65
Cotton	939	632	-1.023	209	209	172

A laminate (composite) shell section was defined in order to model a canvas with a ground layer. From the selected canvas textiles described in detail in

Section 4.2, only the linen canvases were considered for modeling and testing with a ground layer since a prepared version of the cotton canvas was not available for purchase. The prepared linen materials were manufactured all in the same way by the canvas supplier Claessens located in Waregem, Belgium. The canvas is first sized with a PVA glue layer. A layer of oil based Zn white primer and a layer of Ti white paint are then applied. Therefore, the laminate layup for all linens is similar but with a different textile support material. An example of the laminate layup for Rijn linen with ground is shown in Table 3.14.

Table 3.14: Laminate section properties for Rijn linen with ground

Layer	Material	Thickness [mm]	$\overline{m} \times 10^{-10}$ [tonne/mm^2]
1	Rijn Linen	0.155	
2	PVA Glue	0.005	4.57
3	Zn White Primer	0.015	
4	Ti White Paint	0.010	

The values of the thicknesses for each layer were measured under the Scanning Electron Microscope (SEM) on cross-section samples. Figure 3.22 shows SEM photographs for Rijn and Waal linens as an example. The glue layer is very thin and not flat, following the weave pattern at one side of the surface of the canvas as shown in Fig. 3.21b. The glue mingles with the fiber surface producing a composite interface made up of glue matrix and textile fibers from the yarns. In the model, the composite interface is not considered and the glue layer is taken as a uniform flat very thin layer. The Zn white primer is used as a filler material in order to cover the voids in between the woven yarn. Thus, the layer is not a flat film but rather follows the pattern of the weave (already with glue) on one side, with a nearly flat surface on the other side. For the model it is assumed that this layer is flat and homogeneous, with a uniform thickness equal to the average between the maximum and minimum measured thicknesses of the real layer. The Ti white paint is applied for a surface finish over the filling material so it has a fairly homogeneous thickness. For the model, the thickness considered is the average of several measurements taken. The mass per unit area was defined for the entire laminate section corresponding to the factory values for canvas with ground shown in Table 4.1.

The glue, primer and paint layers were defined as linear elastic isotropic materials. The input mechanical properties for these materials are given on Table 3.15. The values for the elastic moduli were measured by performing
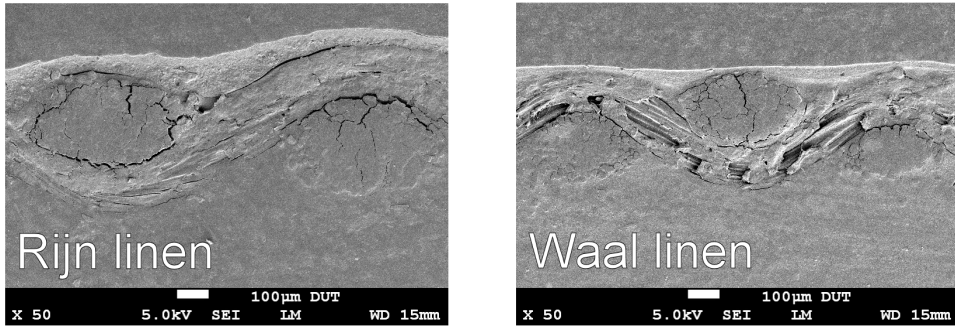
Figure 3.22: Scanning Electron Microscope photographs of cross-section samples of Rijn and Waal linens.

tensile tests on thin film samples as described in Appendix D. The Poisson's ratio was assumed to be 0.4 for fresh samples, as an average between 0.3 corresponding to "glassy" materials, and values of 0,5 for "rubbery" materials [83]. In the case of traditional oil paintings, the glue, ground and paint layers can still be considered as linear isotropic materials, however the corresponding values for the modulus of elasticity should be considered with a Poisson's ratio of 0.3 due to the brittleness of the aged materials.

Table 3.15: Material properties for glue, primer and paint layers

Material	E_g [MPa]	ν
PVA Glue	50	0.4
Zn White Primer	120	0.4
Ti White Paint	70	0.4

Cracked paint layers were assumed to have negligible contribution to the stiffness of the canvas, thus they were modeled only as additional mass. In order to model a canvas with a cracked ground layer (Fig. 3.21c), a laminate section formed only of the canvas and the glue layer was defined, since only the Zn white and Ti white layers were cracked in the tested specimens. However, the density was defined as the value for a canvas with a ground layer since the mass of the cracked paint is still considered. An example of the layup for Rijn linen with a cracked ground is shown in Table 3.16.

Table 3.16: Section properties for Rijn linen with a cracked ground

Layer	Material	Thickness [mm]	$\overline{m} \times 10^{-10}$ [tonne/mm^2]
1	Rijn Linen	0.155	4.57
2	PVA Glue	0.005	

Analysis Steps

The FE analysis was performed in three steps as defined in Abaqus:

1. Static Analysis: The initial static step simulates the biaxial stretching of the canvas and defines the base stress state for the dynamic analysis. Geometric non-linearity is considered in this step and propagated to further steps in order to include the stress stiffening effect of the pre-stretching in the dynamic analysis.

2. Frequency Extraction: A frequency step is then carried out to extract the natural frequencies and modes of the structure. In this step, the free vibration problem is solved. The natural frequencies obtained in this step can be compared to the measured natural frequencies in order to verify the model.

3. Mode-based Steady-State Dynamic Analysis: This step simulates the behavior or response of the painting under vibration excitation (forced response) over a range of frequencies. The response is considered as a superposition of the eigenmodes extracted in the previous step. The vibration amplitudes that the structure will have when excited at different frequencies depends on its natural frequencies and modes (obtained in previous step), and the damping (extracted experimentally). More specifically, when the excitation frequency is far from a natural frequency, the vibration amplitudes are low. As the excitation frequency gets closer to the system's natural frequency, the vibration amplitudes increase up to a maximum value where the excitation frequency matches the natural frequency (resonance) (see for example Fig. 4.1). Additionally, the forced vibration amplitudes have an inverse relation with the damping; this is, for higher damping ratios the amplitudes are lower and vice versa. The amplitude response as a function of frequency obtained in this modelling step can be compared to the experimental amplitudes measured throughout a range of excitation frequencies (sweeps). Therefore the dynamic behaviour of the model over an entire frequency range can be verified.

See Appendix B for an overview of the finite element method and the analysis steps.

Loads and Boundary Conditions

The loads and boundary conditions for the static step applied on the rigid body reference points (RP) are shown in Fig. 3.23. The stretching process was simulated by suppressing the vertical displacements ($\delta_y = 0$) at the bottom edge (RP_1) while the opposite edge was loaded vertically at RP_2 with a Concentrated Force (CF2) equal to 5, 10 or 20 kg (49, 98 or 197 N) that correspond to loads per unit length of 122.5, 245 and 490 N/m accordingly with the tested loads described in detail in Section 4.3. These values were defined by taking into account a reference value of 200 N/m found in the literature as a representative value of the tension that the canvas has when mounted on a stretcher [70], and considering an upper limit value of 500 N/m that was measured as the maximum value that can be applied by hand with a pair of canvas pliers.

The same procedure was carried out for the horizontal axis, that is, suppressing the horizontal displacements ($\delta_x = 0$) at the left edge (RP_3) and applying a horizontal concentrated force (CF1) at the right edge (RP_4). However, in order to have the same load per length in the 300 mm edge specimen, the values of the loads (CF1) were 3.75, 7.5 or 15 kg (36.75, 73.5 or 147 N). The out of plane displacements for all four RP were suppressed ($\delta_z = 0$), that is, assuming that the clamps remain in the plane of the plate.

For the frequency extraction and the modal dynamic step, the cruciform arms were fixed in all coordinates (encastered), that is, it was assumed that the clamps do not move during vibration. The first 10 eigenmodes were requested in the frequency extraction and the forced response was analyzed based on these modes. The response was requested over 200 integration points and direct modal damping (see Appendix B) was defined over the modes. The average values for the damping ratio extracted from the tests were $\zeta = 0.01$ for ground and cracked ground, and $\zeta = 0.2$ for no ground. The harmonic excitation was defined as a surface pressure (see Fig. 3.24) simulating the acoustic waves coming from the excitation source as described in Section 4.4. The value for the pressure $3, 4 \times 10^{-5}$ [MPa] was measured with a microphone at the end of the cone of the acoustic driver. A Bruel and Kjaer (B&K) Microphone with a nominal diameter of 1/4" model Type 4136 with a linear frequency response characteristic up to 10 kHz was used. Additionally, a 1/4" Microphone Preamplifier Type 2633 was used with a Microphone Power Supply Type 2804 both manufactured by B&K.
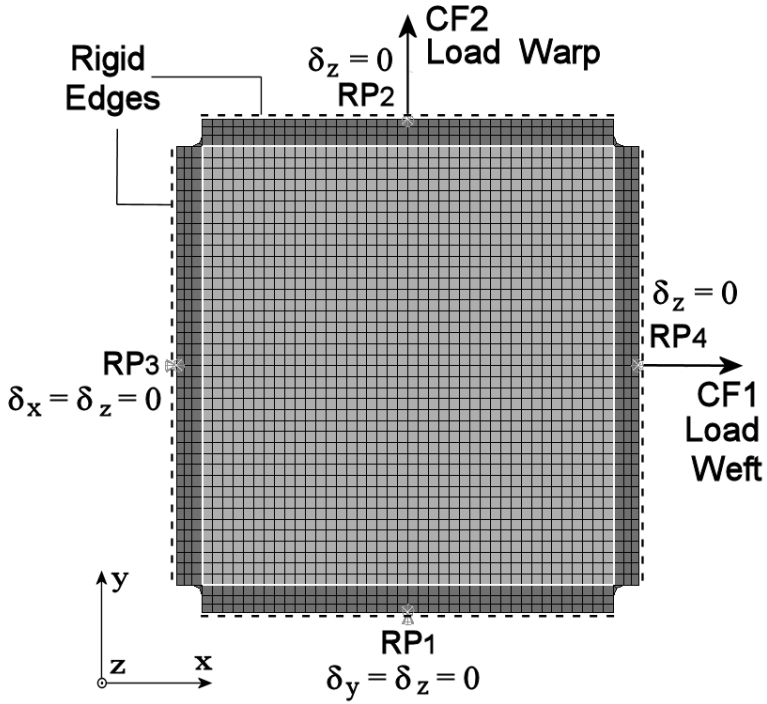
Figure 3.23: Boundary conditions and loads for the static step.
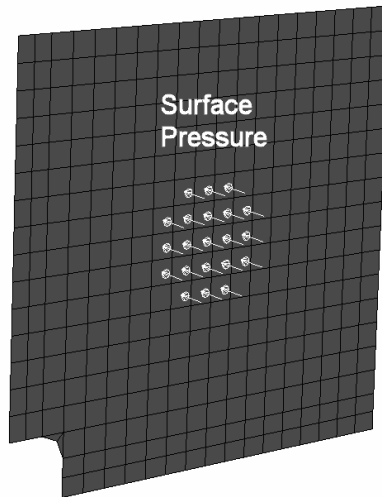
Figure 3.24: Pressure load for the forced response step.

The result of these FE analysis steps will yield the values for the natural frequencies and corresponding mode shapes of the painting model which will be dependent on the previous static (stretching) step. Based on this frequency extraction, the forced response of the canvas to a harmonic pressure loading simulating the acoustic excitation in the experimental setup can be obtained. The forced response step yields an amplitude response plot as a function of the frequency (see Fig. 4.1). This response plot will be equivalent, experimentally, to sweeping the canvas specimen with an acoustic source through a frequency range. The predicted natural frequencies, mode shapes and amplitude response plots can be compared to the measured values in order to verify the model experimentally.

Chapter 4

Experimental Procedures

In this investigation experiments were carried out in order to verify that the dynamic model proposed is truly representative of real canvas paintings. The verification was performed by following a procedure called modal analysis. The basic idea in modal analysis is to measure the natural frequencies and mode shapes of a real test object and compare them to those predicted by the model. If they agree, the model can then be used to predict the response of the object to different types of loading.

In modal analysis, the concept of resonance is used to identify the natural frequencies of a structure experimentally. Forced vibrations are applied to a point in the structure. The response to a range of frequencies is measured at a different location in the structure. Fig. 4.1 shows a schematic plot of the response amplitude as a function of frequency. At resonance the driving frequency matches the natural frequency of the structure, and provided that the damping is small, the magnitude of the measured response reaches a peak value [84]. These natural frequencies are denoted in Fig. 4.1 as f_1, f_2, f_3.

4.1 Vibration Testing System

A vibration testing system, shown schematically in Fig. 4.2, was built to determine the natural frequencies and mode shapes of canvas specimens. The system consists of a stretched canvas specimen, an acoustic excitation system and a laser measurement system. The canvas specimen is first stretched with a biaxial stretcher. It is then excited throughout a frequency range with an acoustic driver (loudspeaker and cone) which produces sound pressure waves. A laser vibrometer is used to measure the response of the canvas.
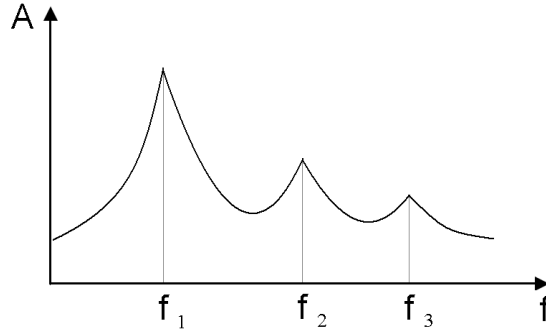
Figure 4.1: Schematic plot of the amplitude response as a function of frequency.

An acoustic excitation system was chosen because it provides an adequate and straightforward method to excite specific mode shapes in the canvas specimens to correlate them with the FE modal data. It is a non-contact method which makes it possible to excite the canvas specimen at particular locations in order to trigger the vibration modes of interest and obtain clear mode shapes (see Section 4.5), while the boundary conditions (representing the support from the stretcher) remain fixed. It is important to note that in reality the majority of vibration loads would be transferred through the stretcher. However, this would involve movable boundary conditions and a different type of analysis (Base excitation) would be required. Experimentally, if the excitation comes from the frame, only the fundamental mode shape would be easily triggered. Higher modes would be harder to trigger clearly even though they will contribute to the response of the canvas at those higher frequencies. The natural frequencies and mode shapes of the painting are independent of the way it is excited since they are intrinsic properties of the system. Thus, the painting will have the same natural frequencies whether it is excited through the frame or acoustically. On the other hand, the forced response will change for different types of excitation even though it is based on the same natural frequencies. Therefore, the acoustic excitation method is appropriate for modal analysis but not to recreate transport conditions for example.

A non-contact laser measurement system was chosen for vibration measurements over conventional accelerometers which can add significant mass causing a change in the dynamic properties of the canvas. This method allows measurement at any point in the specimen without interfering directly with the structure.
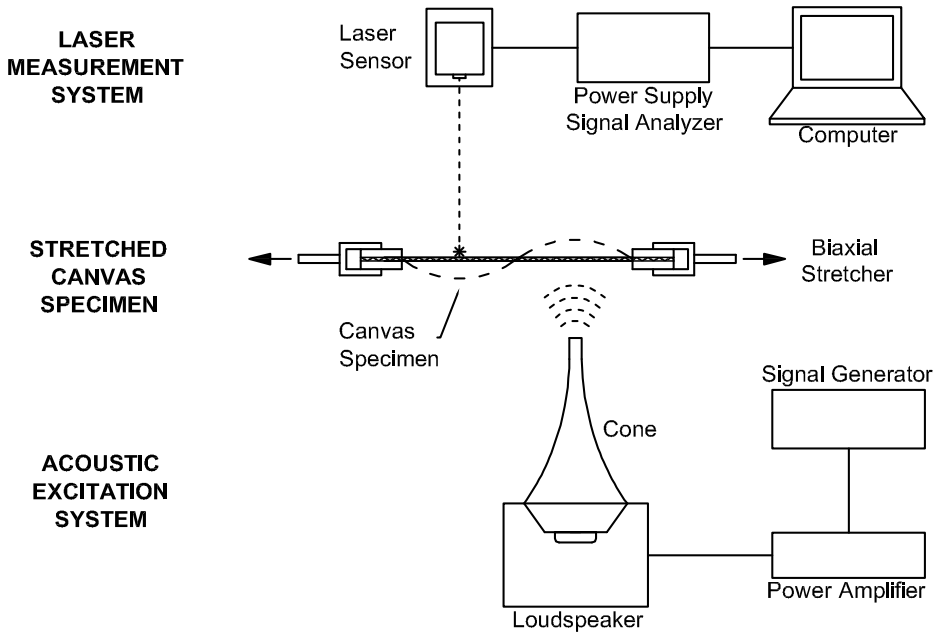
Figure 4.2: Schematic of the vibration testing system and its components.

4.2 Materials and Specimens

The canvas materials that were selected for modeling and testing are shown in Table 4.1. The selected textiles are specified by their raw material, the weave structure, the number of threads per centimeter (yarn count) and the area density expressed in grams per square meter. The most common types of materials used as canvas supports are linen and cotton. Linen has been the traditional choice by artists. For this reason three linen canvasses and one cotton canvas were selected. All of the linen canvasses had a plain weave structure, see Fig. 2.1a. The cotton canvas, on the other hand, had a rib weave with two warp yarns woven under and over a single weft yarn, see Fig. 2.1b. The "Waal" linen was chosen as an example of a balanced weave, that is with the same yarn count in both the weft and warp directions. The other canvasses were unbalanced, having different yarn counts in the weft and warp directions. A generalized overview of the behavior of canvas supports can be obtained by studying this range of materials with different characteristics.

Prepared linens were also selected to investigate the effect of ground and paint layers on the selected canvasses. All selected linens were prepared by the manufacturer [85] in the same way with oil based ground layers. The canvas

Table 4.1: Nominal properties of selected canvas textiles.

Material	Weave	Count [yarns/cm]		Weight [gr/m^2]	
		Weft	Warp	No Ground	Ground
Rijn Linen	Plain Unbalanced	14.5	17	275	457
Waal Linen	Plain Balanced	23	23	210	325
Amazone Linen	Plain Unbalanced	16	20	210	385
Cotton	Rib Unbalanced	20.5	41	350	—

textiles were first coated with a layer of PVA glue (polyvinyl alcohol glue) and dried in a hot air tunnel for 10 minutes. Then a primer layer made of zinc white and chalk was applied as a filler material and dried for 3 days. Finally, a layer of titanium white paint was applied as a surface finish and dried for 10 days. Both oil primer and paint contained the necessary siccatives and were dried in open air. The prepared linens with canvas, ground and paint layers were modeled as laminated plates as described in detail on page 48 of the finite element model in Section 3.3.

On traditional oil paintings, the most common materials used for the preparation of canvasses included animal glues, lead white, chalk and gypsum. However, in this investigation, contemporary factory-made oil prepared canvasses were used for modelling and testing due to several reasons. The first reason was to start simple with readily available materials since the preparation of accurate traditional "recipes" with the right composition and techniques is a complex procedure. Additionally, factory-made materials allow having consistency in prepared specimens in order to obtain comparable results for different tests performed. Furthermore, most traditional and contemporary materials used in oil paintings will have similar mechanical properties an can be modeled in the same way. However, when modeling traditional materials the corresponding values for the mechanical properties must be used as input for the model.

The selected materials were tested with different layer configurations: the canvas, the canvas with a ground layer, and the canvas with a cracked ground layer. The cracks were artificially introduced by immersing the specimen in liquid nitrogen and then bending the specimen until the paint layers were completely covered with transverse cracks. These layer configurations were chosen for testing in order to compare them to the finite element model that was built progressively, beginning with the canvas on its own, and then adding layers and increasing the complexity up to a sensitive painting with cracked paint layers. This approach also permits an understanding of the effect of each layer on the overall behavior of the structure.

The canvas specimen must simulate the way a real painting is stretched on a frame. A biaxial stretcher (described in the following Section 4.3) was built to replicate the tension of a real stretched canvas, while allowing for control and monitoring of the loads at the same time. The specimens for vibration testing were cut from the materials into a cruciform geometry, Fig. 4.3, to allow for clamping on the biaxial stretcher. The edges of the cruciform were cut parallel to the weft and warp so that the biaxial loading could be applied in those weaving directions. A small fillet was left between the arms of the cruciform in order to reduce the stress concentration in the corners. Two specimen geometries were prepared for testing, the same as considered for FE modeling, compare Fig. 3.20 and Fig. 4.3. These geometries were tested in order to verify that the general model works for different sizes of paintings. The tests that were carried out for the different canvas materials, aspect ratios and preparation layers are given in Table 4.2.
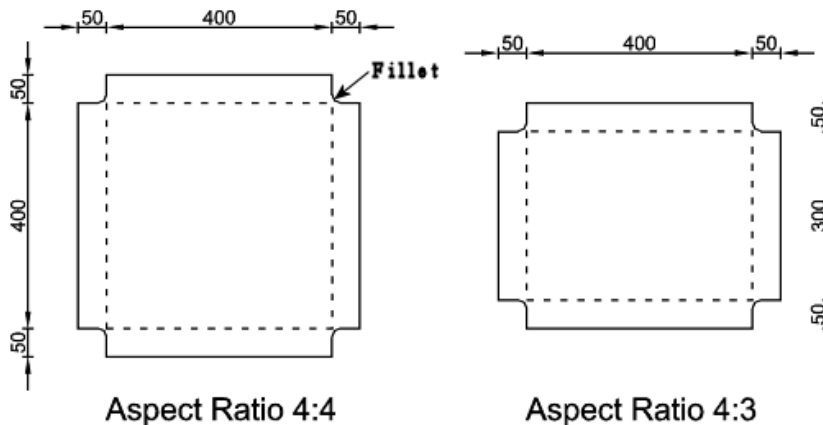
Figure 4.3: Canvas specimen geometries and aspect ratios.

Table 4.2: Tested canvas specimens.

Layers	No Ground		Ground		Cracked Ground	
Aspect Ratio	$4:4$	$4:3$	$4:4$	$4:3$	$4:4$	$4:3$
Rijn Linen	✓	—	✓	—	✓	✓
Waal Linen	✓	—	✓	—	✓	✓
Amazone Linen	—	—	—	—	✓	✓
Cotton	✓	✓	—	—	—	—

The physical properties of textiles are generally influenced by the relative humidity and temperature. In order to make reliable comparisons among the different materials tested, the specimens were left in the testing room

for one day before testing to let them stabilize at its temperature and relative
humidity (21°C and 50% RH). These values are in agreement with the standard
atmospheric values for testing specified in the ASTM Standard Practice for
Conditioning Textiles for Testing [86].

4.3   Biaxial Loading

A diagram of the biaxial stretcher is shown in Fig. 4.4. It consists of a four-
sided frame constructed of square steel tube that provides support for two
orthogonal and independent loading axes. The design criterion for the steel
frame was to minimize the deflection at the midpoints so that the deformation
occurs mainly in the specimen. Each loading axis is equipped with two power
screws that move the specimen clamps. The screws have a fine pitch to allow
accurate control of the displacement of the clamps which slide over lubricated
guides.   The clamps can be rotated at the base of the screw to align the
specimen when mounting it. There is one load cell for each loading axis to
measure the force applied to the specimen while the screws are tightened.
The detailed design considerations for the biaxial stretcher can be found on
Appendix E.

The stretching loads used for testing were 122.5, 245 and 490 N/m (corre-
sponding to 5, 10 and 20 Kg applied to a 0.4 m specimen edge). These were
determined based on the literature where a representative load that a canvas
would have when mounted on a stretcher is given as 200 N/m [70]. This value
was confirmed by performing measurements of the force applied manually with
a pair of canvas pliers on a canvas specimen. Additionally, with these mea-
surements a maximum force value of about 500 N/m was determined as the
force limit that can be applied by hand. The same load values per unit length
were applied in the weft and the warp directions. For specimens with a shorter
cruciform arm, the load was reduced in order to provide the same load per
length. For example, a load of 7.5 Kg was applied to a 300 mm long specimen
while a load of 10 Kg was applied to a 400 mm long specimen, both yielding
an equivalent edge load of 245 N/m.

The canvas textiles exhibit viscoelastic material properties. If they are
stretched and then constrained at a constant deformation, the stress required
to keep it in the deformed state relaxes. To minimize the relaxation of the
canvas during vibration testing, the canvas was loaded and allowed to relax,
repeating this process for three times before performing the test. This caused
the load to remain more constant during the test. A description of the re-
laxation tests that were performed in order to study this phenomenon can be
found in Appendix F.
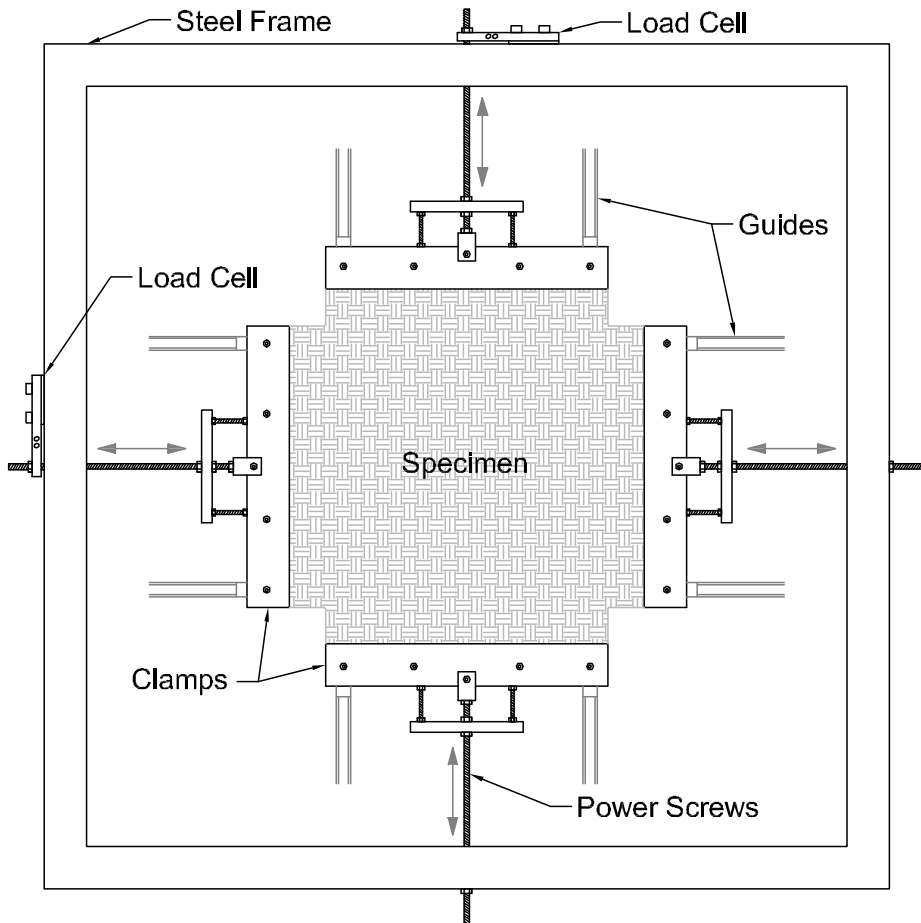
Figure 4.4: Schematic of the biaxial stretcher and mounted specimen.

The procedure of relaxation and re-stretching done previous to vibration testing is schematized in Fig. 4.5 as an example based on the actual weft stress-strain curve for Amazone linen with a stretching load of 20 kg. The curve was manually modified to simulate this process and verify if the load remains within the initial linear region afterwards. The initial stretching occurs until the equivalent stress at a load of 20 kg (3.5 MPa) and at this point the load was dropped to 90% at constant strain simulating the relaxation during the test. Then to simulate the re-stretching, the loading continues through the stress-strain curve starting at the same position were it was allowed to relax until it reaches again the required value of 20 kg (3.5 MPa). The load was allowed to relax once again until 90% of its value. Finally, the canvas is re-stretched once more starting at the position in the curve where it was allowed to relax the second time until it reaches the required load again. From this figure it can be seen that after the repeated stretching and relaxation, the load remains within the initial linear region (up to about 0.5% strain) of the stress-strain curve and thus the assumption of the initial E modulus is still valid. This is a representative example shown for the maximum load of 20 kg and for the weft direction since the initial linear region is significantly smaller than for the warp direction. However, this was also verified for all the canvas textiles for the weft and warp directions.
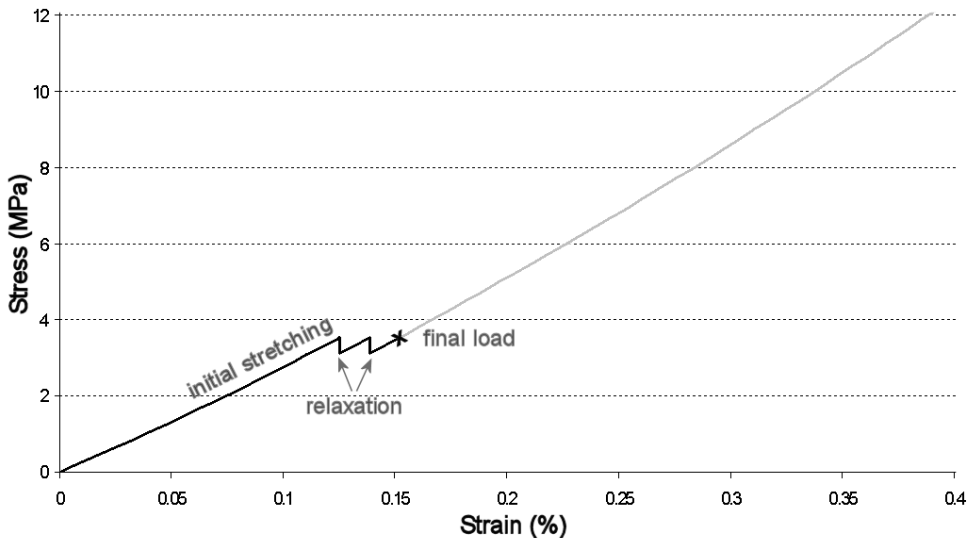
Figure 4.5: Stretching and relaxation procedure previous to vibration testing for Amazone linen weft direction with a stretching load of 20 kg.

4.4 Acoustic Excitation

An excitation system was used which was already available in the laboratory, built for a previous PhD project which studied the vibration of cylindrical shells. The system consists of a frequency generator model GN 484 manufactured by PRODERA Modal Analysis Systems and Software, a high efficiency power amplifier model SA 800 manufactured by Stage Company®, and an acoustic driver composed by a loudspeaker and an exponential cone. Details of the design and construction of the acoustic driver can be found in the doctoral thesis by Gunawan [87]. The operation of the system consists of producing a frequency of interest or a frequency sweep with the generator. The signal is then amplified and converted into sound pressure waves by the loudspeaker. The pressure waves are guided and concentrated by the exponential cone so that a specific part of the canvas can be excited.

Frequency Sweeps

A frequency range of 15 Hz to 100 Hz was used for the experiments which includes the main natural frequencies. This range was chosen based on experience in the field. The frequency content for common vibration sources such as highway traffic, building services, handling equipment, etc., typically ranges from 4 to 100 Hz with a peak at 40 Hz [88] due to an overlap of most sources at this frequency. Furthermore, preliminary experiments showed that the first mode for these test configurations occurs between 15 and 50 Hz depending on the specimen layers and the applied tension. As a consequence, the lower vibration modes will be excited and will be the dominant ones in the behavior of the structure. Moreover, the low modes and especially the first vibration mode are the most dangerous because higher amplitudes are associated with these modes.

The frequency generator was set to produce an exponential frequency sweep governed by the following equation

$$f_{dr} = f_o \, e^{0.01t} \tag{4.1}$$

where f_{dr} is the driving frequency which is a function of the initial frequency f_o, and the time, t. The value of 0.01 corresponds to the rate of the exponential increase in frequency given in (Hz/s)/Hz. This sweep function was chosen because it produces a sufficiently slow frequency increase at low frequencies which are the most important ones, and a faster increase at high frequencies. In this way the required frequency interval can be covered in a reasonable time

(about 160 s) without generating an excessive amount of vibration data.

Volume of acoustic source

The volume of the acoustic source was chosen so that the measured amplitudes are sufficiently high to be detected by the laser and not lost in the noise of the signal. At the same time the amplitudes must be sufficiently low so that the system behaves linearly. When the amplitude of vibration reaches the same order of magnitude of the thickness of the plate, then the application of linear theories begin to lose accuracy [89]. Preliminary experiments were conducted to measure the value of the amplitudes reached at resonance with different volume levels. The results indicated that the amplitudes can reach detectable peak values at low volumes of the power amplifier due to the proximity of the excitation. The sound pressure at the end of the loudspeaker cone was measured with a 1/4" microphone Type 4136 with a preamplifier Type 2633 and a power supply Type 2804 manufactured by Bruel and Kjaer. A pressure value of 34 Pa was measured at the end of the cone which would be representative of the sound pressure produced by a rock and roll band in a small hall [90].

4.5   Laser Measurement

The canvas vibration measurements were performed using a non-contact laser interferometric vibrometer Model SP-S 120 manufactured by SIOS Meβtechnik GmbH, Ilmenau, Germany. The measurement system consists of a laser sensor head, a power supply/signal analyzer unit, and a computer. The laser beam exits the sensor head and is reflected on the vibrating surface and back into the sensor where a miniature interferometer (modified Michelson interferometer) produces interference patterns by overlapping the reflected light wavelength with a reference wavelength. The interference patterns can be directly related to the displacement of the measured surface due to the stable wavelength (633 nm) of the He-Ne laser used. High precision vibration measurements are possible with a resolution of 0.3 nm. The optical output signals from the interferometer are transmitted by a fiber optic cable to the power-supply/signal-analyzer unit. The optical signals are then converted into electronic signals, processed and displayed on a computer that runs the specialized data-analysis software provided by the manufacturer. With this software, the output data can be saved for post processing and analysis [91].

The laser was mounted on an aluminum profile support structure. The laser support structure and the biaxial stretcher were both fixed over a table, and the acoustic driver was positioned to excite the specimen from below

through an opening in the table as shown in a photograph of the test setup, Fig. 4.6. The laser fixture is movable in all three linear axes in space, allowing the measurement of any point on the surface of the specimen, and the adjustment of the distance from the sensor to the specimen to set the optimum working distance.
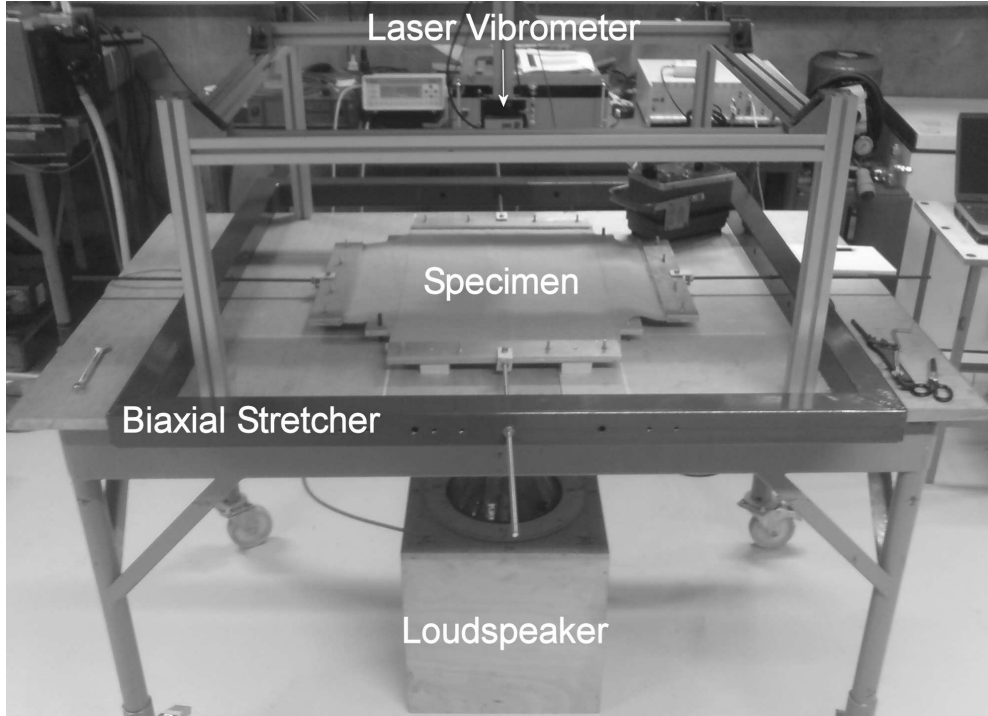
Figure 4.6: Photograph of vibration test setup.

Excitation and Measurement Locations

The measurement and excitation locations were determined before testing according to the vibration modes of interest. Fig. 4.7 shows three vibration modes visualized in two dimensions to illustrate this. The modes have inflection points called nodes (not to be confused with FE nodes) at every half wave in which the amplitude would theoretically be zero. The excitation and measurement should be performed at the antinodes where there are maximum deflections for a particular mode. Initial experiments showed that the behavior of the structure is governed primarily by the first four vibration modes. These can be triggered and detected by measuring and exciting at the antinodes of different quadrants of the specimens depending on their aspect ratio.
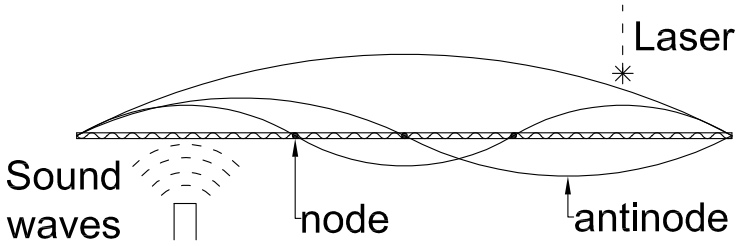
Figure 4.7: Diagram showing the excitation and measurement locations.

A drawback of the laser system is that only one measurement point is possible at a time for each frequency sweep. However, in order to identify mode shapes it is necessary to know the behavior of the entire surface. The initial approach was to map the surface by measuring at different locations. However, this method was very time consuming and presented slight shifts in the frequency peaks from point to point due to the relaxation of the specimen in between measurements. A complementary method to visualize the mode shapes was with a stroboscope. A stroboscope is an intermittent light source that illuminates the surface at a certain frequency. If the light is flashed at the same frequency as the vibrating surface, the object will appear to be stationary. However, if the light flashes at a frequency close to but not equal to the vibrating frequency, then only specific moments of the vibration cycle can be observed making them appear in slow motion [92]. In this way the mode shape of the vibrating canvas can be observed with the naked eye.

To apply this method the vibration response was first measured with the laser at a single location. From this measurement the natural frequencies were identified by observing maximum amplitudes. The specimen was then excited specifically at these natural frequencies while illuminating the surface with a stroboscope to observe the corresponding vibration modes. This method is very useful but is limited to low frequency modes with high amplitudes. For higher modes, the amplitudes are low and the mode shapes are not clearly visible.

Laser Shearography

With the stroboscope method it was only possible to clearly observe the fundamental mode in the canvas specimen, thus a method called laser shearography was used to measure mode shapes with lower amplitudes at higher frequencies in order to compare them to the predicted mode shapes by the finite element model.

Laser shearography, also called speckle pattern shearing interferometry, is an optical experimental method used to measure the deformation on tested objects. In vibration analysis, shearography is suitable for identifying regular vibration mode shapes of harmonically excited objects because it allows full field and non-contact measurements.

The experimental setup for shearography measurements of the canvas vibration mode shapes is shown in Fig. 4.8. The canvas specimen is illuminated with a laser light which is expanded with a lens in order to cover the entire surface. The reflected laser passes first through a shearing element, a modified Michelson interferometer in this case, generating two slightly sheared images, thus the name shearography. The interferometric superposition of two slightly sheared images creates a speckle interferogram which is then recorded by a CCD camera. When the canvas is deformed by an acoustic load, there is a phase change between the two interferograms. Digital subtraction between the deformed and reference images yields a visible fringe pattern (shearogram) showing the deformation in the canvas specimen [93]. The fringe lines in the pattern are areas along which speckles are nullified [94].
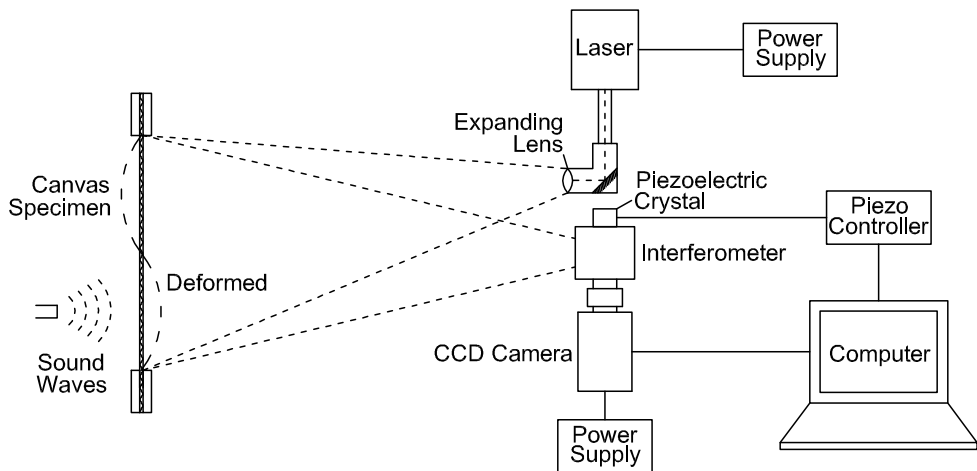
Figure 4.8: Experimental setup of laser shearography for the measurement of canvas mode shapes.

A detailed diagram of the Michelson interferometer is shown in Fig. 4.9. The incident laser is divided into two beams in the beam splitter. A part of the beam goes straight into mirror 1 and the other to mirror 2. The reflected beams from both mirrors recombine after the beam splitter producing shear interference [95]. The CCD camera records the speckle pattern of the vibrating canvas continuously. The digital subtraction is performed between the current

image and the immediately previous image rather than from a reference image at a stationary state. This yields a fringe pattern that changes in quasi real time [96].
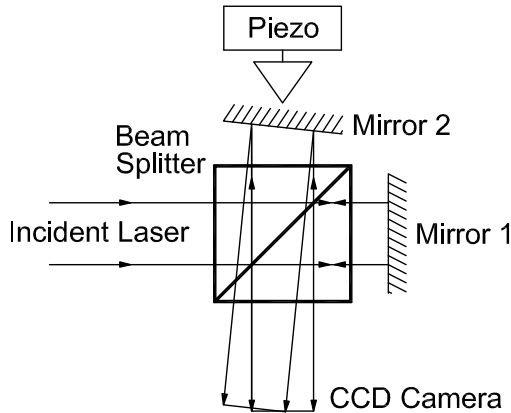
Figure 4.9: Diagram of a modified Michelson interferometer as a shearing and phase-shifting device.

In order to make the fringe patterns visible, a phase-shifting technique is used between two immediate successive images. The phase shift between each image is introduced by driving mirror 2 of the Michelson interferometer with a piezoelectric transducer which is controlled by computer. Without the phase shift introduced by the movement in mirror 2, the intensity of the speckle pattern will be the same as the previous one and there will be no fringe pattern visible.

Before shearography measurements were made, frequency sweeps were performed and single point measurements on the canvas were made with the laser vibrometer as described previously in this section. The natural frequencies were identified at peak amplitudes in the frequency response plots. Then, the specimens were excited at these particular frequencies to perform the shearography measurements and identify the corresponding mode shapes.

The laser source used for shearography measurements was a Torus single-frequency 532 nm continuous wave laser with a power range of 40 to 400 mW, manufactured by Laser Quantum, Stockport, England. A power supply model MPC 3000 manufactured by the same company was used for the laser. A piezo transducer model PSH4z manufactured by Piezosystem Jena, Jena, Germany, was used to drive mirror 2 in the interferometer. The transducer was controller by a piezo controller model NV 40/3 manufactured by the same company. The CCD camera model piA2400-12gm manufactured by Basler in

Ahrensburg, Germany, had a sensor resolution of 2456 x 2058 pixels. A DC power supply for the camera model E 015-2 was used, manufactured by Delta Elektronika, Zierikzee, Netherlands. All optical lenses, mirrors and mounts were manufactured by Linos, Ilmenau, Germany. Finally, all the processing was done in a computer Intel Core 2 quad CPU Q6600 with a processor speed of 2.40GHz and 3.23GB of RAM.

Sampling Frequency

A sampling frequency (f_s) of 500 Hz was chosen for the vibration measurements. This value was chosen as a compromise between a good representation of the waveform and the amount of data generated. It is important to use a sampling frequency that is sufficiently high to capture the details of the analog signal. If the sample rate is too low, an error known as aliasing will occur, which causes the high frequencies to appear as low frequencies. To avoid this, the Nyquist theorem states that there must be at least two sample measurements for each cycle of the highest frequency of interest, this is equivalent to having a sampling frequency of at least twice that frequency (also called the Nyquist frequency) [92]. Given that the maximum frequency of interest for this investigation is 150 Hz. Then the minimum sampling frequency should be 300 Hz.

Sets of Tests

Two sets of tests were conducted. In the first set Rijn and Waal linens with no ground, with ground and with cracked ground were tested for square (40 x 40 cm) specimens under stretching loads of 5, 10 and 20 kg. Several measurements were performed on different positions in the canvas in order to map the surface and identify the mode shapes. In the second set of tests Rijn, Waal and Amazone linens were tested with cracked ground; and cotton canvas with no ground. The materials were tested for two aspect ratios 4:4 and 4:3, all pre-stretched with 10 kg. Only one measurement point per specimen was performed in this set of tests. The natural frequency peaks were identified from the frequency-response plots and the corresponding mode shapes were measured with laser shearography.

4.6 Post-processing

The data obtained with the laser vibrometer is a digital record of the out-of-plane displacement of the canvas as a function of time. As described at the

beginning of the chapter, one needs to have the displacement of the canvas as a function of frequency in order to identify the peak responses and consequently the corresponding natural frequencies. Thus, additional post-processing of the raw data from the vibrometer is necessary to extract the required information for modal analysis.

The vibration of a point in the structure can be represented by a time dependent continuous function $s(t)$. Given that the signal is sampled at regular time intervals, the recorded digital signal of length N can be represented by the discrete vector $\{s(kJ)\}$ for $k = 0, 1, 2, \ldots, N-1$ where k is an integer and $J(= 1/f_s)$ is the sampling interval given by the inverse of the sampling frequency [97]. The signal $\{s(kJ)\}$ can be plotted against the discrete time vector $\{t\} = kJ$ to display it as a function of time. However it is of interest to plot the signal as a function of the driving frequency (frequency-response plots). This can be done recalling that the sweep function (Eq. 4.1) of the excitation frequency is known. Therefore, the signal can be plotted against the discrete driving frequency vector given by $\{f_{dr}(kJ)\} = f_o \, e^{0.01(kJ)}$ for $k = 0, 1, 2, \ldots, N-1$. The signals were post-processed using MATLAB®.

Modal Assurance Criterion

In order to have an indication about the degree of correlation between the predicted FE mode shapes and the measured mode shapes on canvas specimens, the Modal Assurance Criterion (MAC) was applied. This criterion compares the similarities between two mode shape displacement vectors, that is, the experimental mode vector formed by the displacements at the measurement points, and the predicted mode vector formed by the displacements at the corresponding positions in the FE model. This degree of correlation between the vectors is quantified by the MAC number defined as

$$MAC(i,j) = \frac{\left| \{\Phi_i^e\}^T \cdot \{\Phi_j^m\} \right|^2}{(\{\Phi_i^e\}^T \cdot \{\Phi_i^e\})(\{\Phi_j^m\}^T \cdot \{\Phi_j^m\})} \tag{4.2}$$

where $\{\Phi_i^e\}$ is the experimental mode i and $\{\Phi_j^m\}$ is the predicted eigenmode j. The MAC number represents a projection of one vector over the other and it will have values between 0 and 1. A MAC number of 1 means that one vector is a multiple of the other, technically that is to say it has the same shape. Both vectors must have the same number of DOF. The selected measurement locations must therefore correspond to the DOF in the model. For several experimental and numerical mode shapes, the MAC numbers are given in matrix form. High MAC numbers (≈ 1) in the diagonal of the MAC matrix

$(i = j)$ indicate a good match between experimental mode i and numerical mode i. The numbers out of the diagonal $(i \neq j)$ will generally have low MAC numbers (< 0.1) [98, 99].

Damping Extraction

The damping ratio is necessary to simulate the response of the canvas to forced excitation because it determines the energy dissipation in the system, and thus it will have an influence on the vibration amplitudes of the canvas. The damping ratio for the canvas specimens was extracted from the measured response curves by means of the Half-Power Bandwidth (HPBW) method [100, 101]. This method is illustrated with a typical frequency-response curve in the vicinity of resonance as shown in Fig. 4.10. The shape of the curve is determined by the amount of damping in the structure. The method involves determining the frequencies at which the response is reduced to $1/\sqrt{2}$, one frequency below resonance f_1 and one frequency above resonance f_2. The expression for the damping ratio is

$$\zeta = \frac{f_2 - f_1}{f_2 + f_1} \tag{4.3}$$
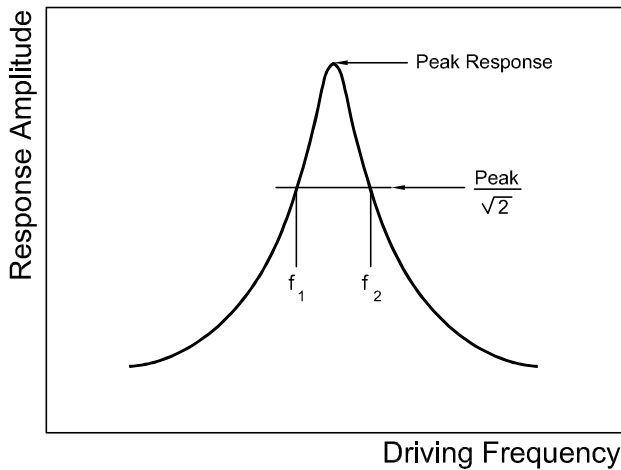
Figure 4.10: Frequency-response plot to determine damping ratio.

It should be noted that this method is used to extract the damping from a frequency-response-function curve which involves the ratio between the response and the excitation. In the present investigation, only measurements of the response were performed and therefore this method is only an approximation to have an estimate of the value for the damping ratio.

Chapter 5

Results

In this section the vibration measurement results are presented together with the results of modeling, in the order of the sets of tests described in Section 4.5 of the experimental description. Typical results obtained from the first set of tests are shown in Fig. 5.1 and Tables 5.1, 5.2 and 5.3. The plots in Fig. 5.1 show the amplitude response (displacement Y axis) as a function of the excitation frequency (X axis) of a single point measured with the laser vibrometer at the center of the second quadrant for 40 x 40 cm Waal linen canvas specimens with no ground, with ground, and with a cracked ground, all under the same stretching load of 5kg. The vertical lines indicate the predicted values of the natural frequencies of the first four modes for comparison.

The excitation source and measurement points were located in opposite quadrants of the specimen as explained in Section 4.5 to trigger and measure the first four modes (1,1)(2,1)(1,2)(2,2). The visualizations shown in Fig 5.2 were obtained with the FE model. These four modes correspond to the first four peaks in the frequency response plots, Fig. 5.1. These are the dominant modes (especially the fundamental mode (1,1)) in the response of the structure, as they are associated with the highest amplitudes.

For the canvas with no ground, Fig. 5.1a, only the fundamental mode (1,1) is clearly present. Mode (1,2) and (2,1) are close together and are not clearly distinguishable due to the high amount of damping present. Note that the scale of Fig. 5.1a (no ground), is a factor of 10 lower than Figs. 5.1b and 5.1c (ground and cracked ground).

When a ground layer is added to the canvas (Fig. 5.1b), there is a decrease of 10 Hz in the fundamental natural frequency as compared to the canvas without ground (Fig. 5.1a). For a canvas with cracked ground (Fig. 5.1c), there is only a slightly difference in frequencies compared to the specimen
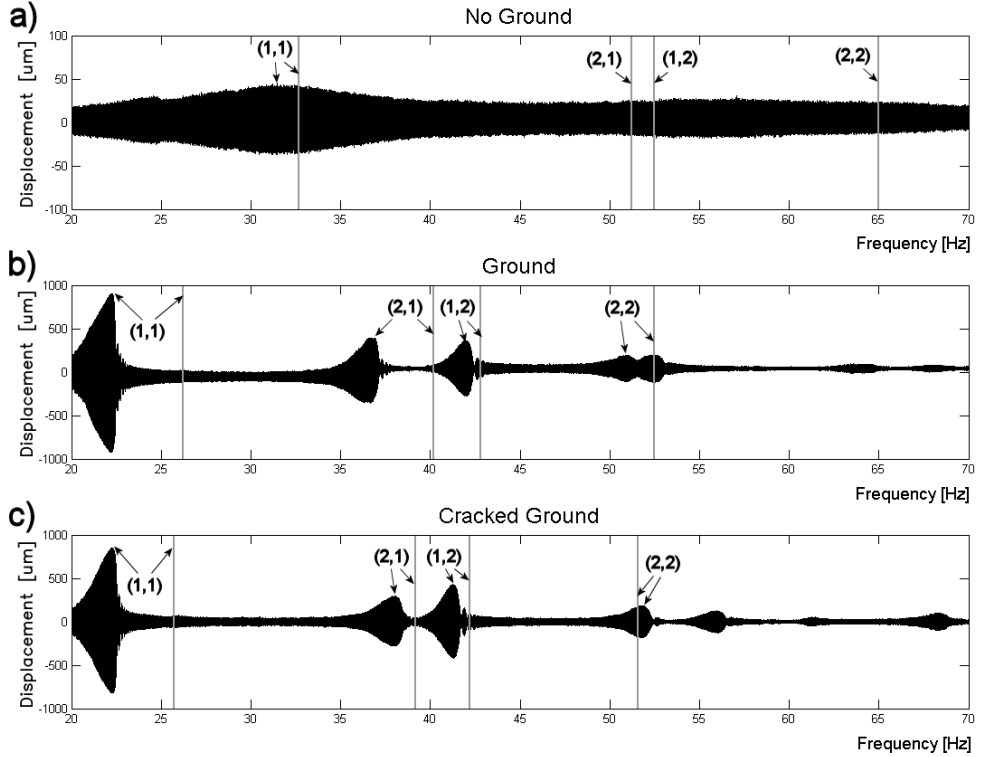
Figure 5.1: Measured frequency-response plots for Waal linen 40 x 40 mm specimens with a stretching load of 5 kg, for canvasses with a) no ground b) ground and c) cracked ground. Note that the scale of the Y axis for no ground (a) is 10 times smaller than for the other two cases. Vertical lines indicate the predicted values for the natural frequencies of the first four modes for comparison. The arrows indicate the mode wave numbers (shown in brackets) which correspond to the experimental natural frequencies and the corresponding predicted frequencies. In the case of a) no ground, the wave numbers for the 2nd, 3rd and 4th frequencies are only indicated for the predicted ones since the corresponding experimental frequencies are not clearly distinguishable.

| Mode (1,1) | Mode (2,1) | Mode (1,2) | Mode (2,2) |
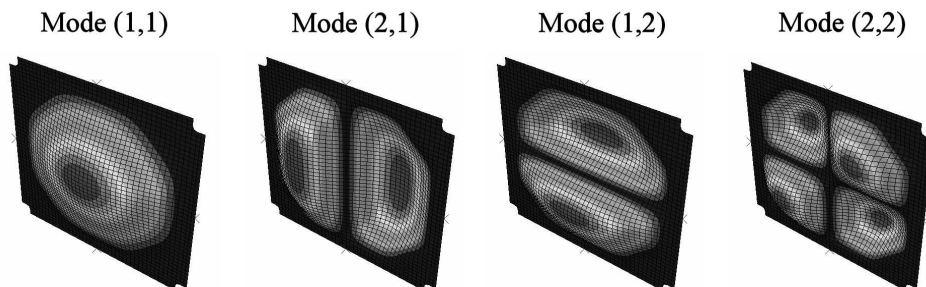
Figure 5.2: First four modes obtained with the FE model.

with a continuous ground layer (Fig. 5.1b).

Tables 5.1, 5.2 and 5.3 show the values for the natural frequencies determined experimentally (Fig. 5.1) and predicted by finite element (FE) modeling together with the percentage difference between them. There is a very small difference between the measured and predicted frequencies (1.5%) for the first mode for a canvas with no ground. On the other hand, for ground and cracked ground the difference for mode (1,1) is significant ($\approx$15%). For higher modes 2, 3 and 4 the difference is again small (1%), except for the second mode for canvas with ground (9%).

Table 5.1: Frequencies Waal no ground 40x40, stretching load 5 kg.

Mode number	Model (m , n)	f [Hz]	Experiment (m , n)	f [Hz]	Difference [%]	Damping [%]
1	(1 , 1)	32.7	(1 , 1)	32.2	1.5	15
2	(2 , 1)	51.2	(2 , 1)	—	—	—
3	(1 , 2)	52.5	(1 , 2)	—	—	—
4	(2 , 2)	65.0	(2 , 2)	—	—	—

Table 5.2: Frequencies Waal ground 40x40, stretching load 5 kg.

Mode number	Model (m , n)	f [Hz]	Experiment (m , n)	f [Hz]	Difference [%]	Damping [%]
1	(1 , 1)	26.2	(1 , 1)	22.5	16.7	2.2
2	(2 , 1)	40.2	(2 , 1)	36.9	9.0	1.3
3	(1 , 2)	42.8	(1 , 2)	42.2	1.5	1.0
4	(2 , 2)	52.5	(2 , 2)	52.6	-0.1	1.4

Table 5.3: Frequencies Waal cracked ground 40x40, stretching load 5 kg.

Mode number	Model (m , n)	f [Hz]	Experiment (m , n)	f [Hz]	Difference [%]	Damping [%]
1	(1 , 1)	25.7	(1 , 1)	22.5	14.4	2.2
2	(2 , 1)	39.2	(2 , 1)	38.8	0.9	1.5
3	(1 , 2)	42.2	(1 , 2)	41.6	1.5	1.0
4	(2 , 2)	51.6	(2 , 2)	51.9	-0.5	1.0

The tables also present the corresponding experimental damping values for each mode determined with the HPBW method as explained in Section 4.6. According to Fig. 5.1a, the canvas with no ground presents very broad peaks due to the high damping involved (15%). In contrast, the canvasses with ground and cracked ground have a relatively low damping ($\approx$1.5%) and display clear sharp peaks.

In order to compare the mode shapes predicted by the model (Fig. 5.2) with the corresponding measured mode shapes, the MAC (Modal Assurance Criterion) numbers were calculated for the first four modes as described in Section 4.6. The MAC matrices are plotted for Waal linen with no ground in Fig. 5.3a, with ground in Fig. 5.3b and with cracked ground in Fig. 5.3c. There are high MAC values (0.9) for the fundamental mode, and a slight decrease in MAC values for higher modes. The MAC matrix for no ground shows only a column for the first mode since higher modes were not identified for the measurements do to the noise in the signal. High MAC numbers in the diagonal thus show a good correlation between the measured and predicted mode shapes.
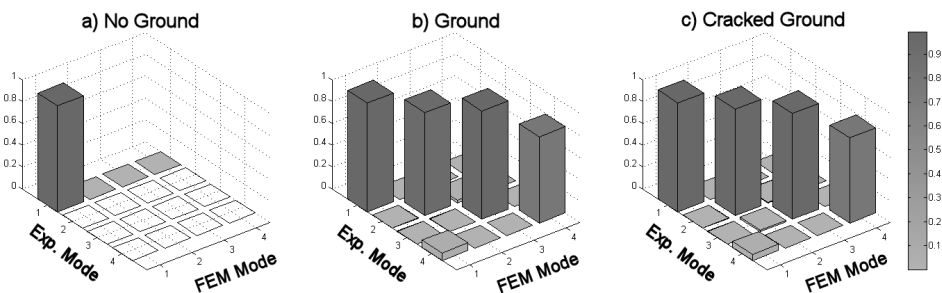
Figure 5.3: MAC matrices for Waal linen with a) no ground, b) ground and c) cracked ground. The MAC matrix for no ground shows only a column for the first mode since this was the only one identified experimentally.

An example of the comparison of the experimental response of the canvas excited over a frequency range, with the predicted forced response calculated with the FE model is shown in Fig. 5.4, for Waal linen with cracked ground (also shown in Fig. 5.1c). The form of predicted dynamic response is similar to that of the measured response for the first four modes. However, significant differences between the predicted and measured natural frequencies can be seen, especially for mode (1,1) and mode (1,2).
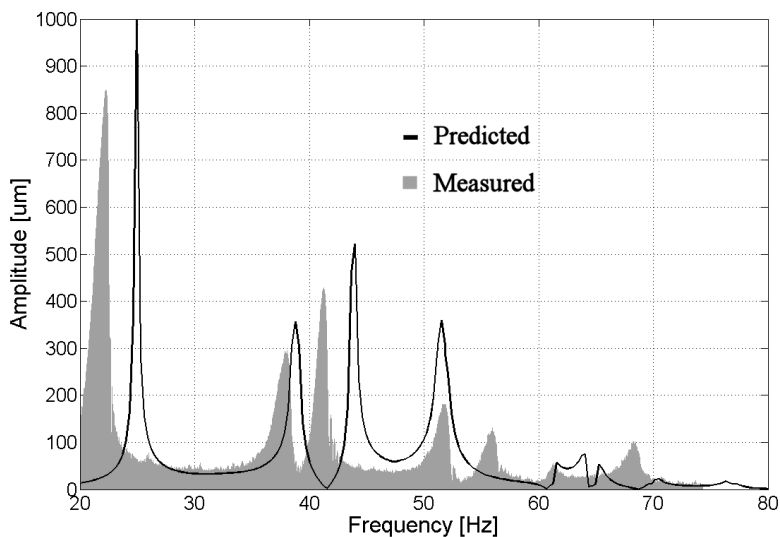
Figure 5.4: Predicted and measured frequency-response plots for Waal linen with cracked ground.

An alternative way to present all of the measured and predicted natural frequencies for all layer configurations and stretching loads is presented in Fig. 5.5 for Rijn linen. The frequencies of the first four modes are shown in separate graphs. The natural frequencies are plotted as a function of the three stretching loads tested (5, 10, 20 kg). Solid lines represent experimental frequency values while dashed lines show the predicted natural frequencies. In general, there is a better agreement between measured and predicted frequencies at low stretching loads. It can be observed that as the stretching load increases, the natural frequencies also increase but not in a linear way. This behavior can be recalled from the natural frequency expression Eq. A.27 obtained in the analytical model where the natural frequency is proportional to the square root of the stretching load.

Typical results obtained from the second set of tests are shown in Fig. 5.6 for Amazone linen with cracked ground for 40 x 40 cm and 40 x 30 cm
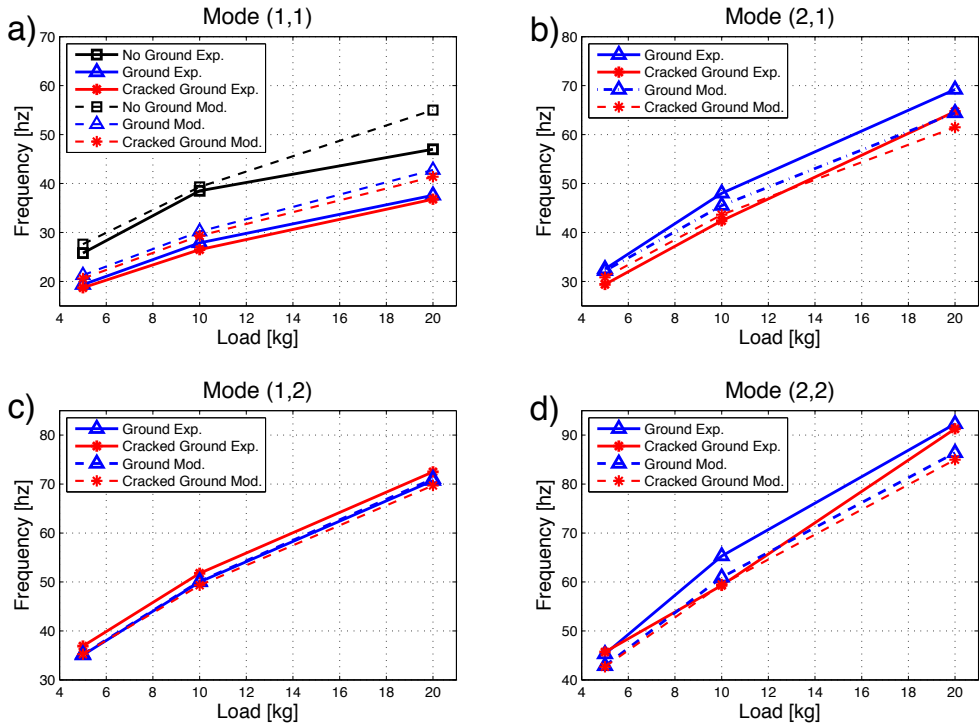
Figure 5.5: Predicted and experimental natural frequencies as a function of stretching loads for Rijn linen with no ground, with ground and with cracked ground for a) Mode (1,1), b) Mode (2,1), c) Mode (1,2) and d) Mode (2,2).

specimens under a stretching load of 10kg. Again, the frequency-response plots show the displacement of a single point measured with the laser vibrometer at the center of the second quadrant of the canvas specimen. A summary of the predicted and measured natural frequencies for the 40x30 specimen are shown on Table 5.4 for illustration. There is good agreement for the fundamental frequency and for mode (2,1). However, the other modes show higher discrepancies. Mode (1,2) in particular, appears to be experimentally in a different mode order (after mode (2,2)) than the predicted order. For the 40x30 specimen, there is fairly good agreement for the fundamental frequency, but the discrepancies for higher modes are rather large.
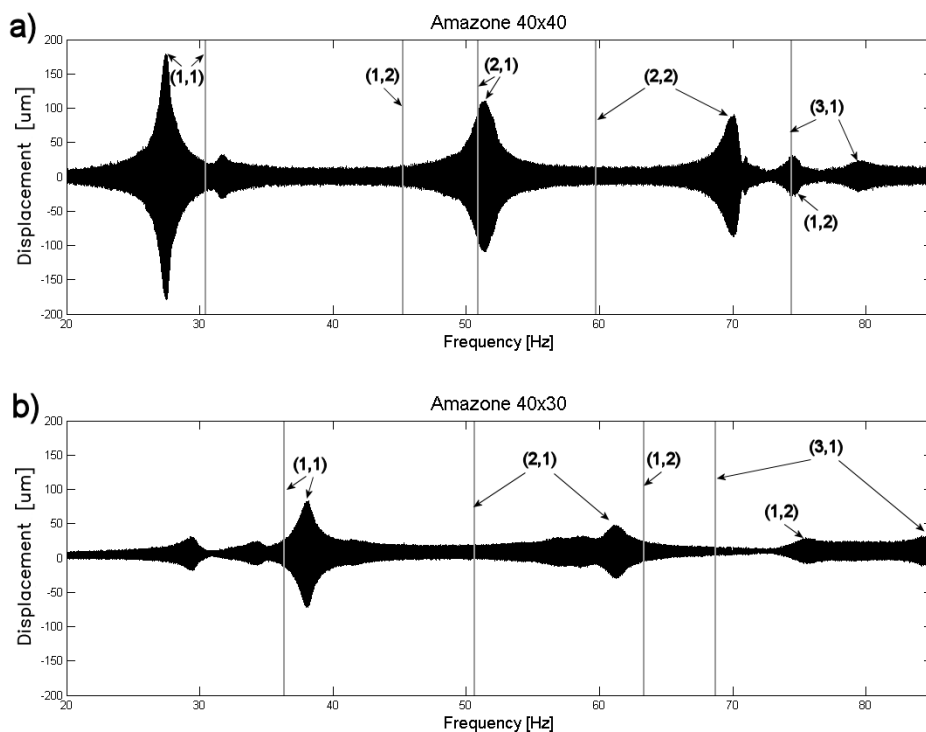
Figure 5.6: Frequency - response plots for Amazone linen with cracked ground for a) 40 x 40 cm and b) 40 x 30 cm specimens with a stretching load of 10 kg

A comparison between the predicted and measured mode shapes is presented in Figs. 5.7 and 5.8. The predicted displacement mode shapes from the FE model are shown on the left hand side (a, b, c), while the mode shapes measured with laser shearography are shown on the right hand side (g, h, i). However, the measured mode shapes (shearograms) show the deformation (displacement derivative) of the canvas specimen. This makes the comparison of

Table 5.4: Frequencies Amazone linen cracked ground 40x30, stretching load 10 kg.

Mode number	Model (m , n)	f [Hz]	Experiment (m , n)	f [Hz]	Difference [%]	Damping [%]
1	(1 , 1)	36.4	(1 , 1)	38.0	-4.3	1.4
2	(2 , 1)	50.6	(2 , 1)	61.3	-17.4	1.3
3	(1 , 2)	63.3	(1 , 2)	75.6	-16.2	1.4
4	(3 , 1)	68.7	(3 , 1)	84.6	-18.8	1.8
5	(2 , 2)	70.9	(2 , 2)	91.0	-22.0	0.8

the measured shearograms with the predicted mode shapes visually difficult. In order to assist in this comparison, analytical derivatives of the predicted (a, b, c) displacement mode shapes are given in the middle (d, e, f) of Figs. 5.7 and 5.8. These derivatives can be directly compared with the measured displacement derivatives on the right (g, h, i).

The shearograms, Figs. 5.7 and 5.8 (g, h, i), show the derivative of the displacement of the mode shape with respect to the x direction ($\partial w/\partial x$), except for Figs. 5.7 i which shows the derivative of the displacement with respect to the y direction ($\partial w/\partial y$) in order to observe the wave number in this direction. The darker areas in the figures represent antinodal positions or areas were the displacement derivative (slope) is zero. Thus, at the peaks or valleys of the mode shape where a tangent has a horizontal position (zero slope), a darker region is observed in the displacement derivatives. These positions should not be confused with nodal lines on the displacement shape itself. An example of nodal and antinodal positions is shown in Fig. 5.7 h.

Note the similarity between the shearograms (g, h, i) and the analytical displacement derivatives (d, e, f). This indicates that the overall shape of the predicted modes agrees with the measured ones with the same number of half waves in each direction. Therefore, for mode (1, 1) with a single half wave, the derivative of the displacement with respect to the x direction has a vertical line in the middle with zero slope. For mode (2, 1) with two half waves in the x direction, the derivative of the displacement with respect to the x direction ($\partial w/\partial x$) has two vertical lines of zero slope at the peaks and valleys (antinodal positions) of the mode shape. For mode (1, 2) with two half waves in the y direction, the derivative of the displacement with respect to y ($\partial w/\partial y$) has two horizontal lines of zero slope at the peaks and valleys of the mode shape, and so on for the rest of the mode shapes. A description of the analytical derivation of the mode shapes is given in Appendix G.
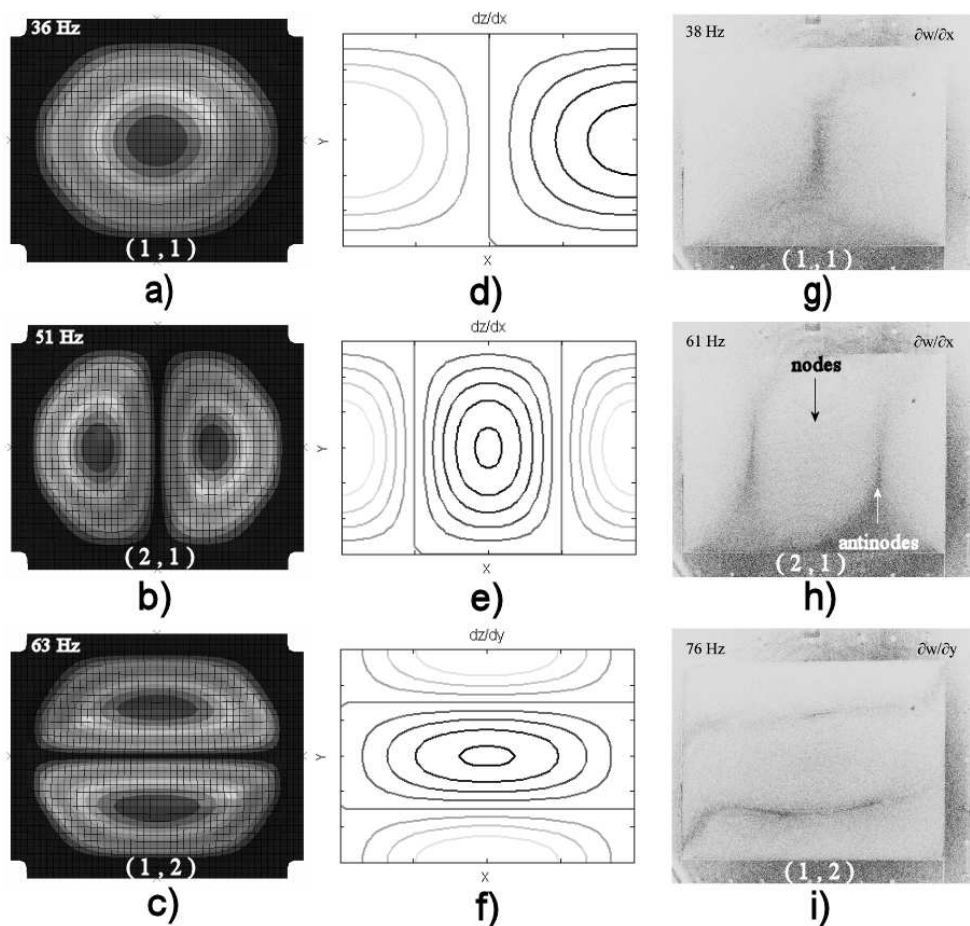
Figure 5.7: Mode shapes (1,1), (2,1), (1,2), predicted by FE model (left, a, b, c) and measured mode shapes with laser shearography (right, g, h, i) for Amazone linen with cracked ground 40 x 30 cm. Shearography mode shape measurements g) (1,1) and h) (2,1) show displacement derivatives with respect to the x direction, while mode i) (1,2) shows the displacement derivative with respect to the y direction. The analytical mode shape derivatives (middle d, e ,f) are given to allow for a direct comparison between the predicted mode shapes (a, b, c) and the measured mode displacement derivatives (g, h, i).
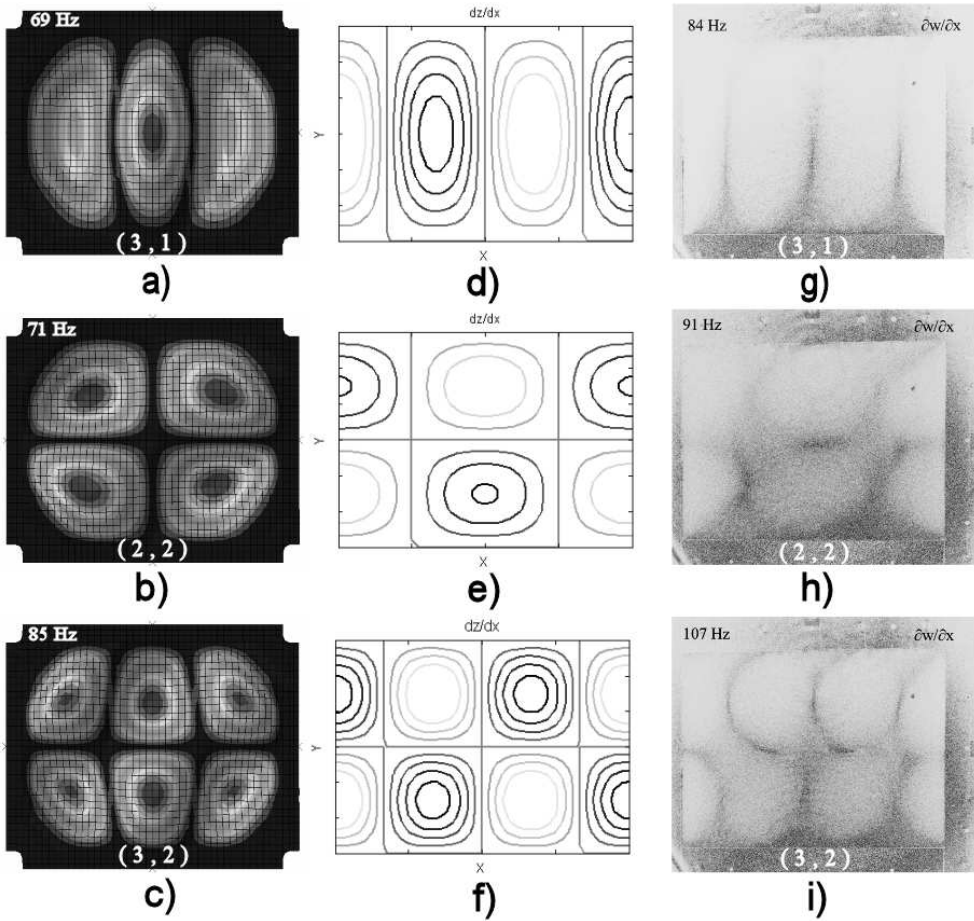
Figure 5.8: Mode shapes (3,1), (2,2), (3,2), predicted by FE model (left, a, b, c) and measured mode shapes with laser shearography (right, g, h, i) for Amazone linen with cracked ground 40 x 30 cm. Shearography mode shape measurements g)(3,1), h)(2,2) and i)(3,2) show displacement derivatives with respect to the x direction. The analytical mode shape derivatives (middle d, e ,f) are given to allow for a direct comparison between the predicted mode shapes (a, b, c) and the measured mode displacement derivatives (g, h, i).

Chapter 6

Discussion

A finite element model has been developed in order to characterize the vibration behavior of sensitive canvas paintings. Vibration experiments were carried out to measure the natural frequencies and corresponding mode shapes of canvas specimens in order to verify the accuracy of the model. The results obtained show that a canvas painting can be modeled as an orthotropic thin laminated plate with biaxial tension. The modeled cases and experiments showed similar vibration behavior with regular modes formed by a number of half-waves for both in-plane coordinates of the canvas, similar to the behavior observed in orthotropic thin plate theory.

The model and experimental results show a number of general effects of each layer on the global behavior of the system. Adding paint layers to a canvas support represent both additional mass (weight) and additional bending stiffness (rigidity). Recall from the analytical model (Eq. 3.1) that the natural frequencies are directly proportional to the square root of the bending stiffness and inversely proportional to the square root of the mass. The results show that the natural frequencies of a canvas with ground are significantly lower than the canvas with no ground for the same stretching load value. This means that the additional mass is the dominant factor which causes the frequency values to drop. The paint layers are very thin so the contribution of the bending stiffness to the natural frequency is very small compared to the additional mass. This negligible bending stiffness effect is also observed in results for canvasses with cracked ground in which the natural frequencies are very similar when compared to the frequency values of canvasses with a ground especially for the first mode. The effect of the paint layers was also verified in the FE model by dropping the mass of the paint to (nearly) zero and observing that the frequency was practically the same as the canvas on its own.

The results show that the natural frequencies are strongly dependent on the tension present in the canvas painting with membrane behavior prevailing over plate behavior. Loads of 5, 10 and 20 Kg (on 0.4 m specimen edge) were tested. However, the vibration measurements for 20 kg loads in most tests had a low signal to noise ratio and the natural frequencies were not clearly identifiable. Additionally, the discrepancies with the predicted frequencies were high as a consequence of the non-linear material behavior of textiles at higher loads. This nonlinear behavior is not taken into account in the model since it is assumed to be linear elastic.

The vibration of the canvas with no ground presents a large amount of damping because the yarns in the textile can move with respect to each other. This involves a high amount of friction that dissipates the energy of the system. Additionally the surrounding air is free to move through the gaps of the textile damping out the vibrations. This explains why the damping is much lower for cotton than for linen, because cotton has a much tighter weave without any gaps. In canvas with ground, on the other hand, the yarns are "frozen" by the paint layers and no relative movement (friction) between the yarns is possible. In this case the low damping value would be produced mainly by the energy dissipated through friction with the surrounding air and the energy absorbed through the clamps. For a canvas with cracked ground, the damping increases slightly compared to the one with ground because the energy is dissipated throughout the paint cracks. At high stretching loads, the damping is high and there are low canvas vibration amplitudes. This results from the higher restoring force about the equilibrium position due to the higher tension. Measurements performed on canvas with no ground for high stretching loads of 20 kg did not show distinguishable peak amplitudes (natural frequencies) because of the high damping values and low vibration amplitudes. The signal is thus lost in the measurement noise.

However, a comparison between the predicted mode shapes and the corresponding measured ones showed differences in the natural frequency values. Typically, for non-critical applications the relative error between the predicted and measured eigenfrequencies should be within 5% in order to be considered as good agreement between model and experiments. The results in this investigation show that for canvasses with no ground, there is good agreement in the natural frequencies for the first mode (1,1). However, for canvasses with ground or cracked ground the differences were greater than 5%. The natural frequencies for mode (1,1) are overpredicted for all cases. The differences range from 6-8% for 5 kg stretching load except for Waal linen with no ground and cracked ground with differences of only 1.46% and 0.68% respectively. Higher stretching loads caused the differences to increase up to 10% for 10 kg and 20% for 20 kg. The differences for mode (2,1) are over or under predicted depending

on the modeled case ranging from 3% to -10%. For modes (1,2) and (2,2) the frequencies for all modeled cases are underpredicted with differences ranging from 0 to -10%. In general there is better agreement between predicted and experimental frequencies for low stretching loads (5 or 10 kg) than for high stretching loads (20 kg), where the non-linear material behavior of the textile takes place causing an increase in the discrepancies. This behavior can be recalled from the frequency vs. load plots (Fig. 5.5) in the Results Section.

An optimization of the model was required in order to obtain better agreement between the predicted and measured frequencies for modeled cases with differences above 5%. The optimization of the model was performed by manually changing the modeling parameters so as to have better agreement between the predicted and measured frequencies. For this manual fitting procedure, a sensitivity analysis was performed in order to determine how sensitive the natural frequencies are to changes in a specific parameter. The parameters can then be optimized based on this analysis, in order to obtain an improved representation of the real system.

6.1 Sensitivity Analysis

For the sensitivity analysis, the derivatives of the frequencies with respect to the model parameters are calculated using Eq. B.14 from the FE model. The Abaqus software was used for the automatic differentiation.

Table 6.1 shows a summary of the average sensitivity values for each of the model parameters. The values are an average of the sensitivities for all modeled cases in order to provide an overview of the effect of the model parameters on the natural frequencies. However, it should be noted that the actual optimization procedure was performed with the specific sensitivity values for each modeled case. The sensitivity values represent the percentage change of the natural frequencies for the first four modes produced by a 10 % change in the corresponding model parameter. If an increase in the parameter produces an increase in frequencies or if a decrease in the parameter produces a decrease in frequencies, the relation is said to be direct and the sensitivity values are positive. On the other hand, if an increase in the parameter produces a decrease in frequencies or if a decrease in the parameter produces an increase in frequencies, the relation is said to be inverse and the sensitivity values are negative. The order in which the parameters are presented in Table 6.1 corresponds to the properties of the canvas, the properties of the ground, and the stretching loads. The sensitivity values for each parameter are analyzed below in further detail.

Table 6.1: Average sensitivity values for model parameters

	10 % Change in Parameter:	Change in Natural Frequencies for Modes:			
		(1:1)	(2:1)	(1:2)	(2:2)
Canvas	h_m *	(-) 0.05 %	(-) 0.14 %	(-) 0.06 %	(-) 0.05 %
	E_1	-0.37 %	-0.52 %	-0.25 %	-0.42 %
	E_2	1.84 %	2.33 %	1.34 %	1.67 %
	ν_{12}	-0.27 %	-0.43 %	-0.07 %	-0.13 %
	G_{12}	-1.50 %	-1.83 %	-1.13 %	-1.29 %
	G_{13}, G_{23}	0.0015 %	0.0029 %	0.0005 %	0.0013 %
	$\overline{m}$ †	-2.34 %	-2.34 %	-2.34 %	-2.34 %
Ground	h_g	0.03 %	0.03 %	0.02 %	0.03 %
	E_g	0.02 %	0.03 %	0.02 %	0.03 %
	$\overline{m}$ ‡	-7.20 %	-7.40 %	-7.00 %	-7.10 %
Loads	F_x	4.09 %	7.18 %	1.29 %	3.89 %
	F_y	0.71 %	-2.35 %	3.43 %	0.84 %

* Inverse relation for models with ground layer (minus sign in brackets)
† Mass sensitivity values for canvas with no ground
‡ Mass sensitivity values for canvas with ground
Sub-indices $_1$ and $_2$ correspond to material directions weft and warp respectively
Sub-indices $_x$ and $_y$ correspond to global plate coordinates

Canvas

Table 6.1 shows that the natural frequencies are not significantly altered by a change in the thickness (h_m) of the canvas as can be seen from the low sensitivity values. The reason for the low sensitivity is that the assumed thickness values for the model are small since they were only a fraction of the nominal thickness of the textile, see Section 3.2. Therefore, changes in the thickness in the same order of magnitude of the thickness itself cause small changes on the bending stiffness and thus small changes on the frequencies. Note that the thickness sensitivity values for models with no ground and cracked ground have a direct relation (positive sign), while for models with ground the relation is inverse (negative sign in brackets). The reason is that in a laminate (canvas and ground), increasing the thickness of the canvas that has a lower bending stiffness compared to the paint will reduce the overall bending stiffness of the laminate causing a decrease in frequencies.

The sensitivity values for the E modulus of the canvas in the weft direction (E_1) have an inverse relation (negative sign). Thus, an increase in modulus would cause a decrease in frequencies. This would not be something to expect

since recalling Eq. A.27 for the vibration of an orthotropic plate, the frequencies should increase with an increase in stiffness. However, it should be noted from the derivation of this analytical equation that the coupling terms are neglected in order to obtain an exact solution. The effect that the bending and stretching coupling has is to lower the natural frequencies and this can cause the sensitivity values to be negative. For the E modulus in the warp direction (E_2), the relation is direct with higher sensitivity values compared to the weft due to its considerably lower stiffness. Thus an increase in the warp modulus will cause a greater increase in frequencies. The E moduli sensitivities in the weft and warp for no ground, ground and cracked ground have similar values for all modeled cases.

An increase in the Poisson's ratio (decrease in absolute value since it is negative) causes a decrease in the frequencies for all modes. It should be noted however, that a change in Poisson's ratio does not have the same influence for all four modes as can be seen from the different sensitivity values given on Table 6.1. This is related to the number of half waves in each mode that can be affected by the Poisson effect due to the biaxial tensile loading. It should be noted that the Poisson's ratio has a very non-linear behavior as a function of strain (recall Fig. 3.17). In addition, the variation of frequencies with respect to the variation in Poisson's ratio was observed to be non-linear, thus the sensitivity values are representative only in the immediate vicinity of the assumed value.

Table 6.1 shows that there is an inverse relationship for the sensitivities of the shear modulus G_{12}, that is, an increase in shear modulus causes the natural frequencies for all modes to decrease. The effect that the shear modulus has on the vibration behavior of the canvas is due to the stress concentrations in the corners caused by shear loading. This causes zones with different stress distribution which affect the overall vibration behavior of the structure. These zones with different stress fields behave differently from the rest of the structure. They can have their "own" vibration modes and frequencies, and they are susceptible to buckling under shear loading due to the thinness of the structure. Shear loading in the canvas can also be a consequence of the non-uniform biaxial tension applied in reality.

Note from the sensitivity values for the shear moduli in the transverse direction G_{23} and G_{13}, that their effect in the natural frequencies is negligible. Since the canvas is a thin plate, the transverse shear stresses in the plate are small compared to the longitudinal stresses. Thus, changes in the transverse shear moduli have a very low influence in the natural frequencies of the canvas.

The sensitivity values for the mass $(\overline{m})$ are the highest among the parameters of the canvas textile as can be seen from the first section of Table 6.1.

There is an inverse relation (minus sign) with equivalent sensitivity values for all modes. Thus, an increase in mass would cause the frequencies to decrease with the same percentage for all modes.

Ground

The contribution of the ground layers to the bending stiffness of the canvas is low due to the small thickness values of the films (max 0.1 mm). The low stiffness contribution of the ground layers is evidenced in the low sensitivity values of the frequencies with respect to the elastic modulus and thickness of the paint (see E_g and h_g in Table 6.1). Sensitivity values for the E modulus and thickness of the ground have similar values and a direct relation for all modes.

It should be noted that the effect of the stiffness of the paint layers on the natural frequencies of the painting depends on its actual value with respect to the stiffness of the weft and warp directions of the canvas. This is because in Classical Laminate Theory, the stiffness of the laminate is obtained by the sum of the stiffnesses of each layer multiplied by their thickness fraction (similar to rule of mixtures with volume fraction). Therefore, for fresh paint films that have very low stiffness values which can be below the textile's warp E modulus, the overall stiffness of the laminate will decrease, causing a decrease in all eigenfrequencies. On the other hand, aged paint films become brittle and can have a higher E modulus than the textile's weft modulus. In this case, the overall stiffness of the laminate increases causing an increase in the eigenfrequencies. If the stiffness of the paint layers lies between the weft and the warp stiffness, it will have an effect on the orthotropy of the laminate. It will increase the frequencies for mode shapes with more half waves in the warp direction (e.g. (1,2) (1,3) etc.) because it will effectively increase the stiffness in this direction. On the other hand, the frequencies for mode shapes with more half waves in the weft direction (e.g. (2,1) (3,1) etc.) will decrease as the stiffness in this direction is reduced.

The highest values in Table 6.1 correspond to the sensitivities of mass of the canvas with ground. There is an inverse relation with values around -7.20% for all modes. Note from Table 6.1, that the higher the value of the mass, the higher the sensitivity, as can be seen from the sensitivity values of the canvas with ground (-7.20%) which are higher than the values for a canvas with no ground (-2.34%). It should be noted also that the sensitivity values for a canvas with cracked ground (not shown in the table) are practically the same as the values for canvas with ground since the mass is the same.

Loads

The sensitivity values with respect to the tensile loads are shown in the last part of Table 6.1. A change in tension in the weft direction (F_x) has a direct relation (positive) with a different effect for each mode. It was observed that a change in tension for the weft has a higher influence on the frequencies of symmetric modes such as (1,1), (2,2), etc; when compared to the warp. This is caused by the higher stiffness in the weft direction. Additionally, changes in F_x also have a higher influence in the frequencies of mode shapes with more half waves in the weft direction (modes (2,1), (3,1), etc). In contrast, a change in tension in the warp direction (F_y) has a lower influence in the frequencies of symmetric modes, due to the lower stiffness in the warp. Accordingly, a change in tension in the warp direction has a greater effect in the frequencies of modes with more half waves in the warp direction such as modes (1,2), (1,3), etc. Note however that for mode (2,1) the sensitivity with respect to the tension in the warp direction is negative. This might be caused by the direction of the force being applied in the direction of the mode nodal lines.

6.2 Model Optimization

The attention for the optimization of the model was focused mainly in obtaining a good agreement for the first mode (1,1), and the best agreement possible for the second and third modes (2,1) and (1,2). These are the most important modes in the dynamics of the structure as they are associated with the highest amplitudes at resonance. The three parameters that were selected from Table 6.1 for optimization of the first three modes were the shear modulus G_{12} and the stretching forces F_x and F_y. The procedure followed to select these parameters was first to consider the ones with the highest sensitivity values (G_{12}, F_x, F_y, E_2, $\overline{m}$) since these will have a greater influence in the natural frequencies. From these parameters, only those with a logical criterion for the optimization of the model were selected. The shear modulus was selected because, as discussed previously, it has a high influence on the natural frequencies of the canvas, evidenced from its sensitivity values (Table 6.1). Given that the assumed value was not directly verified experimentally, but only estimated through a model, there could be room for improvement in the assumptions made for the shear modulus. The stretching forces were selected due to their high influence on natural frequencies (see Table 6.1), and because they are parameters that may vary experimentally due to the textile relaxation and non-uniform clamping. Additionally they can affect each vibration mode in a different way for the model optimization.

The bending stiffness values resulting from the assumed thickness (h_m), E moduli (E_1 and E_2) and Poisson's ratio (ν_{12}) were shown to be in agreement with the measured bending stiffnesses (see section 3.2). Thus, these parameters were not optimized even though E_2 has high sensitivity values. The sensitivity values for h_m, E_1 and ν_{12} are low and would not cause a significant difference in the natural frequencies. The mass $\overline{m}$ was not selected for the optimization since it has a fixed value provided by the canvas manufacturer.

The selected parameters (G_{12}, F_x and F_y) and the way they influence the first four natural frequencies are shown schematically in Fig. 6.1 for Waal linen with ground. The vertical lines show the predicted frequencies and the gray arrows indicate the direction in which the predicted natural frequencies must be shifted for the model optimization. The black arrows on the top of the figure show the shift in the natural frequencies produced by a change in the corresponding parameter.
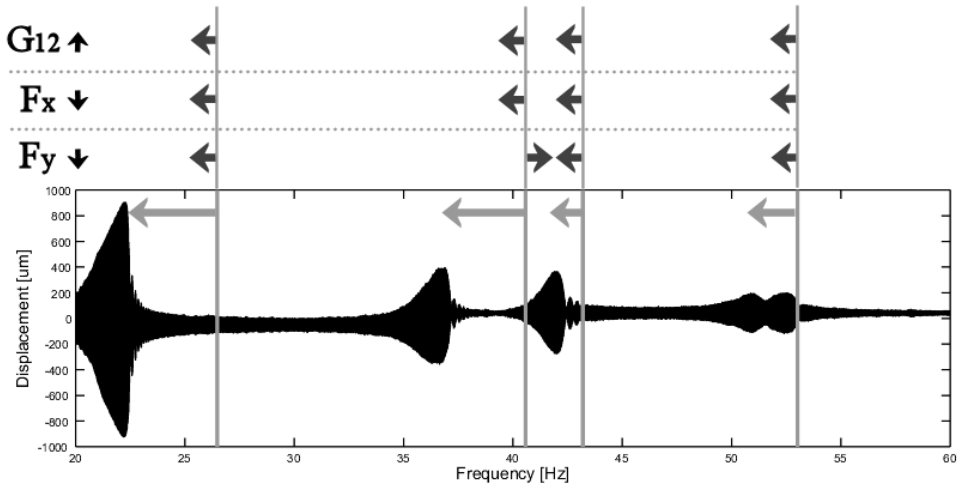
Figure 6.1: Influence of selected parameters for model optimization on natural frequencies of Waal linen with ground

The procedure that was followed was first to increase the shear modulus in order to obtain good agreement for the first mode. Then the tension values for the weft and warp directions were adjusted to provide good agreement for modes (2,1) and (1,2). The changes in the model parameters were performed based on the sensitivity values in order to approximate to the experimental values.

Table 6.2: Optimized frequencies for Rijn linen with no ground, 40x40 cm, stretching load 5 kg

Mode Number	Wave # (m , n)	Model f [Hz]	Exp f [Hz]	Optimized Difference	Initial Difference
1	(1 , 1)	25.2	25.8	-2.3 %	7 %
	Parameter	G_{12} [MPa]	F_x [N]	F_y [N]	
	Optimized	500	49	49	
	Initial	271	49	49	

Table 6.3: Optimized frequencies for Rijn linen with ground, 40x40 cm, stretching load 5 kg

Mode Number	Wave # (m , n)	Model f [Hz]	Exp f [Hz]	Optimized Difference	Initial Difference
1	(1 , 1)	20.1	19.3	3.9 %	10 %
2	(2 , 1)	31.1	32.5	-4.4 %	-1.1 %
3	(1 , 2)	32.6	35.1	-7.0 %	0.4 %
4	(2 , 2)	39.9	45.3	-11.9 %	-5.3 %
	Parameter	G_{12} [MPa]	F_x [N]	F_y [N]	
	Optimized	500	49	49	
	Initial	271	49	49	

Table 6.4: Optimized frequencies for Rijn linen with cracked ground, 40x40 cm, stretching load 5 kg

Mode Number	Wave # (m , n)	Model f [Hz]	Exp f [Hz]	Optimized Difference	Initial Difference
1	(1 , 1)	19.1	18.7	2.0 %	10.0 %
2	(2 , 1)	29.2	29.4	-0.7 %	4.9 %
3	(1 , 2)	31.4	36.9	-14.9 %	-4.5 %
4	(2 , 2)	37.8	45.7	-17.3 %	-6.7 %
	Parameter	G_{12} [MPa]	F_x [N]	F_y [N]	
	Optimized	500	47	49	
	Initial	271	49	49	

The optimization was performed for a representative selection of the modeled cases with relevant materials, geometries and stretching loads. Due to the applicability of the model to linear materials at low stretching loads and

Table 6.5: Optimized frequencies for Waal linen with no ground, 40x40 cm, stretching load 5 kg

Mode Number	Wave # (m , n)	Model f [Hz]	Exp f [Hz]	Optimized Difference	Initial Difference
1	(1 , 1)	31.9	32.2	-0.9 %	1.5 %
	Parameter	G_{12} [MPa]	F_x [N]	F_y [N]	
	Optimized	500	49	49	
	Initial	366	49	49	

Table 6.6: Optimized frequencies for Waal linen with ground, 40x40 cm, stretching load 5 kg

Mode Number	Wave # (m , n)	Model f [Hz]	Exp f [Hz]	Optimized Difference	Initial Difference
1	(1 , 1)	23.5	22.5	4.5 %	16.7 %
2	(2 , 1)	35.5	36.9	-3.8 %	9.0 %
3	(1 , 2)	38.9	42.2	-7.7 %	1.5 %
4	(2 , 2)	46.6	52.6	-11.4 %	-0.1 %
	Parameter	G_{12} [MPa]	F_x [N]	F_y [N]	
	Optimized	500	39	44	
	Initial	366	49	49	

Table 6.7: Optimized frequencies for Waal linen cracked ground, 40x40 cm, stretching load 5 kg

Mode Number	Wave # (m , n)	Model f [Hz]	Exp f [Hz]	Optimized Difference	Initial Difference
1	(1 , 1)	23.6	22.5	5 %	14.4 %
2	(2 , 1)	37.2	38.8	-4.1 %	0.9 %
3	(1 , 2)	38.0	41.6	-8.7 %	1.5 %
4	(2 , 2)	47.9	51.9	-7.7 %	-0.5 %
	Parameter	G_{12} [MPa]	F_x [N]	F_y [N]	
	Optimized	500	42	42	
	Initial	366	49	49	

the low signal to noise ratio in the test results at high loads, only 5 and 10 kg were considered for model optimization. The optimized values for the first four eigenfrequencies are compared to the corresponding experimental values

Table 6.8: Optimized frequencies for Amazone linen cracked ground, 40x40 cm, stretching load 10 kg

Mode Number	Wave # (m , n)	Model f [Hz]	Exp f [Hz]	Optimized Difference	Initial Difference
1	(1 , 1)	28.8	27.5	4.7 %	10.8 %
2	(2 , 1)	51.7	51.4	0.6 %	-0.9 %
3	(2 , 2)	55.0	70.0	-21.4 %	-14.7 %
4	(1 , 2)	38.0	74.5	-49.0 %	-39.3 %
	Parameter	G_{12} [MPa]	F_x [N]	F_y [N]	
	Optimized	350	84	68	
	Initial	315	98	98	

Table 6.9: Optimized frequencies for Amazone linen cracked ground, 40x30 cm, stretching load 10 kg

Mode Number	Wave # (m , n)	Model f [Hz]	Exp f [Hz]	Optimized Difference	Initial Difference
1	(1 , 1)	39.6	38.0	4.2 %	-4.3 %
2	(2 , 1)	58.3	61.3	-4.9 %	-17.4 %
3	(2 , 2)	66.7	75.6	-11.8 %	-16.2 %
4	(1 , 2)	80.1	84.6	-5.3 %	-18.8 %
	Parameter	G_{12} [MPa]	F_x [N]	F_y [N]	
	Optimized	350	88	115	
	Initial	315	73	98	

Table 6.10: Optimized frequencies for cotton with no ground, 40x40 cm, stretching load 10 kg

Mode Number	Wave # (m , n)	Model f [Hz]	Exp f [Hz]	Optimized Difference	Initial Difference
1	(1 , 1)	36.2	37.6	-3.6 %	2.3 %
2	(2 , 1)	52.0	50.0	4.1 %	22.9 %
3	(1 , 2)	60.9	63.5	-4.1 %	-7.4 %
4	(2 , 2)	68.2	70.4	-3.1 %	3.1 %
	Parameter	G_{12} [MPa]	F_x [N]	F_y [N]	
	Optimized	209	68	108	
	Initial	209	98	98	

in Tables 6.2 through 6.10. The percentage difference between the optimized model and experiments is also compared to the initial difference. The initial and optimized parameter values are shown at the bottom of each table.

Following the optimization procedure described previously, an increase in the shear modulus for all the linens, Rijn, Waal and Amazone, was required in order to obtain good agreement for mode (1,1). The optimized value increase is consistent for materials with no ground, with ground and with cracked ground. For Rijn and Waal linens, there was an increase in the shear modulus to a value of 500 MPa (see Tables 6.2 to 6.7), while for Amazon linen, an increase from 315 to 350 MPa in shear modulus was required (see Tables 6.8 and 6.9). For cotton canvas, a change in the shear modulus was not necessary (see Table 6.10), and the optimization was only performed with the biaxial tension.

Once the frequency for mode (1,1) was optimized with changes in the shear modulus, the tension in the weft and warp directions were adjusted to optimize the frequencies for modes (2,1) and (1,2). A decrease in the tension was required for the optimization of most cases, specifically, for Rijn linen with cracked ground (Table 6.4), for Waal linen with ground and with cracked ground (Tables 6.6 and 6.7), and for Amazone linen with cracked ground (Table 6.8). For Rijn linen with no ground and with ground (Tables 6.2 and 6.3), and for Waal linen with no ground (Table 6.5), a change in biaxial tension was not necessary. On the other hand, for Amazone 40x30 and for cotton (Tables 6.9 and 6.10) good agreement was achieved by increasing the tension slightly.

Tables 6.2 to 6.10 show that the model optimization yielded good agreement (within 5%) for the first two modes (1,1) and (2,1) in all cases. This was achieved generally at the expense of a greater difference for higher modes (1,2) and (2,2). This is shown in Fig. 6.2 for Waal linen with ground as an example, where the frequencies before (a) and after (b) optimization can be compared with the measured resonances.

To summarize, the optimization of mode (1,1) was performed by increasing the values of the shear modulus for all linen canvasses but not for cotton canvas. In the case of the biaxial tension for the optimization of modes (2,1) and (1,2), there is not a consistent tendency in the variation of tension for all cases. For some cases there was an increase or decrease in tension by a different amount for the weft and warp directions, while for other cases the tension remained the same. The reasons for the changes in the optimized parameter values are discussed in the following paragraphs along with their physical significance.
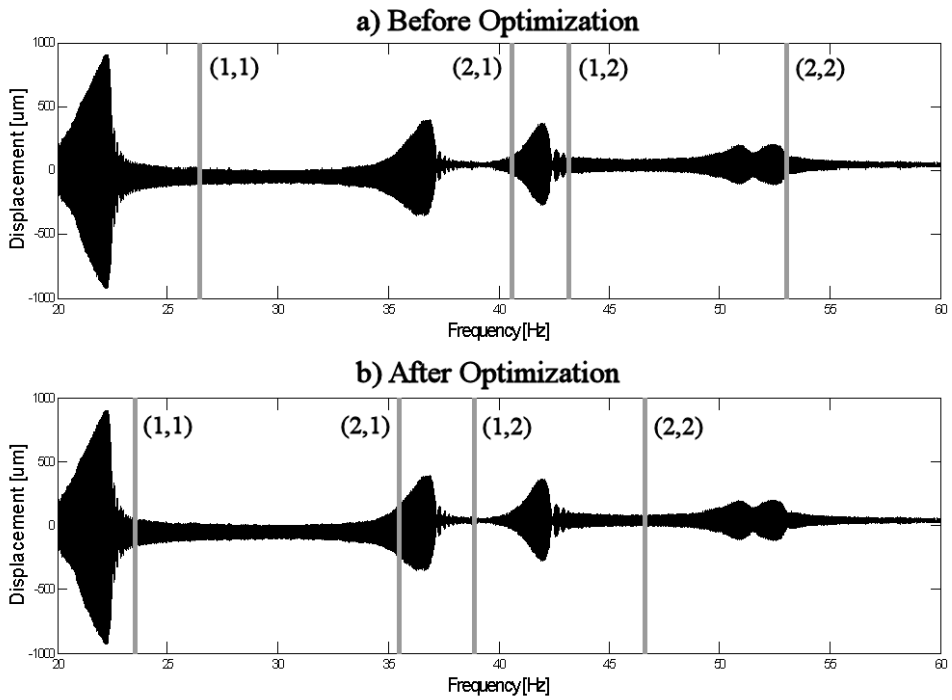
Figure 6.2: Frequencies a) before and b) after optimization showing improvement in the first two modes.

The results of the optimization for the shear modulus suggest that the prediction of the values with the Huber model does not provide an accurate representation of the real value for all cases. The change in shear modulus for the optimization is related to the type of weave of the canvas. That is, for a canvas with a tight compact weave, the behavior is closer to a homogeneous plate which is the concept upon which the Huber model is based. This is the case for cotton canvas in which the predicted value for the shear modulus is representative of the real value and thus a change was not necessary for the optimization. For looser canvasses with more empty space between the yarns, such as for the linen canvasses, the homogeneous plate assumption is less accurate, and thus an increase in shear modulus from the initially predicted value was necessary.

The increase in shear modulus necessary for the optimization of linen canvasses can be explained physically because in the Huber model (p. 43) the friction between the yarns is not considered. For a loose weave, the friction between the yarns will have a greater influence on the shear modulus than for a tight weave, since the yarns have more freedom to move an angle relative to each other under shear stresses. Therefore, for the studied materials, the shear modulus prediction would be better for cotton canvas with a tighter weave because of the lower friction between the yarns as compared to linen.

The values of the shear modulus after optimization for the linen canvasses are still physically realistic since they are only a fraction of the tensile modulus in the weft direction. This is somewhat intuitive since the textiles are easier to shear than to extend in the weft direction. The optimized value of the shear modulus for Rijn linen is 15% of E_1, 13% of E_1 for Waal linen, and 10% of E_1 for Amazone linen. Although the literature available in the shear modulus of textiles is limited, some studies report values up to around 30% or 40% of E_1 [102, 103]. It should be noted however that the values in these studies depend on the assumptions and semi-empirical methods applied in each case.

The results of the optimization show that the change in biaxial tension is specific to each case. For the cases in which a decrease in biaxial tension was necessary to optimize the model, this can be explained physically due to the relaxation that the canvas experiences after being stretched, effectively reducing the tension in the specimen. The greatest decrease in tension of 30% after optimization occurs for cotton canvas in the weft direction. This value is higher compared to the measured value from the relaxation experiments (see Appendix F) in which a maximum relaxation of 11% of the initial load was measured for the warp and 4% for the weft after 20 minutes of applying the load. It should be noted however that relaxation experiments were performed only for Rijn linen, and the relaxation for cotton is probably different.

Although no specific values for the relaxation of cotton were found in the literature, some studies report relaxation values for textiles well up to 40% or higher [104, 105]. Therefore, the optimized cases with a decrease in tension are still within the physically realistic values.

The increase in tension for the optimization of some cases can be explained because in reality the tension along the edge of the specimen is not uniform, and the actual tension value measured by the load cell might have been applied to a smaller portion of the edge causing the effective load per unit length to increase. This is related to the fact that for each experiment, the mounting and tension of the canvas was done manually. Due to the low stiffness properties of the canvas which causes it to easily move from the aligned position, it is very difficult to apply the tension uniformly and in the same way for each case. The greatest increase in tension of 20% after optimization was performed for Amazone linen in the weft direction. In order to have an increase in tension per unit length of 20% with the same total applied force, the effective length at which this force is applied at the clamped edges should be reduced roughly around 20 % as well. This is equivalent to releasing about 1/5 of the clamped edge length, which in a 400 mm specimen is equal to 80 mm. This is still a realistic value considering that it can be caused by an unclamped region of 4 cm in each corner of the clamps.

In an attempt to understand the influence of non-uniform tension in the natural frequencies, a series of simulations with different "gripping" lengths were performed. This was done by releasing progressively the nodes in the rigid body edge where the load was applied. Two cases with non-uniform tension were analyzed. In the first case the nodes were released from the corners towards the center part of the edge as seen in Fig. 6.3a. In the second case the nodes were released progressively from the center towards the corners of the edge as seen in Fig 6.3b.
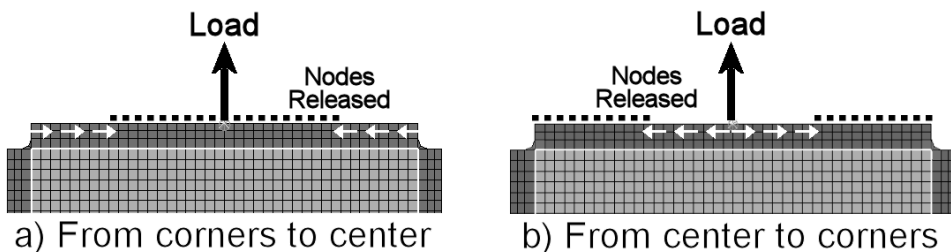

Figure 6.3: Nodes released a) from corners to center b) from center to corners.

Numerical examples of the effect on the predicted natural frequencies caused by releasing the nodes progressively from the corners towards the center of the edges (see Fig. 6.3a) are shown in Fig. 6.4a for Amazone linen with ground and a 10 kg load. The figure shows the frequency values for released lengths of 0, 1/6, 1/3 and 1/2 of the total edge length. The three sets of data in the figure shows the node release performed separately for the weft and warp directions and then for both directions at the same time. It can be seen that releasing the nodes in the weft direction has a higher effect than the warp causing an increase in the natural frequencies for all modes. On the other hand, releasing the nodes in the warp direction caused the frequencies for all modes to decrease. If the nodes are released in both weft and warp directions, there is a superimposed effect in the frequencies but the effect of the release in the weft direction is dominant. Releasing the nodes from the corners would increase the effective load per unit length in the center part of the canvas and thus would increase the frequency values. Interpolating from the frequency values of mode (2,1) in Fig. 6.4a, a release of $1/5^{th}$ of the edge in the weft direction would cause an increase in frequency of 14%. This is approximately the difference between the initial and optimized percentage difference in frequencies for mode (2,1) shown in Table 6.9. This would confirm the hypothesis that the under-prediction of the model for this case could be explained by an unclamped portion of the corners of the edges in the experiment.

Fig. 6.4b shows the effect on the frequencies caused by releasing the nodes from the center towards the corners (see Fig. 6.3b). The effect was the opposite of the previous case. Thus, releasing the nodes in the weft direction caused a decrease in the natural frequencies, while releasing them in the warp caused a slight increase in frequencies. Similarly, the effect of the node release in the weft direction is higher than in the warp and is also dominant when the nodes are released in both directions. The figure only shows the first two modes because due to the uneven distribution of the loading along the edge, clear higher modes were not present in the FE calculation. Releasing the nodes from the center of the clamped edge causes the center part of the canvas to have less tension which in turn causes the frequencies to decrease particularly for the first mode. This indicates that a decrease in the optimized value for the tension can not be explained only by the relaxation of the canvas but also by an unclamped portion of the center of the specimen.

From the sensitivity analysis and optimization work, it can be concluded that the main causes for the differences between model and experiments are the input material properties of the canvas textiles and the application of non-uniform tensile loads since both have a high influence in the results obtained. Further research is needed in these topics in order to improve the accuracy of the model predictions.
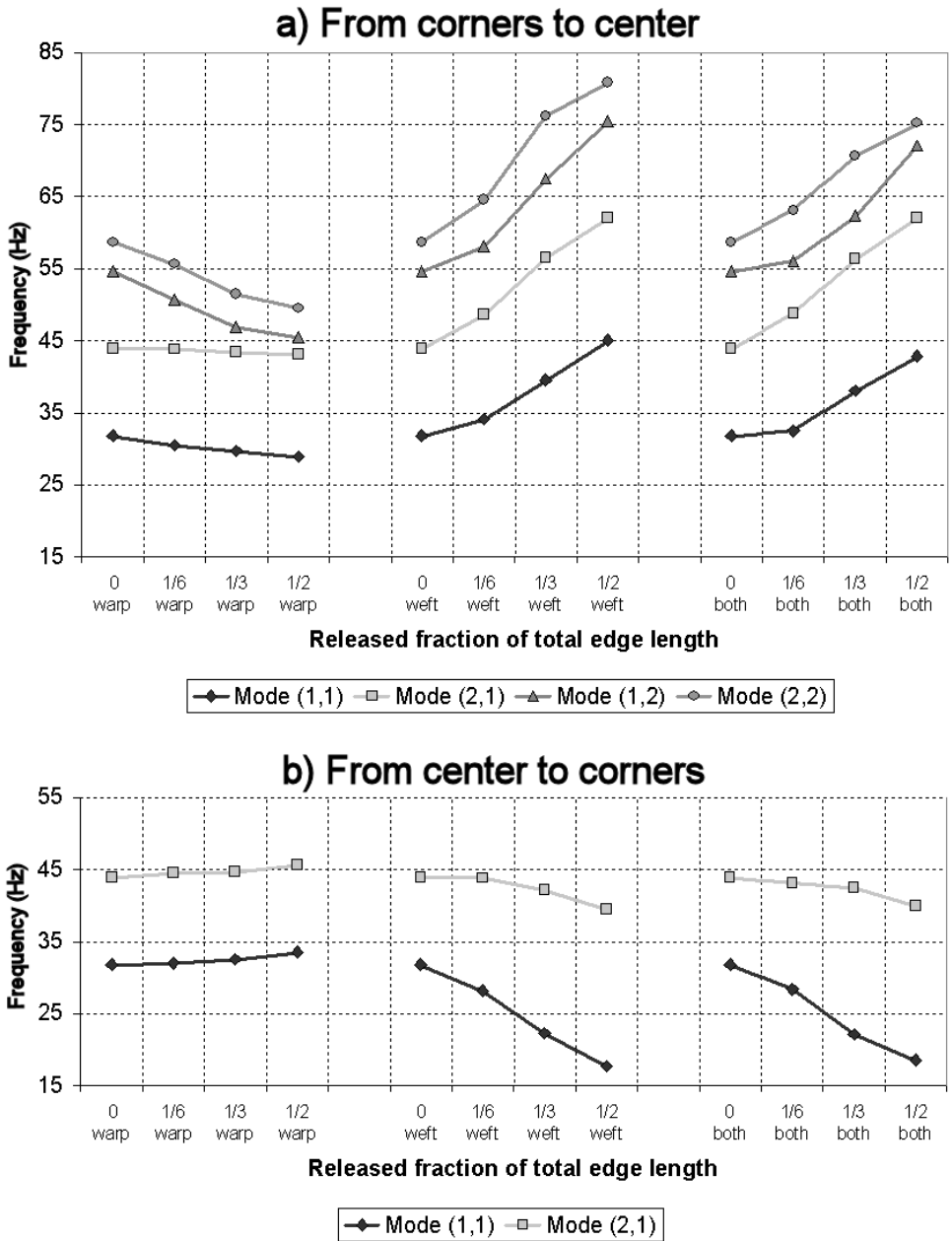
Figure 6.4: Effect of node release from corners to center in the natural frequencies for Amazone linen with ground 10 kg load

The first cause indicates that the material model assumed for the FE simulations does not give an exact representation of the real mechanical behavior of textiles. The material was assumed to behave linearly elastic and the mechanical properties were predicted with semi-empirical methods and adopted models from the literature. Therefore, additional follow-up work is necessary to study the non-linear and visco-elastic material behavior of textiles and to investigate methods of predicting and measuring more accurately the material property values. More specifically, this would involve developing a non-linear material model capable of describing the mechanical properties of textiles (E moduli, shear modulus and Poisson's ratio) and their variation with respect to the loading and time. Further research is also needed to develop appropriate experimental methods for measuring the mechanical properties of textiles particularly for the shear modulus and Poisson's ratio. Given the experimental difficulties to perform these measurements there are no standard procedures available in the literature.

The other main reason for the differences between model and experiments is the non-uniform biaxial tension applied to the canvas specimens which is case specific for each one of the experiments. Therefore, the model is not capable of predicting the frequencies exactly for each case since in the model the tension is assumed to be uniform with perfect boundary conditions. For further studies, it is recommended to investigate experimental methods for applying the tension in the textiles as uniformly as possible to improve the repeatability in the tension for each case. It is also suggested to further investigate the effect that the non-uniform tension has in the vibration behavior of the canvas, since this would be the case for real paintings. This would involve further modeling work simulating the way the non-uniform tension is applied manually in reality. Experimental methods to apply controlled non-uniform tension to replicate the manual stretching process would also be necessary.

6.3   Application to Canvas Paintings

The objective of this project was to develop a computer (finite element) model to simulate the way a canvas painting vibrates with an understanding of the parameters that influence the painting's vibration behavior. The way a canvas painting responds to vibration excitation depends on the natural frequencies and associated mode shapes of the painting. These are intrinsic properties that will depend on the physical and mechanical characteristics of the painting. A natural frequency, as its name would suggest, is the frequency at which the painting vibrates naturally when given an initial impulse. In analogy to a guitar string, for example, when the string is plucked it will vibrate at a

certain characteristic frequency which can be heard as the pitch of the sound produced. Given that this is the frequency at which the painting 'likes' to vibrate naturally, when a vibration source excites the painting at its natural frequency, the movement of the canvas would be much larger than when it is excited at other arbitrary frequencies. *This phenomenon is known as resonance and it is the potentially most dangerous condition since there are high vibration amplitudes that can produce the most damage to the painting.*

The model developed in this project can be applied in real case studies in order to estimate the lower natural frequency values for specific paintings. These lower frequencies and modes (particularly the first mode) will be the ones dominating the response of the canvas to vibration excitation and will potentially be the most damaging to the painting since higher amplitudes are involved. This prediction is useful in order to avoid direct vibration excitation at the frequency range in which these lower modes are included. Additionally, the model can assist on designing packaging or protective methods in order to 'tune' them so that these lower modes are not triggered. The natural frequencies of a specific canvas painting will be dependent on many factors such as its size, the tension, the weight and the stiffness. However, for the majority of paintings within a wide range of average characteristics, the lower natural frequencies will be situated below 150 Hz. Therefore, *in general it is advisable that paintings are exposed as little as possible to vibrations on the low-end frequency spectra in order to avoid resonance of the canvas at the dominant lower natural frequencies.*

The vibration damage produced in canvas paintings is a fatigue phenomenon that can be illustrated in a typical S-N diagram shown schematically in Fig. 6.5. The Y axis corresponds to the amplitude (A) of vibration or stress, and the X axis corresponds to the number of vibration cycles (N). *The damage (delamination crack growth) produced at a specific amplitude accumulates in terms of the number of vibration cycles to which the painting is exposed.* In the S-N curve, the total number of loading cycles until failure (e.g. paint loss) is plotted as a function of the corresponding amplitude value. At the extreme case with highest amplitudes, a shock load or corner impact on the frame of the painting can be taken as an example. In this case only one or a few severe loading cycles (N_1) of high amplitude (A_1) would be enough to produce paint loss. As the amplitudes decrease although still at a high level (A_2), such as the vibrations produced when a painting is transported by a truck or an airplane for example, there will be a certain number of vibration cycles (N_2) which will have to take place for paint loss to occur. This would be the fatigue life of the painting at that particular amplitude. Reducing the vibration amplitudes even further (A_3), take for example the case of road traffic noise nearby a museum, the number of vibration cycles required to produce paint loss would

be higher (N_3) and thus the fatigue life of the painting would increase. *If the vibration amplitudes are reduced below a theoretical threshold value called the fatigue limit, then crack growth does not occur and the painting can be exposed to these vibration amplitudes* (e.g. A_4) *for extended periods of time without accumulating damage. This would be the ideal case regarding canvas vibration and it would mean that the painting has an infinite fatigue life below this limit.*

The reason for reducing vibrations in sensitive canvas paintings is to avoid further crack growth and eventual paint loss from the canvas, or to extend the time until the loss of paint would occur as long as possible. Generally speaking, lower natural frequencies are related to higher amplitudes and higher natural frequencies to lower amplitudes. Therefore, intuitively this would mean that resonance of the canvas at lower frequencies would produce more damage than resonance at higher frequencies. However, this would not always be the case. *Although resonance at higher frequencies generally involves lower amplitudes, it also means that there is a higher number of loading cycles for the same period of vibration time exposure.* From the S-N curve in Fig. 6.5, it can be seen that a greater number of loading cycles (N) would also mean that a greater part of the total fatigue life (No. of cycles until paint loss e.g. N_2 or N_3) may have been consumed. Thus, there must be a balance between the amplitude reduction and the increase in loading cycles due to higher vibration frequencies. For this reason, *research on the fatigue behavior of sensitive canvas paintings is needed in order to determine the relationship between vibration amplitude and damage* as in such S-N curves, and establish the vibration limits at which cracking would not occur.

There are two general paths by which vibrations can travel from the excitation source to the canvas. One is by structural means (structure borne) through the stretcher frame, museum wall, hanging system or packing case. The second one is through the air (airborne) in the form of sound pressure waves. The model developed can be readily used to simulate the response of a painting to airborne excitation. This can be modeled in the same way in which the forced response analysis was performed in Section 3.3. Here the sound waves are modeled as a pressure force distributed over an area of the canvas. In order to simulate structure borne excitation, it is necessary to develop the current model a step further. This is due to the way in which the excitation or vibration load is applied through the structure or frame. In the current model the frame (boundary conditions) is considered to be fixed and only the canvas can vibrate. Thus, an additional analysis called 'base excitation' is necessary in order to apply the vibration loading to the frame where the canvas is supported. It should be noted that the free vibration analysis (frequency extraction) will be the same as the one performed in Section 3.3 since the natural frequencies and mode shapes will not change for both cases.
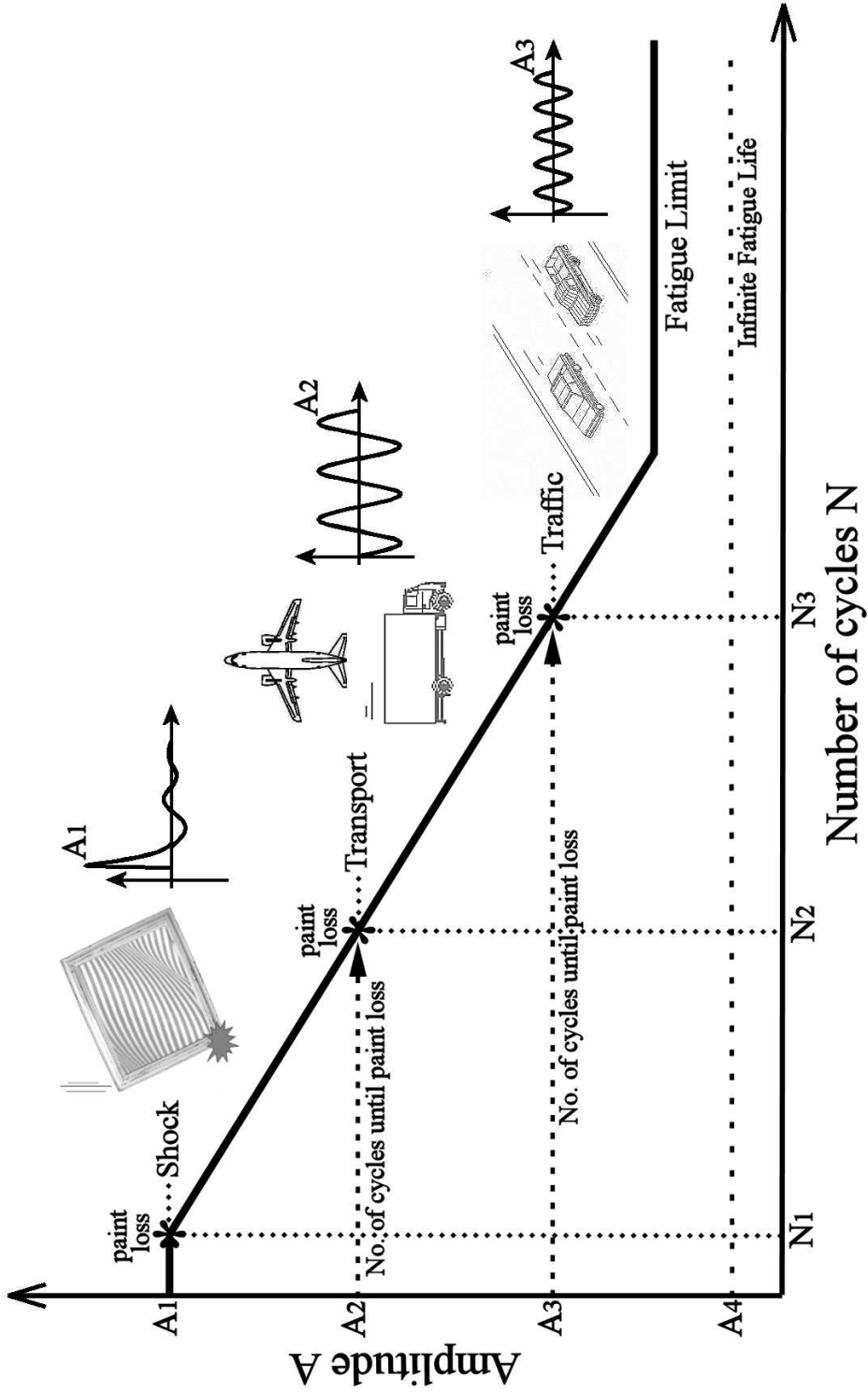
Figure 6.5: S-N curve shown schematically to illustrate the fatigue life of sensitive canvas paintings

The difference would be in the way in which the vibration loads are applied in the forced response analysis.

The current model can also be used as a basis to develop more complicated models in order to simulate specific vibration scenarios and investigate possible solutions to reduce vibration levels, such as packing and hanging systems, or the design of protective methods against vibration excitation. In this way, the effect that these additional components have on the dynamic behavior of the entire system can be analyzed. It should be realized that changes in the system would produce a shift in the natural frequencies and a difference in vibration amplitudes. Ideally, the shift in natural frequencies of the system should move out of the frequency range of the excitation sources to avoid resonances. Otherwise it would be desirable to lower the vibration amplitudes below the paint cracking threshold.

For example, *it is believed that increasing the tension in the canvas would be beneficial regarding vibration effects since there would be a decrease in amplitudes. However, this is not recommended.* The stretching itself may cause stresses in the paint films, thus enhancing the stresses produced during vibration loading due to an increase in the average stress value. Moreover, higher stretching produces an increase in the natural frequencies. Thus, resonance at these higher frequencies would increase the number of loading cycles per time and possibly accumulating more damage of the total fatigue life, as described previously. At the other extreme, a slack or buckled canvas will in theory have no vibratory motion. This behavior will be similar to an instrument string without tension. Therefore in terms of vibration response, it might be beneficial for the painting because no vibration will occur and thus no cyclic stresses in the paint. However, other problems such as paint flakes under compression should be considered in this case.

The use of backing boards is also a method commonly thought to improve the vibration of the canvas. A backing board will effectively produce an air cushion which acts as a source of surface pressure on the back of the canvas. This will produce a stiffening effect on the bending of the canvas causing an increase in the natural frequencies of the system. Again, higher frequencies involve an increase in the number of loading cycles and possibly increasing the damage accumulated over time. The ideal situation is if vibration amplitudes decrease below the cracking threshold so that no damage is produced. Additionally, it is advisable that the entire system is analyzed to make sure that the natural frequencies of the board do not overlap with the natural frequencies of the canvas so that they do not resonate together causing an amplification of the response over a range of frequencies. Thus, *a thorough investigation is needed to determine if this method is producing the desired effects.*

Packaging and hanging methods for paintings should damp incoming vibration loads from the structural path and airborne vibration. In general, low frequency vibrations with values below 500 Hz will be mainly transmitted through a structural path such as the frame or hanging systems, while higher frequency vibrations above 1000 Hz will be transmitted mainly through the air (sound/noise). From 500 to 1000 Hz there would be an overlap between both paths. Since the dominant natural frequencies of a painting would be located generally in the low frequency range (<150 Hz), the structural supports of the painting should be well isolated from the vibration excitation. Simple vibration isolators in a canvas painting scenario are shown schematically in Fig. 6.6. Ideally, *a vibration isolator should include springs to support the mass of the painting, and dampers to absorb any kinetic energy that the painting may have to eventually bring the painting to rest. The main problem with typical packaging methods for paintings is that dampers are not included; only suspension straps or springs are used, which effectively produce an oscillatory system.* Both packaging and hanging systems should include springs and dampers that can be designed for specific frequency ranges depending on the characteristics of the painting. The airborne excitation can be stopped by placing barriers of material between the acoustic source and the painting. Protective packing or display cases are recommended to isolate the painting from airborne excitation. The cases should have a high stiffness so that their resonance frequencies are high and would not excite the lower natural frequencies of the canvas. Additionally, cushioning foams and pads are also recommended at structural connections. For critical applications more effective, but expensive methods such as pneumatic isolators and active vibration isolation systems can be used.
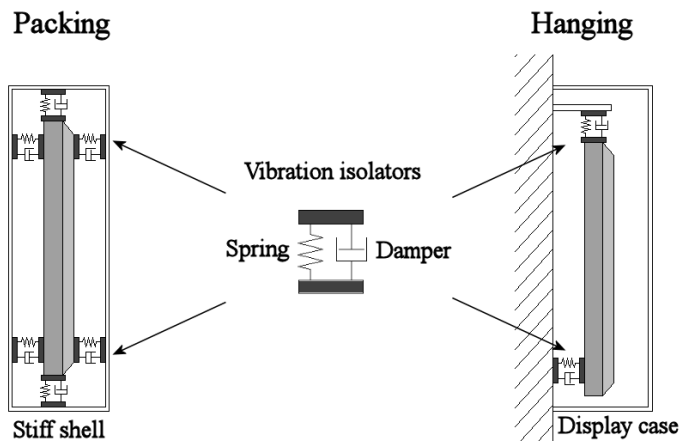

Figure 6.6: Vibration isolation scheme for packing and hanging of paintings

Chapter 7

Conclusions and Recommendations

7.1 Conclusions

A project was conducted to develop a finite element model for characterizing the vibration of canvas paintings. The goal was to be able to predict the behavior of a painting under vibration loading, and to obtain a fundamental understanding of the parameters involved. Vibration experiments were carried out in order to verify and optimize the model by comparing the predicted natural frequencies and mode shapes to those measured on canvas specimens. The following conclusions can be drawn from the modeled and experimental results:

- Canvas paintings can be modeled as orthotropic laminated plates under biaxial tension. They behave as thin plates with low bending stiffness causing the vibration behavior to be dominated by the canvas tension.

- The most important parameters that influence the natural frequencies and mode shapes of paintings are the tension and the uniformity in which is applied to the canvas, the shear modulus of the textile, and the mass of the canvas and paint layers.

- An optimization of the model was required to reduce the initial differences between the predicted and measured natural frequencies for the first four dominant vibration modes of the canvas. The optimized model was capable of predicting the first two natural frequencies with differences within 5% compared to the experimental values.

- The main reasons for the differences between model and experiments are the non-uniform biaxial tension applied during the tests and the simplified linear elastic material model adopted for canvas textiles.

7.2   Recommendations

The following recommendations are made for further studies:

- Follow-up work to include the non-linear and viscoelastic characteristics of canvas textiles is necessary to improve the accuracy of the vibration model. This involves developing appropriate experimental methods and predictive models to determine the macro-mechanical properties of the textile with an investigation of their relationship to the micro-mechanics, including yarn interactions and friction.

- Further modeling and experimental work is suggested to investigate the effect of non-uniform tension on the vibration behavior of the canvas since this is the case for real paintings in which the stretching process is handwork.

- The study and simulation of real-life load cases and museum scenarios such as packing and hanging systems are suggested to assist in the design and implementation of protective methods against vibration excitation.

- Research to characterize the fatigue delamination of paint films in sensitive paintings is needed to establish the relationship between canvas vibration and damage. This will allow a complete description of the problem in order to determine tolerable vibration levels and provide guidelines for vibration exposure of paintings.

Appendix A

Derivation of Analytical Model

This appendix presents a detailed derivation of the equations considered for the analytical model of the free vibration of a canvas painting, as described in Section 3.1. This model considers the canvas as a thin laminated plate consisting of the different layers of the painting. In order to derive an expression for the natural frequencies of the plate, the kinematic, constitutive and dynamic equilibrium equations are solved using classical laminate theory.

Kinematic Equations

The kinematic equations for the plate can be derived from the first Kirchhoff assumption (see Section 3.2). This assumption states that the lines that are normal to the mid-plane of the plate remain straight, normal and inextensional during deformation. The first Kirchhoff assumption is illustrated in Fig. A.1 for the y, z plane. The figure shows the cross section of a plate of thickness h before and after deformation. The mid-plane lies on the x, y coordinates in the undeformed configuration. The line in the z direction normal to the mid-plane in the undeformed configuration (Fig. A.1a) is assumed to remain straight and perpendicular to the mid-plane when the laminate is extended and bent (Fig. A.1b).

As a consequence of this assumption, the laminate displacement components $\bar{u}, \bar{v}, \bar{w}$ are expressed in terms of the mid-plane displacements u, v, w by
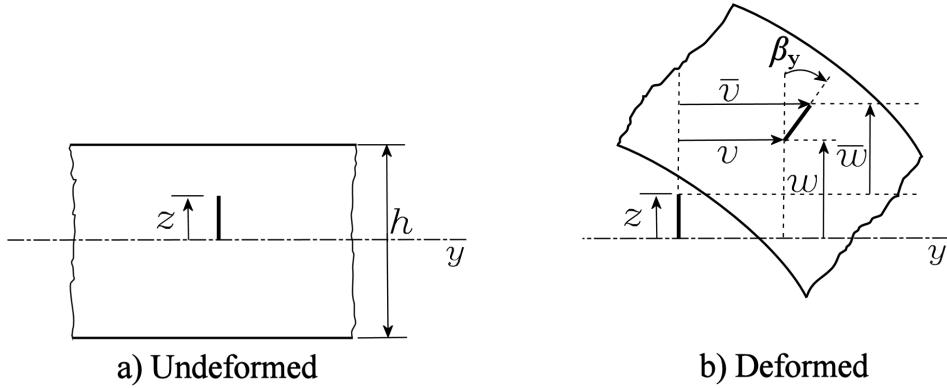
Figure A.1: Normal line to mid-plane before and after deformation.

$$\bar{u} = u + z\beta_x$$
$$\bar{v} = v + z\beta_y \tag{A.1}$$
$$\bar{w} = w$$

where the rotations β_x and β_y are assumed to be small so that $sin\beta \approx \beta$. The rotations are equal to the slope of the mid-plane with respect to the x and y directions

$$\beta_x = -w_{,x}$$
$$\beta_y = -w_{,y} \tag{A.2}$$

where a comma denotes differentiation with respect to x or y. Furthermore for a geometrically non-linear theory that considers small strains, moderate rotations relative to x and y, and negligible rotations relative to z; the non-linear strain-displacement relations are [62]

$$\bar{\epsilon}_x = \bar{u}_{,x} + \tfrac{1}{2}\beta_x^2$$
$$\bar{\epsilon}_y = \bar{v}_{,y} + \tfrac{1}{2}\beta_y^2 \tag{A.3}$$
$$\bar{\gamma}_{xy} = (\bar{u}_{,y} + \bar{v}_{,x}) + \bar{w}_{,x}\bar{w}_{,y}$$

where $\bar{\epsilon}_x$, $\bar{\epsilon}_y$ and $\bar{\gamma}_{xy}$ are extensional and shearing strains at an arbitrary point in the plate. Introducing the derived displacements u and v from Eqs. A.1 and rearrangement gives

$$\bar{\epsilon}_x = \epsilon_x + z\kappa_x$$
$$\bar{\epsilon}_y = \epsilon_y + z\kappa_y \tag{A.4}$$
$$\bar{\gamma}_{xy} = \gamma_{xy} + 2z\kappa_{xy}$$

where ϵ_x, ϵ_y and γ_{xy} are mid-plane strains, and κ_x, κ_y and κ_{xy} are the curvatures and twist curvature of the mid-plane respectively. The kinematic relations for a plate are thus,

$$\begin{array}{lll} \epsilon_x = u_{,x} + \frac{1}{2}\beta_x^2 & \kappa_x = \beta_{x,x} & \beta_x = -w_{,x} \\ \epsilon_y = v_{,x} + \frac{1}{2}\beta_y^2 & \kappa_y = \beta_{y,y} & \beta_y = -w_{,y} \\ \gamma_{xy} = (u_{,y} + v_{,x}) + \beta_x\beta_y & \kappa_{xy} = \beta_{x,y} + \beta_{y,x} \end{array} \tag{A.5}$$

Note that all of the variables in the equations are averaged to the mid-plane and are a function of x and y only.

Constitutive Equations

The stresses and strains in the laminate are obtained from the properties of the constituent plates using Classical Laminate Theory [106]. The macromechanical behavior of the plates are assumed to be described by their averaged mechanical properties, rather than the detailed interactions of the constituent materials (e.g. canvas textile friction and uncrimping). The materials are assumed to have linear elastic behavior that can be described by the generalized Hooke's law written in matrix form as

$$\sigma_i = C_{ij}\epsilon_j \qquad i, j = 1, \ldots, 6 \tag{A.6}$$

where σ_i are the stress components, C_{ij} is the stiffness matrix, and ϵ_j are the strain components. Since the plates are thin, the second Kirchhoff assumption states that the transverse normal stresses may be neglected given that they are small as compared to the longitudinal normal stresses. This assumption leads to the following simplifications

$$\sigma_3 = 0, \ \tau_{23} = 0, \ \tau_{31} = 0 \tag{A.7}$$

which define the so-called plane stress condition.

The plate corresponding to the canvas, shown in Fig. A.2, is considered to be orthotropic because the weft and warp set of yarns define two orthogonal
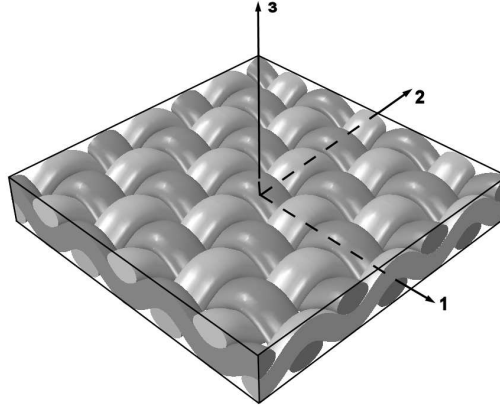
Figure A.2: Canvas modeled as orthotropic plate

planes of material property symmetry. Moreover, the yarn directions coincide with the 1-2 plane of the rectangular coordinate system used. Thus, the stress-strain relations for the orthotropic plate are given by

$$
\left\{
\begin{array}{c}
\sigma_1 \\
\sigma_2 \\
\tau_{12}
\end{array}
\right\} =
\left[
\begin{array}{ccc}
Q_{11} & Q_{12} & 0 \\
Q_{12} & Q_{22} & 0 \\
0 & 0 & Q_{66}
\end{array}
\right]
\left\{
\begin{array}{c}
\epsilon_1 \\
\epsilon_2 \\
\gamma_{12}
\end{array}
\right\}
\tag{A.8}
$$

where Q_{ij} are the so-called reduced stiffness coefficients of the plate. In terms of engineering constants these coefficients are

$$
\begin{aligned}
Q_{11} &= \frac{E_1}{1 - \nu_{12}\,\nu_{21}} \\[2mm]
Q_{12} &= \frac{\nu_{12}\,E_2}{1 - \nu_{12}\,\nu_{21}} = \frac{\nu_{21}\,E_1}{1 - \nu_{12}\,\nu_{21}} \\[2mm]
Q_{22} &= \frac{E_2}{1 - \nu_{12}\,\nu_{21}} \\[2mm]
Q_{66} &= G_{12}
\end{aligned}
\tag{A.9}
$$

Four independent material properties define the orthotropic stiffness matrices: two elastic moduli E_1 and E_2 for the weft and the warp respectively, the Poisson's ratio ν_{12}, and the shear modulus G_{12}. Additionally, from the reciprocal theorem of Betti [72], the relationship between the elastic constants is

$$\frac{\nu_{12}}{E_1} = \frac{\nu_{21}}{E_2} \tag{A.10}$$

The plates corresponding to the ground and paint layers are considered to be isotropic since there are no preferred directions in the material. The stress-strain relations for an isotropic plate are given by

$$\left\{ \begin{array}{c} \sigma_1 \\ \sigma_2 \\ \tau_{12} \end{array} \right\} = \left[\begin{array}{ccc} Q_{11} & Q_{12} & 0 \\ Q_{12} & Q_{11} & 0 \\ 0 & 0 & Q_{66} \end{array} \right] \left\{ \begin{array}{c} \epsilon_1 \\ \epsilon_2 \\ \gamma_{12} \end{array} \right\} \tag{A.11}$$

The isotropic relations in terms of engineering constants can be obtained from the orthotropic relations by equating E_1 and E_2 to E, ν_{12} and ν_{21} to ν, and G_{12} to G which yields

$$Q_{11} = \frac{E}{1 - \nu^2}$$

$$Q_{12} = \frac{\nu E}{1 - \nu^2} \tag{A.12}$$

$$Q_{66} = \frac{E}{2(1 + \nu)} = G$$

where only two of the three material properties (E, ν, G) are independent. The internal force and moment resultants that act on an infinitesimal laminate element $dx\,dy$ are shown in Fig. A.3 [61, 62].

The resultants are obtained by integration of the stresses in each layer through the laminate thickness by

$$\begin{aligned}
N_x &= \int_{-h/2}^{h/2} \bar{\sigma}_x \, dz & N_y &= \int_{-h/2}^{h/2} \bar{\sigma}_y \, dz \\
N_{xy} &= \int_{-h/2}^{h/2} \bar{\tau}_{xy} \, dz & N_{yx} &= \int_{-h/2}^{h/2} \bar{\tau}_{yx} \, dz \\
M_x &= \int_{-h/2}^{h/2} \bar{\sigma}_x z \, dz & M_y &= \int_{-h/2}^{h/2} \bar{\sigma}_y z \, dz \\
M_{xy} &= \int_{-h/2}^{h/2} \bar{\tau}_{xy} z \, dz & M_{yx} &= \int_{-h/2}^{h/2} \bar{\tau}_{yx} z \, dz
\end{aligned} \tag{A.13}$$

where N_x, N_y, N_{xy}, N_{yx} are forces per unit length (width) of the cross section of the laminate and M_x, M_y, M_{xy}, M_{yx} are moments per unit length.
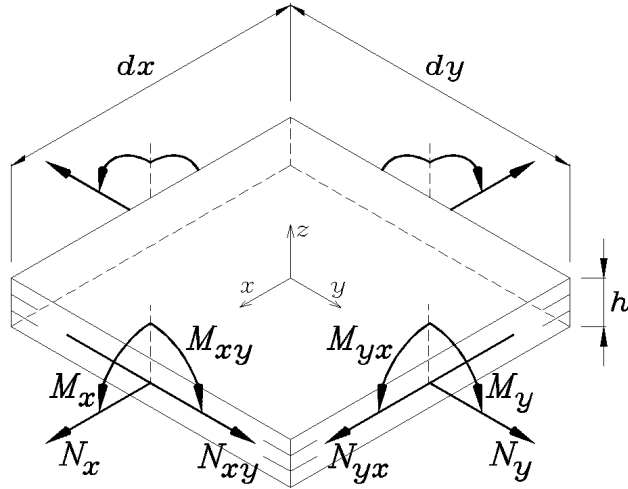
Figure A.3: Force and moment resultants on a laminate.

A canvas painting composed of an orthotropic plate (canvas) and multiple isotropic plates (ground and paint) results in an orthotropic laminate. Additionally it can be seen from Fig. 3.3, see also Fig. A.4, that the stacking sequence results in a laminate which is asymmetric about the mid-plane. The force and moment resultants of an orthotropic laminate which is asymmetric about the mid-plane are [75].

$$
\left\{ \begin{array}{c} N_x \\ N_y \\ N_{xy} \end{array} \right\} = \left[\begin{array}{ccc} A_{11} & A_{12} & 0 \\ A_{12} & A_{22} & 0 \\ 0 & 0 & A_{66} \end{array} \right] \left\{ \begin{array}{c} \epsilon_x \\ \epsilon_y \\ \gamma_{xy} \end{array} \right\} + \left[\begin{array}{ccc} B_{11} & B_{12} & 0 \\ B_{12} & B_{22} & 0 \\ 0 & 0 & B_{66} \end{array} \right] \left\{ \begin{array}{c} \kappa_x \\ \kappa_y \\ \kappa_{xy} \end{array} \right\} \quad \text{(A.14)}
$$

$$
\left\{ \begin{array}{c} M_x \\ M_y \\ M_{xy} \end{array} \right\} = \left[\begin{array}{ccc} B_{11} & B_{12} & 0 \\ B_{12} & B_{22} & 0 \\ 0 & 0 & B_{66} \end{array} \right] \left\{ \begin{array}{c} \epsilon_x \\ \epsilon_y \\ \gamma_{xy} \end{array} \right\} + \left[\begin{array}{ccc} D_{11} & D_{12} & 0 \\ D_{12} & D_{22} & 0 \\ 0 & 0 & D_{66} \end{array} \right] \left\{ \begin{array}{c} \kappa_x \\ \kappa_y \\ \kappa_{xy} \end{array} \right\} \quad \text{(A.15)}
$$

where the coefficients A_{ij} are the extensional stiffnesses, B_{ij} are the coupling stiffnesses, and D_{ij} are the bending stiffness. The asymmetry of the laminate about the mid-plane produces coupling between bending and extension which is implied from B_{ij}. Thus, extensional forces result in twisting and/or bending deformations, and moments result in extension of the mid-plane. The stiffness coefficients are given by the following expressions [61]:

$$A_{ij} = \sum_{k=1}^{N}(Q_{ij})_k(z_k - z_{k-1})$$

$$B_{ij} = \frac{1}{2}\sum_{k=1}^{N}(Q_{ij})_k(z_k^2 - z_{k-1}^2) \qquad \text{(A.16)}$$

$$D_{ij} = \frac{1}{3}\sum_{k=1}^{N}(Q_{ij})_k(z_k^3 - z_{k-1}^3)$$

where $(Q_{ij})_k$ represents the stiffness coefficients of the kth layer, and z_k and z_{k-1} are defined in Fig. A.4.

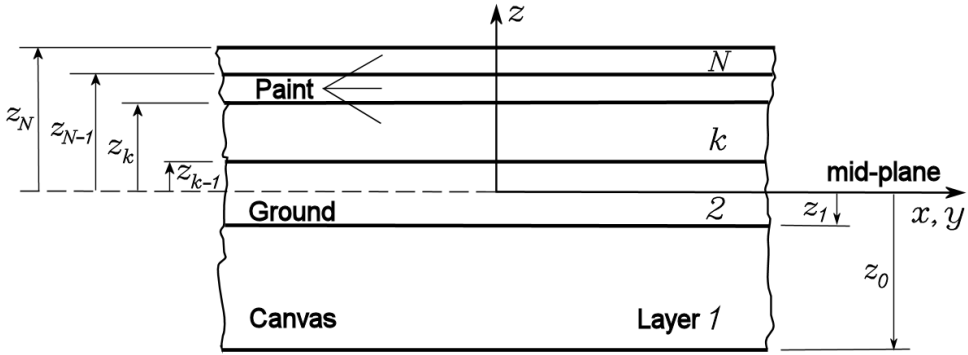Figure A.4: N-layered canvas painting laminate asymmetric about the mid-plane.

There are very few cases that have an exact solution for laminates with coupling coefficients in vibration problems. Closed form solutions for cross-ply plates with two simply supported opposite boundaries and antisymmetrically laminated plates are described in Qatu (2004) [107]. Different lamination sequences or boundary conditions from the ones mentioned previously have no exact solution. Approximate methods such as the Ritz, Galerkin or the finite element method are required for the analysis of these laminates. In order to obtain an analytical solution as a first approximation, the coupling terms B_{ij} are neglected so that the constitutive equations (Eq. A.14 and Eq. A.15) reduce to

$$\left\{ \begin{array}{c} N_x \\ N_y \\ N_{xy} \end{array} \right\} = \left[\begin{array}{ccc} A_{11} & A_{12} & 0 \\ A_{12} & A_{22} & 0 \\ 0 & 0 & A_{66} \end{array} \right] \left\{ \begin{array}{c} \epsilon_x \\ \epsilon_y \\ \gamma_{xy} \end{array} \right\} \qquad \text{(A.17)}$$

$$
\left\{ \begin{array}{c} M_x \\ M_y \\ M_{xy} \end{array} \right\} = \left[\begin{array}{ccc} D_{11} & D_{12} & 0 \\ D_{12} & D_{22} & 0 \\ 0 & 0 & D_{66} \end{array} \right] \left\{ \begin{array}{c} \kappa_x \\ \kappa_y \\ \kappa_{xy} \end{array} \right\}
\tag{A.18}
$$

These are equivalent to the force and moment resultants of a single homogeneous orthotropic plate. However, the stiffness coefficients A_{ij} and D_{ij} are calculated from Classical Laminate Theory using Eqs. A.16.

Dynamic Equilibrium Equations

To derive the nonlinear equilibrium equations an infinitesimal plate element is considered in a slightly deformed configuration as shown in Fig. A.5. This accounts for the nonlinear interaction between forces and rotations. The force and moment resultants are shown in separate diagrams for clarity. The notation N_x^+, for example, is used to denote $(N_x + N_{x,x}\, dx)$ because the force and moment resultants vary across the element. The rotations β_x and β_y are assumed to be small so that $sin\beta \approx \beta$ and $cos\beta \approx 1$.

The static equilibrium equations are obtained from summation of forces and moments in the x, y and z directions. The simplified and rearranged equilibrium equations can be written in the following compact form [108]:

$$
N_{x,x} + N_{xy,y} = 0
$$

$$
N_{xy,x} + N_{y,y} = 0
\tag{A.19}
$$

$$
M_{x,xx} + 2M_{xy,xy} + M_{y,yy} + N_x w_{,xx} + 2N_{xy} w_{,xy} + N_y w_{,yy} = -P
$$

Substitution of the constitutive equations (Eq. A.18) into the out of plane equilibrium equation (Eq. A.19) yields

$$
D_{11}\kappa_{x,xx} + D_{12}(\kappa_{y,xx} + \kappa_{x,yy}) + 2D_{66}\kappa_{xy,xy} + D_{22}\kappa_{y,yy}
$$
$$
+ N_x w_{,xx} + 2N_{xy} w_{,xy} + N_y w_{,yy} = -P
\tag{A.20}
$$

Substitution of the kinematic equations (Eq. A.5) in Eq. A.20, and rearrangement yields the static out-of-plane equilibrium equation

$$
D_{11} w_{,xxxx} + 2(D_{12} + 2D_{66})w_{,xxyy} + D_{22} w_{,yyyy}
$$
$$
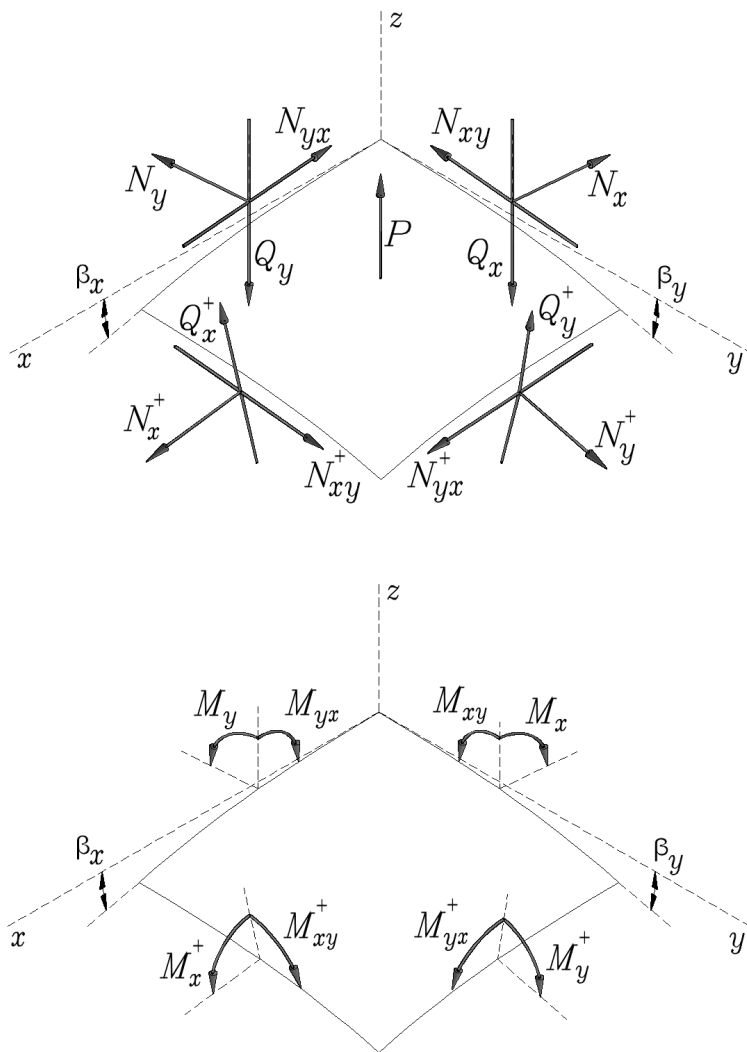- (N_x w_{,xx} + 2N_{xy} w_{,xy} + N_y w_{,yy}) = P
\tag{A.21}
$$

Figure A.5: Infinitesimal plate element in deformed configuration.

The dynamic equilibrium equation is obtained by adding a mass inertia term to the static equilibrium equation (D'Alembert's principle). Further, the surface load component P and the shear forces N_{xy} are zero for this case which gives

$$D_{11}w_{,xxxx} + 2(D_{12} + 2D_{66})w_{,xxyy} + D_{22}w_{,yyyy}$$
$$-(N_x w_{,xx} + N_y w_{,yy}) + \bar{m}w_{,tt} = 0 \tag{A.22}$$

where $\bar{m}$ is the mass per unit area of the laminate. Note that only out-of-plane displacements are present in the equation.

Solution

The non-linear dynamic equilibrium equations can be linearized by application of the adjacent equilibrium criterion [109]. The criterion consists of giving small increments $(u^{(1)}, v^{(1)}, w^{(1)})$ to the displacement variables

$$u \rightarrow u^{(0)} + u^{(1)}$$
$$v \rightarrow v^{(0)} + v^{(1)} \tag{A.23}$$
$$w \rightarrow w^{(0)} + w^{(1)}$$

that define two adjacent configurations, a pre-vibration (stretching) state $(u^{(0)}, v^{(0)}, w^{(0)})$ and a vibration state $(u^{(1)}, v^{(1)}, w^{(1)})$. The displacement increment causes a change in the forces

$$N_x \rightarrow N_x^{(0)} + N_x^{(1)}$$
$$N_y \rightarrow N_y^{(0)} + N_y^{(1)} \tag{A.24}$$
$$N_{xy} \rightarrow N_{xy}^{(0)} + N_{xy}^{(1)}$$

The diplacement and force increments (Eq. A.23 and Eq. A.24) are substituted in Eq. A.22. Considering that for in-plane loading in the stretching state, the out-of-plane displacements $w^{(0)}$ and their derivatives are zero, and neglecting the quadratic terms (e.g. $N_x^{(1)}w_{,xx}^{(1)}$) because of the smallness of the incremental displacements, this gives

$$D_{11}w_{,xxxx}^{(1)} + 2(D_{12} + 2D_{66})w_{,xxyy}^{(1)} + D_{22}w_{,yyyy}^{(1)}$$
$$-(N_x^{(0)}w_{,xx}^{(1)} + N_y^{(0)}w_{,yy}^{(1)}) + \bar{m}w_{,tt}^{(1)} = 0 \tag{A.25}$$

that is a homogeneous and linear equation in $w^{(1)}$ with variable coefficients in $N_x^{(0)}, N_y^{(0)}$. Recall from Fig. 3.2 that the laminate is considered to have simply supported edges for which the boundary conditions take the simple form:

$$at\ x = 0, a \ \rightarrow \ w = 0$$

$$at\ y = 0, b \ \rightarrow \ w = 0$$

It can be observed that the differential equation and the boundary conditions are satisfied by a solution that consists of a spatial displacement function and a harmonic time variation of the form

$$w^{(1)}(x, y, t) = W_{mn} \sin\left(\frac{m\pi x}{a}\right) \sin\left(\frac{n\pi y}{b}\right) \cos \omega_{mn} t \qquad \text{(A.26)}$$

where ω represents the circular frequency, W_{mn} represents the arbitrary scaled amplitude, and m and n represent the number of half waves in the x and y direction. This equation corresponds to the mode shapes of the plate also given in Eq. 3.2 in Section 3.1. Differentiation and substitution of the solution (Eq. A.26) in the dynamic equilibrium equation (Eq. A.25) yields

$$
\begin{aligned}
\omega_{mn}^2 = \frac{\pi^4}{\bar{m}} & \left[D_{11}\left(\frac{m}{a}\right)^4 + 2\left(D_{12} + 2D_{66}\right)\left(\frac{m}{a}\right)^2\left(\frac{n}{b}\right)^2 + D_{22}\left(\frac{n}{b}\right)^4 \right] \\
+ \frac{\pi^2}{\bar{m}} & \left[N_x\left(\frac{m}{a}\right)^2 + N_y\left(\frac{n}{b}\right)^2 \right]
\end{aligned}
\qquad \text{(A.27)}
$$

which is Eq. 3.1 in Section 3.1. This expression gives the natural frequencies ω_{mn} with the corresponding mode shapes m, n of the simply supported laminated plate.

Appendix B

Overview of the Finite Element Method

The basic concept of the FE method is the subdivision of the continuous system into a finite number of elements of simple geometry called *finite elements*. The process consists then on finding the solution of the complete system by rebuilding it from the individual elements whose behaviour is completely understood and all the parameters are defined [59]. The elements may be straight lines or curved segments for one dimensional cases, triangular or quadrilateral for two dimensional cases, and tetrahedral or hexahedral for three dimensional cases.
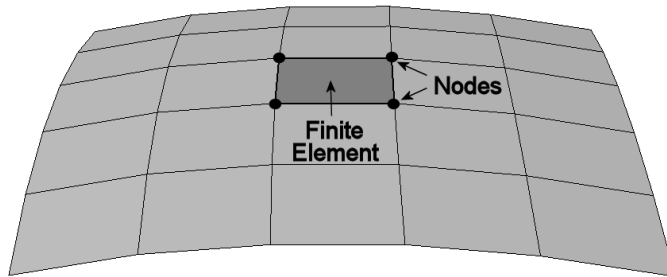
Figure B.1: Discretized shell showing finite elements and nodes

The geometry of the elements is defined by a set of points called *nodes* situated on their boundaries where neighbour elements are connected to each other, see Fig. B.1. In problems dealing with elastic solids, the variables (unknowns to be solved) are the displacements of these nodal positions, also called *degrees of freedom* (DOF). Since the displacements in the region be-

tween the nodes are unknown, simple (interpolation) equations are chosen to describe and define the displacements within the element in terms of the nodal displacements. The global equations for the system can be obtained by assembling, in matrix form, all the individual element equations. Finally, the solution for the unknown displacements is obtained by replacing certain known displacement values into the system of equations. These known values are the initial conditions, or the known displacements at time zero; and the boundary conditions that are known displacement values at certain nodes such as the edges of the structure. Once the displacement values at the nodes (DOF) are known, the interpolation equations are used to obtain the displacements within the elements and throughout the entire system [110, 111].

Static Analysis

In static structural problems, the behavior of the structure under loads (forces) is analyzed in terms of the displacements produced. In order to illustrate the FE method applied to a deformable body, the simple example of a spring fixed at one end is taken as shown in Fig. B.2. In fact, the stretching of a canvas can be modelled as a simple spring.
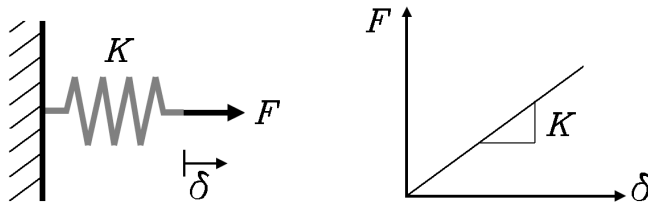
Figure B.2: Spring fixed at one end being stretched by a force applied at the other end.

The spring will have an inherent property called the spring stiffness or the spring constant K. If a force F is applied to the free end, the spring will deform a distance δ out of its equilibrium position. The displacement δ is directly proportional to the force F, given by a relation known as Hooke's law of elasticity.

$$K\delta = F \tag{B.1}$$

In analogy to the spring system, a canvas is stretched by first fixing it to one side of the frame and then applying a force to the other end. The

deformation of the canvas will depend on its stiffness (E modulus) similarly to the spring constant.

Assuming that the canvas is formed by a large assembly of connected elements as shown in Fig. B.1, the displacements in the canvas caused by applied forces can be determined with the governing equations in linear static analysis. These equations can be written in matrix form as

$$[K]\{\delta\} = \{F\} \tag{B.2}$$

where $[K]$ is the assembled global stiffness matrix that relates the nodal displacement vector $\{\delta\} = \{\delta_1, \delta_2, \ldots, \delta_n\}$ to a nodal force vector $\{F\} = \{F_1, F_2, \ldots, Fn\}$. Note the similarity between Eq. B.1 and Eq. B.2. However, the extensive calculations needed to solve the system of equations in Eq. B.2 require the aid of computers with high-speed processing power.

Dynamic Analysis

In dynamic analysis the elastic, damping and inertia properties of the system are considered. The simple example of a spring-mass-damper system is now considered for illustration as shown in Fig. B.3 where M is the mass of the object, K is the stiffness of the spring and C is the damping coefficient.
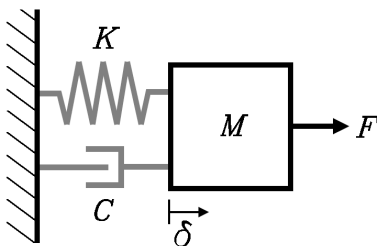
Figure B.3: Spring-mass-damper system

From dynamic equilibrium the governing equation for the system is given by

$$M\ddot{\delta} + C\dot{\delta} + K\delta = F \tag{B.3}$$

where $\dot{\delta}$ denotes the time derivative of the displacement (velocity) and $\ddot{\delta}$ denotes the second time derivative of the displacement (acceleration). Dividing the expression by the mass M yields

$$\ddot{\delta} + 2\zeta\omega\dot{\delta} + \omega^2\delta = F/M \tag{B.4}$$

where $\omega = \sqrt{K/M}$ is the natural frequency (eigenfrequency) of the system, and $\zeta = C/(2m\omega) = C/(2\sqrt{KM})$ is called the damping ratio [112].

Similar to Eq. B.3, the discretized set of equations describing the dynamics of a structure for the FE method is

$$[M]\{\ddot{\delta}\} + [C]\{\dot{\delta}\} + [K]\{\delta\} = \{F\} \tag{B.5}$$

where [M], [C] and [K] are the mass, damping and stiffness matrices. {F} is the vector of externally applied time-dependent nodal loads. The vectors $\{\delta\}$, $\{\dot{\delta}\}$ and $\{\ddot{\delta}\}$ are the time-dependent nodal displacements, velocities and accelerations of the FE model [113].

Free Vibration

Considering the case when no external forces are applied to the structure and assuming that there is no damping, Eq. B.5 reduces to the free vibration problem

$$[M]\{\ddot{\delta}\} + [K]\{\delta\} = 0 \tag{B.6}$$

Assume a non-trivial solution ($\{\delta\} \neq 0$) of the form

$$\{\delta\} = \{\Phi\}e^{i\omega t} \tag{B.7}$$

where $\{\Phi\}$ is a vector of scaled amplitudes for each DOF that gives the eigenshape (mode shape), ω is the eigenfrequency (natural frequency) and t is time. Differentiation of Eq. B.7 and substitution in Eq. B.6 yields the so-called eigenvalue problem

$$[K]\{\Phi\} = \omega^2[M]\{\Phi\} \tag{B.8}$$

Solving the homogeneous linear system gives a set of eigenvalues (squared natural frequencies) $0 \leq \omega_1^2 \leq \omega_2^2 \leq \ldots \leq \omega_n^2$ and the corresponding set of orthogonal eigenvectors $\{\Phi\}_1, \{\Phi\}_2, \ldots, \{\Phi\}_n$ for an n-DOF system [114, 115].

Forced Vibration (Mode Superposition)

The dynamic response of a discrete system can be represented by a superposition of its eigenmodes. Therefore, the solution of the eigenvalue problem is required for mode superposition analysis. Assuming that no damping is present, the dynamic equation governing a system subjected to external time-dependent forces $F(t)$ is

$$[M]\{\ddot{\delta}\} + [K]\{\delta\} = \{F\}(t) \tag{B.9}$$

Since the vibration modes are a set of orthogonal vectors, any arbitrary vector can be represented by a linear combination of the eigenmodes. Therefore, the response of an n-DOF structure can be expressed as

$$\{\delta\}(t) = \sum_{s=1}^{n} \eta_s(t)\{\Phi\}_{(s)} \tag{B.10}$$

where $\eta_s(t)$ are the time-dependent amplitudes of the modal components. Eq. B.10 is differentiated and substituted into Eq. B.9. The resulting equation is then pre-multiplied by the transpose of each eigenvector to project the equilibrium equations into the modal directions. Due to the orthogonality of eigenmodes, a set of uncoupled equations is obtained for the modal amplitudes

$$\ddot{\eta}_r(t) + \omega_r^2 \eta_r(t) = N_r(t) \qquad r = 1, 2, \ldots, n \tag{B.11}$$

where $N_r(t)$ is a generalized force describing the modal participation factor to the loading. These equations have the same form as a single-DOF system. Thus, similarly to Eq. B.4, adding damping to Eq. B.11 yields

$$\ddot{\eta}_r(t) + 2\zeta_r\omega_r\dot{\eta}_r(t) + \omega_r^2\eta_r(t) = N_r(t) \qquad r = 1, 2, \ldots, n \tag{B.12}$$

where ζ_r is the modal damping factor for the corresponding modes, as defined for the single-DOF system from Eq. B.4 [116].

It should be noted that the solution of the eigenvalue problem itself is computationally expensive. Therefore, for models with a large number of degrees of freedom, the computation of all eigenmodes in order to apply mode superposition is not efficient. A practical solution, so called *modal displacement method*, is to neglect higher modes and compute the approximate dynamic response by the superposition of a 'truncated' set of lower eigenmodes. Thus

Eq. B.10 can be expressed in terms of a smaller number $\hat{N}$ of modes in the system:

$$\{\delta\}(t) = \sum_{s=1}^{\hat{N}} \eta_s(t)\{\Phi\}_{(s)} \tag{B.13}$$

The modes to be included in the mode superposition should provide a good representation of the dominant response of the structure. In other words, the omitted eigenmodes should only be slightly excited and therefore could be neglected [117].

Sensitivity of Eigenfrequencies

A sensitivity analysis is performed in order to obtain quantitative information about the sensitivity of eigenfrequencies to a change in the model parameters. A change in the model parameters will produce a change in the eigensolution such that Eq. B.8 remains satisfied. By differentiating Eq. B.8 with respect to a parameter p and rearrangement yields the eigenfrequency sensitivity

$$\frac{\partial \omega_s^2}{\partial p} = \frac{\{\Phi\}_s^T \left([K]^* - \omega_s^2[M]^*\right) \{\Phi\}_s}{\{\Phi\}_s^T [M]\{\Phi\}_s} \tag{B.14}$$

where $[K]^*$ and $[M]^*$ are the sensitivity stiffness and mass matrices respectively, given by

$$[K]^* = \frac{\partial [K]}{\partial p} \qquad\qquad [M]^* = \frac{\partial [M]}{\partial p} \tag{B.15}$$

Appendix C

Convergence Analysis

The FE method is a numerical method used to find approximate solutions to complicated mathematical models. The FE model developed in Section 3.3 is only an approximation for the solution of the vibration of the plate considered to model a canvas painting. Therefore, it is important to determine the error of the FE approximation with respect to the analytical solution of the mathematical model derived in Section 3.1. A convergence analysis is used to determine if the approximate solution approaches (converges to) the exact solution as the mesh is refined (increase in number of elements and DOF) [118].

The convergence analysis was performed for the free vibration of a simply supported orthotropic plate with a biaxial stretching load such as the one shown in Fig. 3.2. The dimensions of the plate were $a = 400$ [mm] and $b = 400$ [mm], and a biaxial load of $N_x = N_y = 0.1225$ [N/mm] (5 kg) was considered. The material properties for Rijn linen were used, these are the elastic moduli $E_1 = 3302$ [MPa] and $E_2 = 128$ [MPa] for the weft and the warp respectively, the Poisson's ratio $\nu_{12} = -1.015$, the shear modulus $G_{12} = 271$ [MPa], the thickness $h = 0.155$ [mm], and the density $\overline{m} = 275 \times 10^{-12}$ [tonne/mm^2].

The exact values for the fundamental natural frequency were obtained with Eq. A.27 for $m = n = 1$

$$
\begin{aligned}
\omega_1^2 = \frac{\pi^4}{\overline{m}} & \left[D_{11} \left(\frac{1}{a} \right)^4 + 2 \left(D_{12} + 2D_{66} \right) \left(\frac{1}{a} \right)^2 \left(\frac{1}{b} \right)^2 + D_{22} \left(\frac{1}{b} \right)^4 \right] \\
& + \frac{\pi^2}{\overline{m}} \left[N_x \left(\frac{1}{a} \right)^2 + N_y \left(\frac{1}{b} \right)^2 \right]
\end{aligned}
\tag{C.1}
$$

where the bending stiffness coefficients D_{ij} for an orthotropic plate are given

by

$$D_{11} = \frac{E_1 \, h^3}{12(1 - \nu_{12} \, \nu_{21})}$$

$$D_{12} = \frac{\nu_{12} \, E_2 \, h^3}{12(1 - \nu_{12} \, \nu_{21})} = \frac{\nu_{21} \, E_1 \, h^3}{12(1 - \nu_{12} \, \nu_{21})}$$

$$D_{22} = \frac{E_2 \, h^3}{12(1 - \nu_{12} \, \nu_{21})}$$ (C.2)

$$D_{66} = \frac{G_{12} \, h^3}{12}$$

Table C.1 shows the FE fundamental frequencies obtained for a progressive mesh refinement starting with 2^2 elements per edge and then duplicating the number (half the size) up to 2^7 elements per edge. The exact value calculated analytically with Eqs. C.1 and C.2 is given at the bottom of the table. The absolute error between each one of the progressively refined FE frequencies and the exact value is given in the third column in Table C.1. It can be observed that when the number of elements is doubled, the error reduces approximately by a factor of 4. This means that the FE solution converges to the exact value with a quadratic order.

Table C.1: Absolute error between the FE and exact fundamental frequency

Elements per Edge	f_1 [Hz]	$|f_1 - f_{1exact}|$ [Hz]
2^2	38.2817	0.9652
2^3	37.5564	0.2399
2^4	37.3761	0.0596
2^5	37.3311	0.0146
2^6	37.3198	0.0033
2^7	37.3170	0.0005
f_{1exact}	37.3165	—

The numerical and exact values of the fundamental natural frequency are plotted in Fig. C.1 together with the computational time against the number of elements for illustration. Note that an optimal number of approximately 40 elements per edge are necessary for an accurate approximation balanced with an efficient computational time. A higher number of elements would increase the computational time and would not result in a significant increase in accuracy for the FE frequency values.
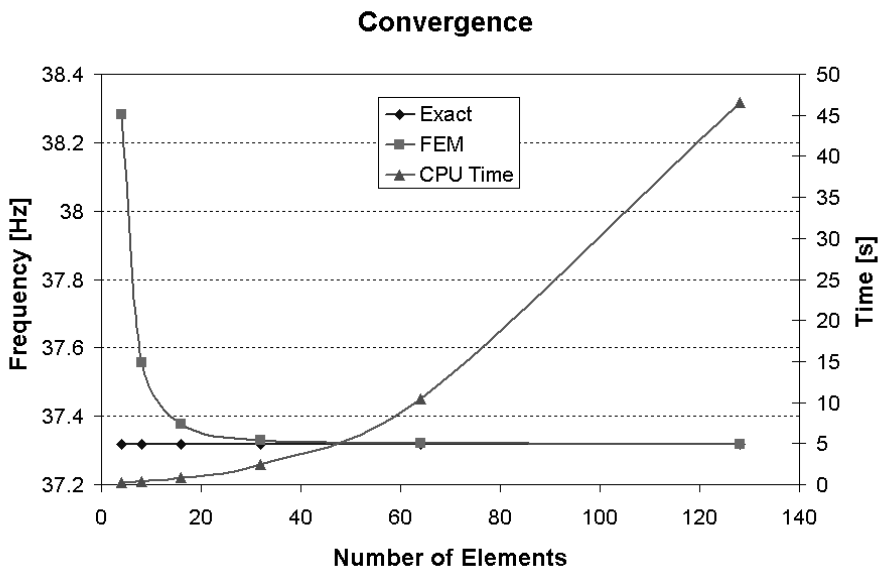
Figure C.1: Numerical and exact values of the fundamental natural frequency and computational time for increasing number of elements per edge.

Appendix D

Thin Film Tensile Testing

Tensile testing was performed on thin film samples in order to measure the elastic moduli of the materials that form the ground layers of the selected prepared canvas specimens. The reasons for the selection and factory properties of the prepared specimens for modelling and testing can be found in Section 4.2 of Chapter 4, Experimental Procedures. The ground is formed by a layer of PVA glue (Polyvinyl alcohol glue), a layer of Zinc White Primer and a final layer of Titanium White Paint. The materials were provided by Classens SA in Waregem Belgium, the manufacturer of the selected prepared and unprepared canvas textiles.

The thin film samples were cast using molds consisting of a Teflon based sheet in order to easily detach the films once they are dry, see Fig. D.1. Adhesive tape was used as guides and borders to form thin film strip molds with a width of 5 mm as shown schematically in Fig. D.1a. Each one of the ground materials was poured in liquid state into the molds and then spread out using a blade and the tape guides to produce uniform thickness films. The strips were dried at room temperature for 10 days. Once dry, the adhesive tape was carefully removed from the Teflon sheet leaving only the strips as shown in Fig. D.1b.

In order to investigate the change in stiffness due to the aging of the films, several moulds were artificially aged in an Atlas Xenotest weathering machine available at the ICN (now RCE). In this machine the specimens were exposed to a xenon arc lamp which ages them at a rate of approximately one fourth of a museum year[1](520 hours) for every hour in the test machine. The specimens were tested at simulated periods of 0, 75, 150 and 225 years.

---

[1]A museum year is defined as the time in which the museums are open to the public in a year (8 hours a day, 5 days a week, 52 weeks a year equal 2080 hours a year).
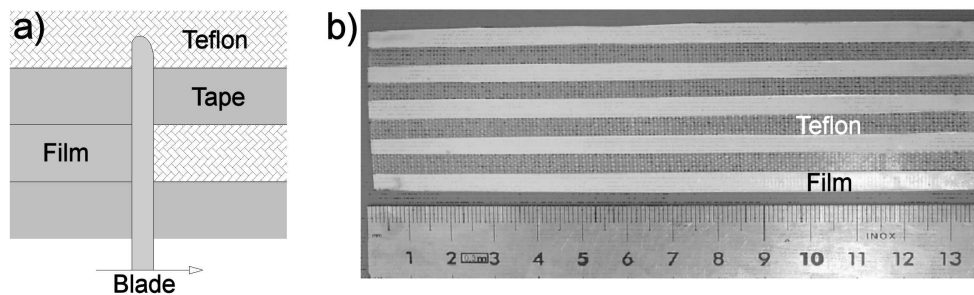
Figure D.1: a) Scheme of thin film casting. b) Photograph of dry films on Teflon sheet.
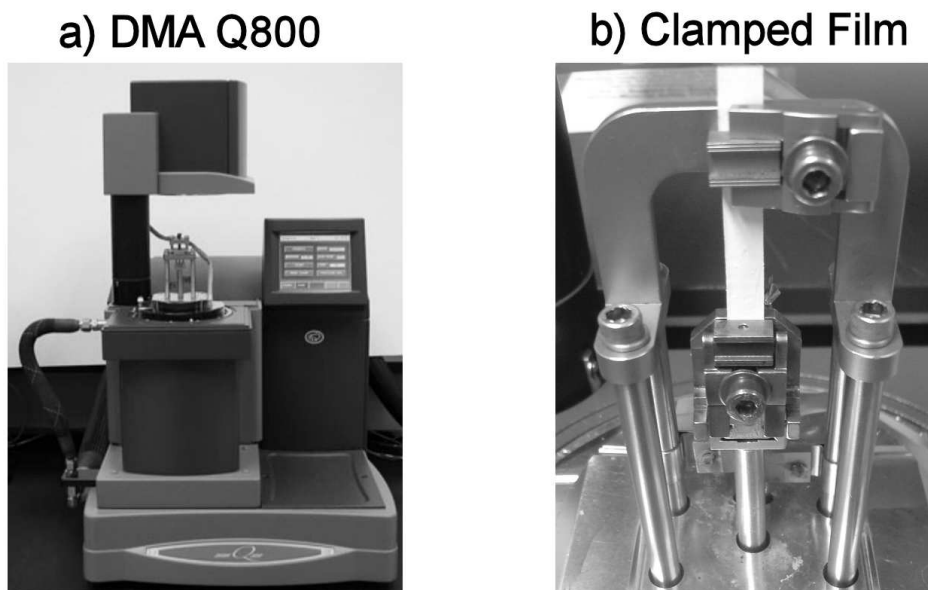

Figure D.2: a) DMA (Dynamic Mechanical Analyzer) Q800. b) Photograph of clamped thin film.

Tensile testing was carried out at the Department of Precision and Microsystems Engineering at the faculty of Mechanical, Maritime and Materials Engineering at the TU Delft. The machine used was a DMA Q800 (Dynamic Mechanical Analyzer) Machine manufactured by TA Instruments (see Fig. D.2a). The thin film strips were carefully removed from the Teflon based sheet and then cut into approximately 40 mm long specimens. Measurements of the width and the thickness of the specimens were taken in order to determine the cross-section area to calculate the stresses. The specimens were mounted on the DMA Machine as shown in Fig. D.2b with an effective length of approximately 20 mm between the clamps. Tensile testing was performed at a strain rate of 3 %/min and a preload of 0.01 N.

Table D.1 and Fig D.3 show the measured elastic moduli for the materials that form the ground layers for the each aging period. The Zn Primer has the highest stiffness and the PVA glue has the lowest one. Note that in general the fresh films have a low E modulus and the stiffness increases with age with the highest aging rate occurring between 75 and 150 years. After 150 years PVA glue appears to age at the same rate while for the Zn Primer the rate decreases significantly. For the Ti Paint the stiffness at 225 years is significantly lower that the stiffness at 150 years. This can be explained because at a certain point the paint film becomes very brittle and starts falling apart.

Table D.1: Elastic moduli of grounds as a function of aging time.

Age	0 Years		75 Years		150 Years		225 Years	
Material	E_g [MPa]	SD	E_g [MPa]	SD	E_g [MPa]	SD	E_g [MPa]	SD
PVA Glue	50	30	140	50	970	225	1840	220
Zn Primer	120	25	310	40	1270	320	1310	295
Ti Paint	70	40	180	60	960	260	260	130
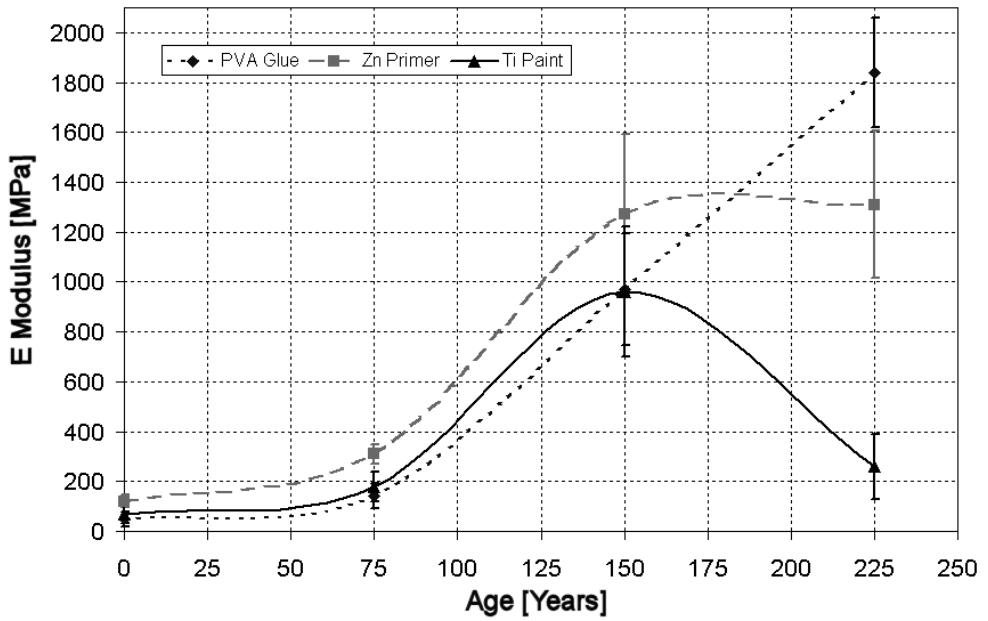
Figure D.3: Elastic moduli of grounds as a function of aging time

Appendix E

Design of the Biaxial Stretcher

In this appendix the design considerations for the basic components of the biaxial stretcher are presented: the support frame, the power screws and the load cells. The support frame bears the load produced when the specimen is stretched; this load is applied with power screws that move the specimen clamps and it can be measured with the load cells.

Support Frame

The support frame consists of a 1200 x 1200 mm square structure. The frame dimensions were determined by taking into account the specimen and clamp lengths plus the displacement stroke of the clamps and enough free space for mounting parts and specimens. The design calculations are done by considering one of the sides of the frame as a beam with fixed edges with a center point load applied when the specimen is stretched (see Fig. E.1a). The edges are assumed fixed because the beam would be welded to the other sides of the frame. The deflection of the beam should be minimized so that the deformation occurs mainly in the specimen. Thus, the maximum deflection of the beam at the center is considered as the design criterion.

The case of a beam with fixed edges and a central load is well known. The maximum deflection occurs at the center of the beam and the value is given by

$$Y_{max} = -\frac{F\,L^3}{192\,E\,I} \qquad (\text{E.1})$$
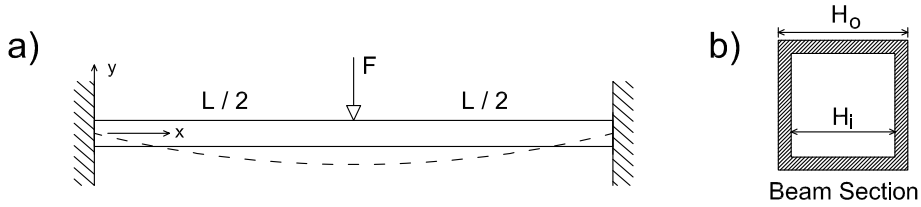
Figure E.1: a) Beam with fixed edges and a center load for the design of one of the sides of the frame. b) Square tube beam section.

Considering that for the maximum test load of 196 N (20 kg) the strain in a 400 mm long specimen is approximately 0.001, a permissible difference in strain of one tenth of that value (0.0001) due to deflection of the beam is assumed. This strain difference would correspond to a maximum deflection of the beam of 0.04 mm for a 400 mm long specimen.

Replacing the maximum deflection Y_{max}=0.04 mm, the length of the beam L=1200 mm, the test load F=196 N on Eq. E.1 and considering the elastic modulus of steel of $E = 200000$ MPa yields the required moment of inertia for the beam

$$I = -\frac{F\,L^3}{192\,E\,Y_{max}} = -\frac{(196)\,(1200)^3}{192\,(200000)\,(-0.04)} = 220500\,mm^4 \qquad (E.2)$$

A safety factor of 1.5 is assumed which yields a moment of inertia of $I = 330750$ mm^4. Based on this value, a conservative square tube section (Fig. E.1b) of 60 x 60 x 3 mm was selected. The square tube section was chosen for its geometrical stiffness, low weight and ease of fabrication. The corresponding moment of inertia of the section was calculated by

$$I = \frac{H_o^4 - H_i^4}{12} = \frac{(60)^4 - (54)^4}{12} = 371412\,mm^4 \qquad (E.3)$$

which is conservative and satisfies the required value determined previously. Replacing the moment of inertia of the selected section in Eq. E.1 yields

$$Y_{max} = -\frac{F\,L^3}{192\,E\,I} = -\frac{(196)\,(1200)^3}{192\,(200000)\,371412} = -0.024\,mm \qquad (E.4)$$

This deflection would result on a difference in strain of 0.00006 in a 400 mm long specimen, which is only one sixteenth of the strain in the specimen

(0.001) at a load of 196 N. Additionally, the entire support frame was simulated by finite element analysis. Beam elements were used with a central point load (196 N) as it is rendered on Fig. E.2a. The beams have rigid connections at the corners to simulate welded joints. The resulting deflections at the mid points of the beams have a maximum value of 0.025 mm in agreement with the analytical values from Eq. E.4.
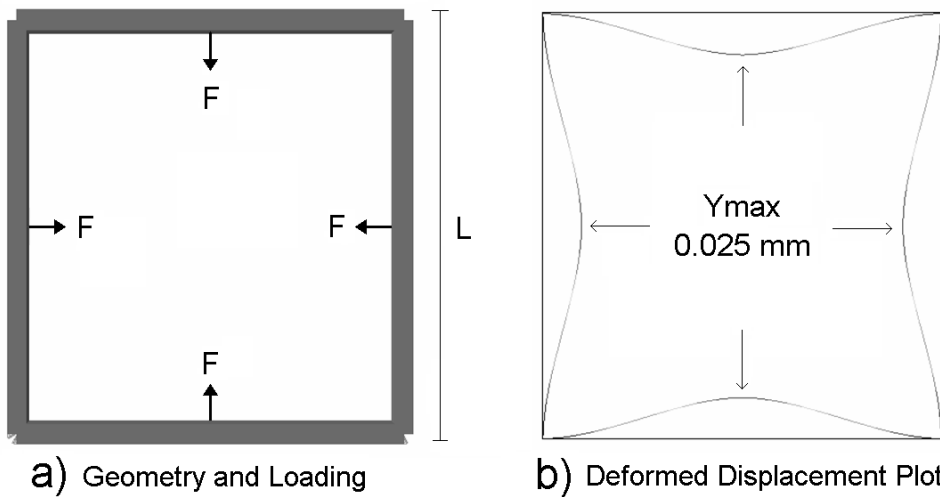

Figure E.2: Finite element analysis of the support frame. a) Geometry and loading; b) Deformed displacement plot.

Power Screws

This section presents the design considerations for the selection of the power screws used to tension the canvas specimens. A portion of one of the screws as it is mounted against the support frame is shown in Fig. E.3. By tightening the nut the angular motion is changed into a linear motion of the screw which displaces the specimen clamps. The design considerations used for the selection of the power screws can be found on Shigley's book on Mechanical Engineering Design [119].

The selection of the power screws was performed by an iterative procedure based on mathematical expressions found in [119]. The equations and the iterations were processed in a Matlab code. The corresponding calculations for the selected section are given below as an example.

A standard fine pitch metric screw M8 x 1 was selected after the iteration process. This type of screw was chosen considering that the power require-
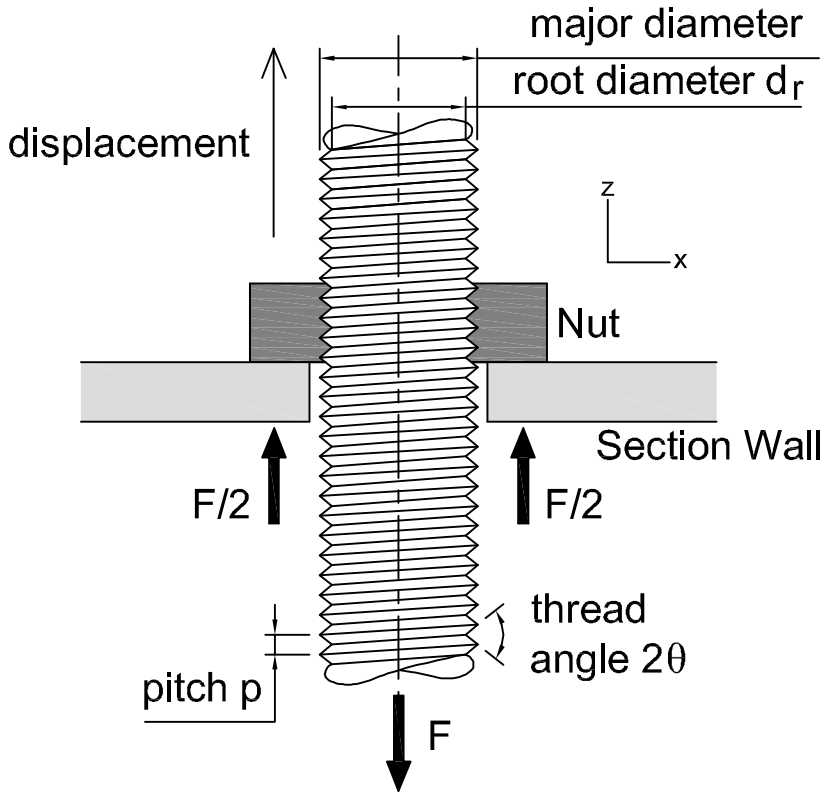
Figure E.3: Detail of power screw.

ments are low for this case and a 1 mm pitch implies that one turn of the nut corresponds to a 1 mm displacement of the screw. The root and mean diameters for this screw are $d_r = 6.7731$ mm and $d_m = 7.3505$ mm respectively. A conservative design load of F = 1000 N ($\approx$102 Kg) is assumed. (see Section 4.3). First the torque required to apply the design load of is calculated with

$$T = \frac{Fd_m}{2} \left(\frac{l + \pi\mu d_m sec\,\theta}{\pi d_m - \mu l sec\,\theta} \right) \tag{E.5}$$

In this case, the lead l is equal to the pitch $p = 1$ mm because the screw has a single thread. The thread angle for metric threads is $2\theta = 60°$, and a friction coefficient of $\mu = 0.15$ for oiled steel against steel is assumed. Replacing these values in Eq. E.5 yields

$$T = \frac{1000(7.35)}{2} \left(\frac{1 + \pi(0.15)(7.35)sec\,30°}{\pi(7.35) - (0.15)(1)sec\,30°} \right) = 801.74\,N\,mm \tag{E.6}$$

The torque is used to calculate the maximum nominal shear stress in torsion of the screw body with the following equation:

$$\tau_{yz} = \frac{16T}{\pi d_r^3} = \frac{16(801.74)}{\pi(6.77)^3} = 13.14\,MPa \tag{E.7}$$

The axial stress in the body of the screw due to the force F is

$$\sigma_z = \frac{F}{A} = \frac{4F}{\pi d_r^2} = \frac{4(-1000)}{\pi(6.77)^2} = -27.75\,MPa \tag{E.8}$$

Additionally, there are bending stresses at the root of the threads. Assuming that the number of engaged threads is n_t=3, the stresses are calculated with

$$\sigma_x = \frac{6F}{\pi d_r n_t p} = \frac{6(1000)}{\pi(6.77)(3)(1)} = 94\,MPa \tag{E.9}$$

The von Mises stress at the top of the root is given by

$$\sigma' = \frac{1}{\sqrt{2}} \left[(\sigma_x - \sigma_y)^2 + (\sigma_y - \sigma_z)^2 + (\sigma_z - \sigma_x)^2 + 6(\tau_{xy}^2 + \tau_{yz}^2 + \tau_{zx}^2) \right]^{1/2} \tag{E.10}$$

Replacing the previously calculated stress values yields

$$\sigma' = \frac{1}{\sqrt{2}} \left[(94)^2 + (27.75)^2 + (-27.75 - 94)^2 + 6(13.14)^2 \right]^{1/2} = 112.83 \ MPa \tag{E.11}$$

Considering that the yield strength of structural steel is S_y=250 MPa the safety factor is

$$SF = \frac{S_y}{\sigma'} = \frac{250}{112.83} = 2.2 \tag{E.12}$$

Load Cells

Bending beam type load cells were used to measure the force applied to the specimen. One end of the beam was attached to the support frame and the other end was loaded with the force applied by tightening the power screw nut as shown in Fig E.4a. The beam has two holes in the shape of binoculars which allow tension and compression on the same surface of the beam. Strain gauges are bonded to the upper and lower part of this region at the points with maximum strain. The strain gauges are basically conductors that will vary in resistance as they are stretched or compressed when the beam is bent. The change in electrical resistance in the strain gauges is measured using a full Wheatstone bridge in which the four resistances can be variable.
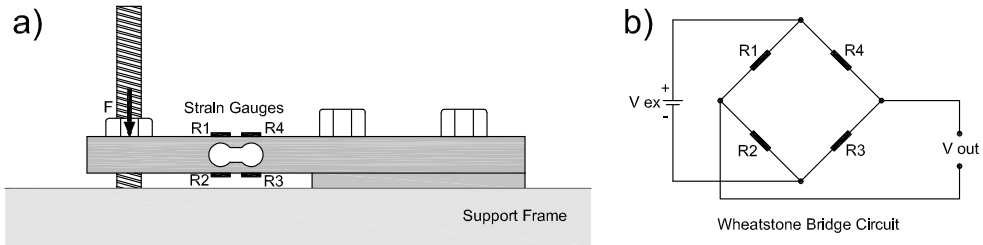
Figure E.4: a) Bending beam load cell and b) Wheatstone bridge circuit.

The circuit of the Wheatstone bridge is shown on Fig. E.4b. The external and output voltages (V_{ex} and V_{out}) are applied and measured respectively with a multichannel compact amplifier model PICAS manufactured by Peekel Instruments B.V. The bridge is said to be balanced in the unloaded state. When the beam is bent the two strain gauges in tension R2, R4 increase in resistance while gauges R1, R3 in compression decrease in resistance, producing an imbalance in the bridge and a change in output voltage proportional

to the load in the range of mV. Prior to being mounted, the load cells were calibrated with weights so that a weight of 1 kg produces an output voltage of 1 mV.

# Appendix F

Canvas Relaxation Tests

The relaxation of the canvas was investigated by performing tests in which the canvas was loaded biaxially up to a certain load and then several measurements of the load were taken as it relaxed in time. Rijn linen canvas was used for the relaxation tests with the same cruciform geometry (40 x 40 mm) as the ones used for vibration testing (see Section 4.2).

The results of the relaxation test are shown in Fig. F.1. The specimen was loaded biaxially with 5, 10 and 20 kg (Fig. F.1 a,b,c respectively), and the reduction in load was recorded for the weft and warp directions during a period of 20 minutes. It can be observed that the warp direction relaxes considerably more that the weft direction due to amount of crimp present in the warp. It can also be observed that the higher the load, the greater the decrease in load, however in percentage the relaxation is similar for all loads. Additionally the load was monitored after 24 hours of stretching it with 20 kg and it was observed that the load in both directions continued to relax gradually up to 9 % in the weft direction and 15 % in the warp direction.

In order to minimize the relaxation of the canvas during the vibration testing, the canvas was re-stretched repetitively for three times up to the desired load before carrying out the vibration test. The canvas relaxation with re-stretching was investigated with similar tests as the ones described previously and the behavior is shown in Fig. F.2.

The percentage relaxation after 20 minutes for a canvas which has been stretched only once and a canvas which has been stretched 3 times is given in Table F.1 for comparison. Note that the relaxation is minimized considerably for the warp direction when it is repeatedly stretched, however for the weft directions the values remain practically the same. Furthermore, the loads were monitored for the following 24 hours and it was observed that the canvas

c) 20 kg Applied Biaxial Load
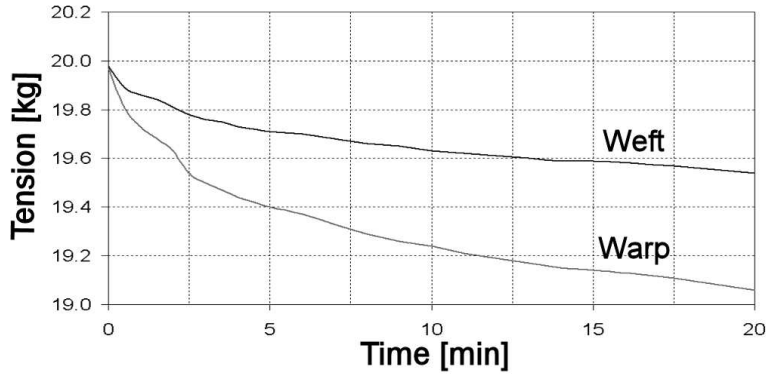
b) 10 kg Applied Biaxial Load
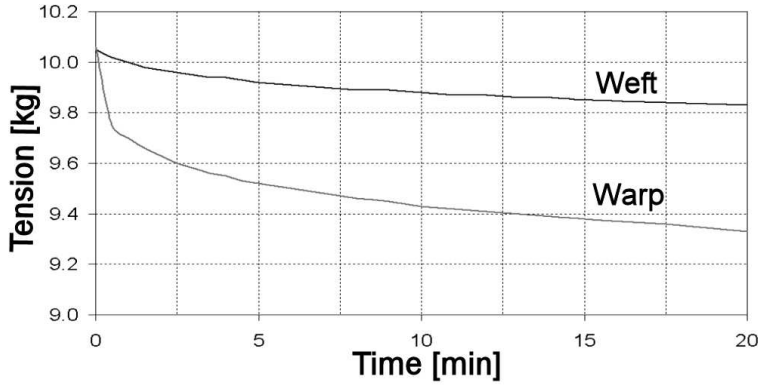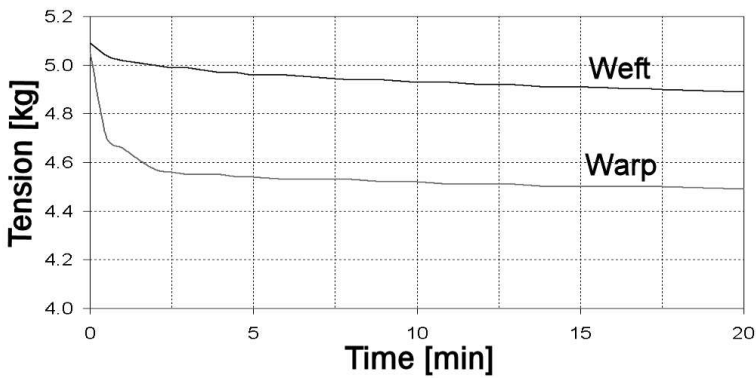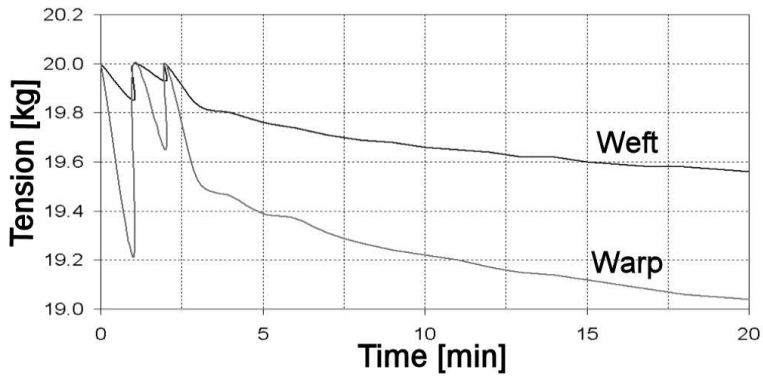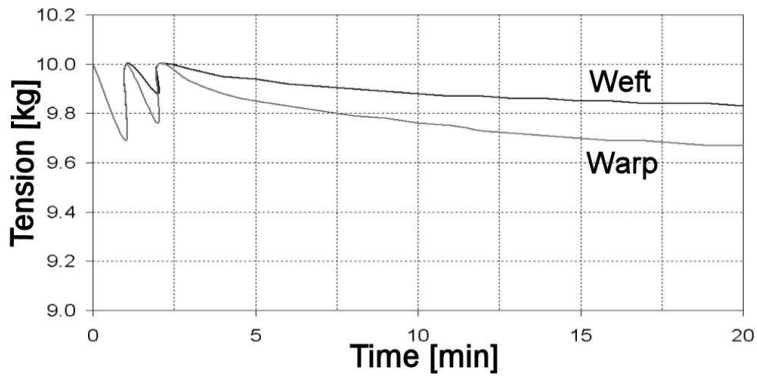
a) 5 kg Applied Biaxial Load

Figure F.1: Rijn linen relaxation measurements after stretching once.

c) 20 kg Applied Biaxial Load

b) 10 kg Applied Biaxial Load

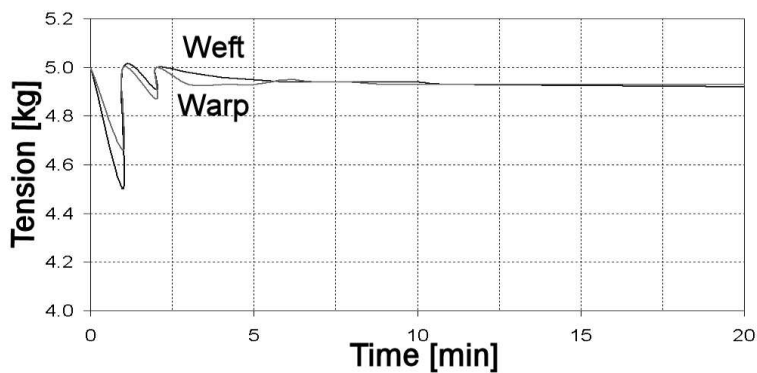## a) 5 kg Applied Biaxial Load

Figure F.2: Rijn linen relaxation measurements after stretching three times.

relaxed continuously in an asymptotic way. Therefore, the rate at which it relaxed decreased significantly over time.

Table F.1: Percentage relaxation of canvas after 20 minutes

Load	Stretching	Once	3 Times
5 kg	Weft	4 %	2 %
	Warp	11 %	1 %
10 kg	Weft	2 %	2 %
	Warp	7 %	3 %
20 kg	Weft	2 %	2 %
	Warp	5 %	5 %

In reality, artists stretch a canvas repeatedly and they wet the canvas in between each stretching process. In order to investigate the effect of water on the canvas textile, a canvas sample was stretched up to a 20 kg load and then the canvas was sprinkled with water while the load was measured in the weft and warp directions. The results show that there is a considerable increase in load for the weft direction after wetting (190 %), while for the warp direction the increase in load is about one third (65 %) of the increase for the weft. It can be observed that after half hour the load in the warp direction returned to the original load applied.
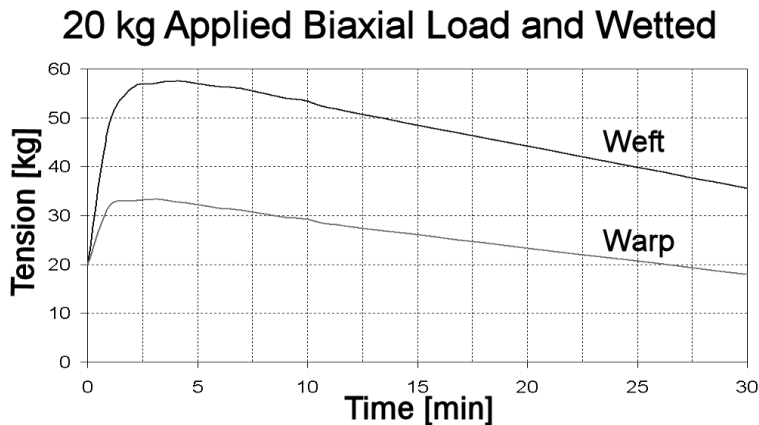
Figure F.3: Rijn linen relaxation measurements after wetting.

Appendix G

Mode Shape Derivatives

This appendix shows the derivation with respect to the x and y directions of mode shape functions of the form

$$\Phi(x, y) = \sin\left(\frac{m\pi x}{a}\right)\sin\left(\frac{n\pi y}{b}\right) \tag{G.1}$$

where m and n are the wave numbers in the x and y directions respectively. The derivatives were obtained numerically with Matlab and are plotted with their corresponding mode shape in Figs. G.1 and G.2. These mode shape derivatives were used as a reference to compare the FE mode shapes given as out-of-plane displacements, with the measured mode shapes with laser shearography which are given as the derivatives of the out-of-plane displacements.
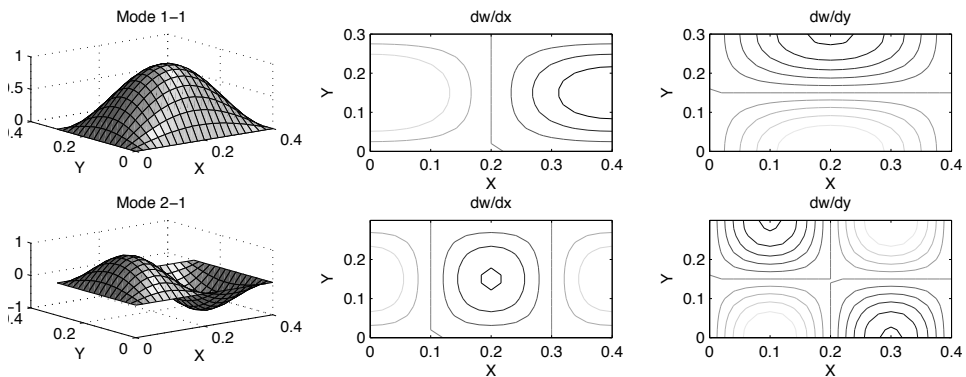
Figure G.1: Mode shapes and derivatives with respect to x and y directions for the first two modes.
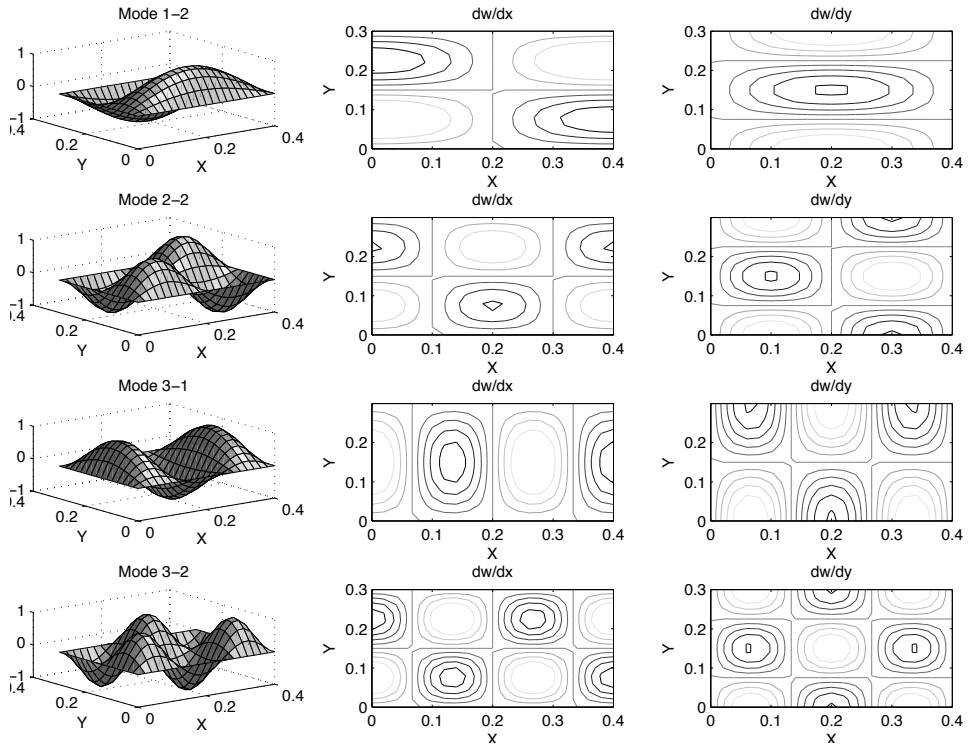
Figure G.2: Mode shapes and derivatives with respect to x and y directions for higher modes.

Literature

[1] Rexart. http://www.rexart.com/stretching.html, Accessed 10/08/10.

[2] L. W. McKeen, *Fluorinated Coatings and Finishes Handbook*, p. 200. New York: William Andrew Publishing, 2006.

[3] I. V. Mullova, "Craquelures." http://www.shutterstock.com, Accessed 02/11/10.

[4] "Mona lisa detail eyes." http://commons.wikimedia.org, Accessed 02/11/10.

[5] M. Kimmelman, "Art view; an antidote to the blockbuster syndrome," *The New York Times*, March 1991.

[6] M. Doerner, *Los Materiales de Pintura y su Empleo en el Arte*, p. 121. Barcelona: Editorial Reverte S.A, sexta ed., 1998.

[7] R. Gettens and G. Stout, *Painting Materials: A Short Encyclopedia*, p. 228. New York: Dover Publications Inc., 1966.

[8] Museum of Fine Arts, *Conservation and Art Materials Encyclopedia Online (CAMEO)*, (Boston), 2000. http://cameo.mfa.org.

[9] R. Horrocks and S. Anand, *Handbook of Technical Textiles*, p. 78. Abington: Woodhead Publishing, 2004.

[10] M. Doerner. op. cit., p. 123.

[11] M. Doerner, *The Materials of the Artist and Their Use in Painting*, p. 3. New York: Harcourt Inc., first harvest ed., 1984.

[12] R. Horrocks and S. Anand. op. cit., p. 63.

[13] M. Doerner. op. cit., p. 158.

[14] D. Graves, *Figure Painting in Oil*, p. 15. New York: Dover Publications Inc., 1973.

[15] L. Lamb, *Preparation for Painting: The Purpose and Materials of the Artist*, pp. 118–119. London: Oxford University Press, 1954.

[16] M. Doerner. op. cit., p. 45.

[17] I. Giakoumis, N. Nikolaidis, and I. Pitas, "Digital image processing techniques for the detection and removal of cracks in digitized paintings," *IEEE Transactions on Image Processing*, vol. 15, pp. 178–188, January 2006.

[18] D. Pinna, M. Galeotti, and R. Mazzeo, *Scientific Examination for the Investigation of Paintings: A Handbook for Conservator-Restorers*, p. 16. Firenze: Centro Di, 2011.

[19] M. F. Mecklenburg and C. S. Tumosa, "Mechanical behavior of paintings subjected to changes in temperature and relative humidity," in *Art in Transit: Studies in the Transport of Paintings*, (Washington, DC), pp. 173–216, National Gallery of Art, 1991.

[20] C. Young and P. Ackroyd, "The mechanical behaviour and environmental response of paintings to three types of lining treatment," *The National Gallery Technical Bulletin*, vol. 22, pp. 85–104, January 2001.

[21] T. Bilson, "Canvas shrinkage: a preliminary investigation into the response of a woven structure," in *ICOM committee for conservation, 11th triennial meeting in Edinburgh, Scotland, 1-6 September 1996: Preprints*, (London), pp. 245–252, 1996.

[22] G. A. Berger and W. H. Russell, "Interaction between canvas and paint film in response to environmental changes," *Studies in Conservation*, vol. 39, pp. 73–86, May 1994.

[23] A. Karpowicz, "A study on development of cracks on paintings," *Journal of the American Institute for Conservation*, vol. 29, pp. 169–180, Autumn 1990.

[24] M. F. Mecklenburg, "Some aspects of the mechanical behavior of fabric supported paintings," *Report to the Smithsonian Institution*, 1982.

[25] G. A. Berger and W. H. Russell, "Investigations into the reactions of plastic materials to environmental changes. part i. the mechanics of the decay of paint films," *Studies in Conservation*, vol. 31, pp. 73–86, May 1986.

[26] C. Young, "Interfacial interactions of modern paint layers," *Modern Paints Uncovered*, pp. 247–256, 2007.

[27] N. Stolow, *Procedures and conservation standards for museum collections in transit and on exhibition.* UNESCO, Paris, 1981.

[28] M. F. Mecklenburg, "Art in transit: studies in the transport of paintings," in *International Conference on the Packing and Transportation of Paintings*, (London), National Gallery of Art, September 1991.

[29] P. J. Marcon, "Shock, vibration, and protective package design," in *Art in transit: studies in the transport of paintings*, (Washington DC.), pp. 107–120, National Gallery of Art, 1991.

[30] P. Caldicott, "Vibration and shock in transit situation: a practical evaluation using random vibration techniques," in *Art in transit : studies in the transport of paintings*, (Washington DC.), pp. 343–344, National Gallery of Art, 1991.

[31] D. Saunders, "Monitoring shock and vibration during the transportation of paintings," *National Gallery Technical Bulletin*, vol. 19, pp. 64–73, 1998.

[32] D. Thickett, "Vibration damage levels for museum objects," *ICOM Committee for Conservation, ICOM-CC : 13th Triennial Meeting, Rio de Janeiro: preprints*, vol. 1, pp. 90–95, 22-27 September 2002.

[33] N. Kamba, H. Wada, M. Tsukada, Y. Takagi, and K. Imakita, "Measurement and analysis of the global transport environment for packing cases for artifacts," *IIC International Institute for conservation of Historic and Artistic Works, Contributions to the London Congress*, pp. 90–95, 15-19 September 2008.

[34] D. Saunders, "The effect of painting orientation during air transportation," *ICOM Committee for Conservation, 14th Triennial Meeting, The Hague*, vol. 2, pp. 700–7077, 12-16 September 2005.

[35] T. Green, "Vibration control: Paintings on canvas supports," in *Art in transit : studies in the transport of paintings*, (Washington DC.), pp. 59–67, National Gallery of Art, 1991.

[36] S. Michalski, "Paintings - their response to temperature, relative humidity, shock, and vibration," in *Art in transit: studies in the transport of paintings*, (Washington DC.), pp. 723–248, National Gallery of Art, 1991.

[37] M. Bustin and T. Green, "Tate case specification for a single painting," *Tate Conservation Department*, 2001.

[38] T. Garcia, "Packaging system for paintings, other works of art and the like," *United States Patent*, no. 5285902, 1994.

[39] M. Richard, M. F. Mecklenburg, and R. M. Merrill, "Art in transit, handbook for packing and transporting paintings," 1997.

[40] A. Stephenson-Wright and R. White, "Packing: An updated design, reviewed and tested," *National Gallery Technical Bulletin*, vol. 11, pp. 36–39, 1987.

[41] P. J. Marcon, "Shock, vibration, and the shipping environment," in *Art in transit: studies in the transport of paintings*, (Washington DC.), pp. l2l–132, National Gallery of Art, 1991.

[42] S. Michalski and P. Marcon, *Mechanical risks to large paintings such as Guernica during transit.* Santander: Fundaci6n Marcelino Botin, 2002.

[43] W. Wei, W. Kragt, and A. Visser, "Non-contact measurement of vibrations in paintings using laser doppler vibrometry," in *Proceedings of Art '05 - Non-Destructive Investigations and Microanalysis for the Diagnostics and Conservation of the Cultural and Environmental Heritage*, (Lecce (Italy)), pp. 15–19, 15-19 May 2005.

[44] A. Johnson and A. Akbar, "Rock concerts 'add years' to artworks," *The Independent*, June 2008.

[45] K. H. Ian Gibb, Adrian Phillips and K. Frame, "Shake, rattle and roll: vibration effects at the Hampton Court Music Festival," *Conservation Science*, 2007.

[46] M. F. Mecklenburg and C. S. Tumosa, "An introduction into the mechanical behavior of paintings under rapid loading conditions," in *Art in Transit: Studies in the Transport of Paintings*, (Washington, DC), pp. 137–170, National Gallery of Art, 1991.

[47] W. Wei, "Mechanical aspects of the restoration of the Barnett Newman painting 'Cathedra'," Tech. Rep. 99-014, Netherlands Institute for Cultural Heritage, 2002.

[48] E. Aubry, R. Postle, and M. Renner, "Vibrating properties of textile surfaces," *Textile Research Journal*, vol. 69, pp. 335–338, May 1999.

[49] W. Shanahan, D. Lloyd, and J. Hearle, "Characterizing the elastic behavior of textile fabrics in complex deformations," *Textile Research Journal*, vol. 48, pp. 495–505, September 1978.

[50] J. Zheng, T. Komatsu, M. Takatera1, S. Inui, L. Bao, and Y. Shimizu, "Relationship between uniaxial and strip biaxial tensile properties of fabrics," *Textile Research Journal*, vol. 78, pp. 224–231, March 2008.

[51] V. Quaglini, C. Corazza, and C. Poggi, "Experimental characterization of orthotropic technical textiles under uniaxial and biaxial loading," *Composites*, vol. 39, pp. 1331–1342, February 2007.

[52] M. King, P. Jearabaisilawong, and S. Socrate, "A continuum constitutive model for the mechanical behavior of woven fabrics," *International Journal of Solids and Structures*, vol. 42, pp. 3867–3896, January 2005.

[53] J. Hu and J. Teng, "Computational fabric mechanics: Present status and future trends," *Finite Element Analysis and Design*, vol. 21, pp. 225–237, April 1996.

[54] B. B. Boubaker, B. Haussy, and J.-F. Ganghoffer, "Discrete woven structure model: yarn-on-yarn friction," *Comptes Rendus Mecanique*, vol. 335, pp. 150–158, April 2007.

[55] M. Tarfaoui and S. Akesbi, "A finite element model of mechanical properties of plain weave," *Colloids and Surfaces*, vol. 187, pp. 439–448, 2001.

[56] P. V. Cavallaro, A. M. Sadegh, and C. J. Quigley, "Decrimping behavior of uncoated plain-woven fabrics subjected to combined biaxial tension and shear stresses," *Textile Research Journal*, vol. 77, no. 6, pp. 403–416, 2007.

[57] S. S. Rao, *Vibration of Continous Systems*, p. 4. New Jersey: John Wiley & Sons, 2007.

[58] O. Zienkiewicz and R. Talylor, *The Finite Element Method*, vol. 1, pp. 487–490. Oxford: Butterworth Heinemann, fifth ed., 2000.

[59] O. Zienkiewicz and R. Talylor. op. cit., pp. 1–3.

[60] V. Panc, *Theories of Elastic Plates*, pp. 1–2. Leiden: Noordhoff International Publishing, 1975.

[61] R. M. Jones, *Mechanics of Composite Materials*, pp. 147–155. Tokyo: McGraw-Hill, international student ed., 1975.

[62] D. O. Brush and B. O. Almroth, *Buckling of Bars, Plates and Shells*, pp. 76–80. Tokyo: McGraw-Hill, international student ed., 1975.

[63] M. S. Qatu, *Vibration of Laminated Shells and Plates*, pp. 6–7. Oxford: Elsevier Academic Press, first ed., 2004.

[64] "Imagej." http://rsbweb.nih.gov/ij/index.html, Accessed 14/01/12.

[65] J. Hu, *Structure and mechanics of woven fabrics*, p. 68. Abington: Woodhead Publishing Limited, 2004.

[66] American Society for Testing and Materials, *ASTM Standard D 3883 Standard Test Method for Yarn Crimp or Yarn Takeup in Woven Fabrics*, vol. 7.01, (Philadelphia), 1998.

[67] American Society for Testing and Materials, *ASTM Standard D 1682-64 Standard Test Methods for Breaking Load and Elongation of Textile Fabrics*, vol. 7.01, (Philadelphia), 1998.

[68] G. A. Berger and W. H. Russell, "Deterioration of surfaces exposed to environmental changes," *Journal of the American Institute for Conservation*, vol. 29, pp. 45–76, Spring 1990.

[69] C. Young, "Accelerated ageing of fabric supports: is it possible?," *Scientific analysis of ancient and historic textiles: informing preservation, display and interpretation: postprints, first annual conference*, pp. 111–117, 13-15 July 2004 2004.

[70] D. Carr, C. Young, A. Phenix, and R. Hibberd, "Development of a physical model of a typical nineteenth century english canvas painting," *Studies in Conservation*, October 2003.

[71] J. W. S. Hearl, P. Grosberg, and S. Backer, *Structural Mechanics of Fibers, Yarns, and Fabrics*, vol. 1, pp. 340–342. New York: Wiley-Interscience, 1969.

[72] V. Panc. op. cit., p. 5.

[73] R. J. D. Tilley, *Understanding Solids: The Science of Materials*, pp. 322–323. Chichester: John Wiley & Sons, 2004.

[74] H. J. K. Lemmen, *Fatigue and Damage Tolerance of Friction Stir Welded joints for Aerospace Applications.* PhD thesis, Delft University of Technology, Faculty of Aerospace Engineering, 2011.

[75] R. M. Jones. op. cit., p. 171.

[76] V. Panc. op. cit., pp. 393–405.

[77] R. S. Srinivasan and V. Thiruvenkatachari, "Static and dynamic analysis of stiffened plates," *Computers & Structures*, vol. 21, pp. 395–403, February 1985.

[78] L. P. Kollar and G. S. Springer, *Mechanics of Composite Structures*, pp. 107–112. Cambridge: Cambridge University Press, 2003.

[79] R. M. Jones. op. cit., p. 159.

[80] American Society for Testing and Materials, *ASTM Standard D 1388-96 Standard Test Method for Stiffness of Fabrics*, vol. 7.01, (Philadelphia), 1998.

[81] J. Hol, *Computational Fluid and Solid Mechanics Practical*. Delft: Delft University of Technology, 2007. Work Package 12: Linear Dynamics.

[82] SIMULIA, *Abaqus 6.8 Documentation*. Analysis User's Manual, Linear Elasticity.

[83] K. Jansen. TU Delft: Dep. Precision and Microsystems Engineering, 2009. Private Communication.

[84] D. J. Inman, *Engineering Vibration*, pp. 364–380. New Jersey: Prentice Hall, 1996.

[85] P. Huyvaert. Claessens SA, Waregem, Belgium, 2009. Private Communication.

[86] American Society for Testing and Materials, *ASTM Standard D 1776-90 (Reapproved 1996) Standard Practice for Conditioning Textiles for Testing*, vol. 7.01, (Philadelphia), 1998.

[87] L. Gunawan, *Experimental Study of Nonlinear Vibrations of Thin-walled Cylindrical Shells*. PhD thesis, Delft University of Technology, 1998.

[88] CVI Melles Griot, *Fundamentals of Vibration Isolation*, 2009.

[89] M. Amabili, *Nonlinear Vibrations and Stability of Shells and Plates*, p. 11. New York: Cambridge University Press, 2008.

[90] R. G. Gupta, *Audio and Video Systems: Principles, Maintenance and Troubleshooting*, p. 5. New Delhi: McGraw-Hill, 2010.

[91] SIOS Meβtechnik GmbH, Ilmenau, *Models SP 120/500/2000 Miniature Plane-Mirror Interferometers User's Guide*, 1999.

[92] C. D. Silva, *Vibration Monitoring, Testing, and Instrumentation*, pp. 1–93. Florida: CRC Press, 2007.

[93] W. Steinchen and L. Yang, *Digital Shearography; Theory and Application of Digital Speckle Pattern Shearing Interferometry*, p. 1. Washington: SPIE Press, 2003.

[94] W. Steinchen and L. Yan. op. cit., pp. 30–34.

[95] W. Steinchen and L. Yan. op. cit., pp. 55–57.

[96] W. Steinchen and L. Yan. op. cit., pp. 203–212.

[97] N. M. M. Maya and J. M. M. e Silva, *Theoretical and Experimental Modal Analysis*, p. 97. Somerset: Research Studies Press, 1997.

[98] R. J. Allemang, "The modal assurance criterion - twenty years of use and abuse," *Sound and Vibration*, pp. 14–21, August 2003.

[99] N. M. M. Maya and J. M. M. e Silva. op. cit., p. 350.

[100] R. W. Clough and J. Penzien, *Dynamics of structures*, pp. 69–73. Michigan: McGraw-Hill, 1975.

[101] N. M. M. Maya and J. M. M. e Silva. op. cit., pp. 45–46.

[102] G. A. V. Leaf and A. M. F. Sheta, "The initial shear modulus of plain-woven fabrics," *Journal of The Textile Institute*, pp. 157–163, May 1986.

[103] J. Wu and N. Pan, "Grab and strip tensile strengths for woven fabrics: An experimental verification," *Textile Research Journal*, pp. 789–796, November 2005.

[104] E. Hezavehi, S. S. Najar, P. Zolgharnein, and H. Yahya, "A new electro-mechanical technique for measurement of stress relaxation of polyester blended fabric with constant torsional strain," *International Journal of Clothing Science and Technology*, vol. 23, no. 5, pp. 388–398, 2011.

[105] J. Gersak, D. Sajn, and V. Bukosek, "A study of the relaxation phenomena in the fabrics containing elastane yarns," *International Journal of Clothing Science and Technology*, vol. 17, no. 3, pp. 188–199, 2005.

[106] R. M. Jones. op. cit., pp. 31–47.

[107] M. S. Qatu. op. cit., pp. 121–140.

[108] D. O. Brush and B. O. Almroth. op. cit., pp. 80–83.

[109] D. O. Brush and B. O. Almroth. op. cit., pp. 90–91.

[110] O. Zienkiewicz and R. Talylor. op. cit., pp. 18–20.

[111] S. S. Rao, *The Finite Element Method in Engineering*. Oxford: Elsevier, 2005.

[112] D. J. Inman. op. cit., pp. 2–22.

[113] H. V. Lakshminarayana, *Finite Element Analysis: Procedures in Engineering*, pp. 14–17. Hyderabad: Universities Press, 2004.

[114] O. Zienkiewicz and R. Talylor. op. cit., pp. 476–479.

[115] M. Petyt, *Introduction to Finite Element Vibration Analysis*, pp. 315–321. Cambridge: Cambridge University Press, 1990.

[116] L. Meirovitch, *Computational Methods in Structural Dynamics*, pp. 183–215. Alphen aan den Rijn: Sijthoff & Noordhoff, 1980.

[117] R. R. Craig, *Structural Dynamics; An Introduction to Computer Methods*, pp. 344–350. New York: John Wiley & Sons, 1981.

[118] A. Curnier, *Computational Methods in Solid Mechanics*, pp. 195–198. Dordrecht: Kluwer Academic Publishers, 1994.

[119] R. Budynas and K. Nisbett, *Shigley's Mechanical Engineering Design*, pp. 395–407. USA: McGraw-Hill, 2006.

Summary

The effect of vibrations on the condition of sensitive canvas paintings has been a major concern for museums and art conservation institutions. Canvas vibrations can produce progressive delamination of cracked paint layers and may cause loss of paint from the canvas. The vibration behavior of the canvas and the delimitation damage produced in the paint are mechanisms which are not well understood and a relation between them has not yet been established. Therefore, many of the precautions and decisions about tolerable vibration levels are based on insufficient knowledge about the nature of the problem in the cultural heritage world.

The objective of this investigation was to develop a model to characterize the vibration behavior of canvas paintings using finite element methods. The mechanical properties of the canvas and paint materials were measured experimentally and determined by semi-empirical methods in order to obtain input material data for the model. The model was used to predict the natural frequencies and mode shapes of canvas paintings with biaxial tension simulating the way it is stretched on a frame. Vibration experiments were carried out in order to measure the natural frequencies and mode shapes of biaxially stretched canvas specimens. The measured natural frequencies and modes were compared to the predicted ones in order to verify and optimize the model.

The results showed that canvas paintings exhibit vibration behavior of thin orthotropic plates with biaxial tension. The natural frequencies of paintings are strongly dependent on the tension present on the canvas. The mass of the layers is the dominant factor contributing to the dynamics of the painting, while the bending stiffness has a negligible effect on the frequencies due to the thinness of the layers. The optimized model was capable of predicting the first two natural frequencies of canvas paintings with sufficient accuracy with differences within 5% compared to the experimental values. The main reasons for the differences between model and experiments were the non-uniform biaxial tension applied in the tests and the simplified material model used for

canvas textiles. Follow-up work is needed in these areas in order to improve the accuracy of the model particularly for higher modes. Further research is also needed to describe the fatigue delamination of paint films in order to provide the cultural heritage world with a complete basis for making decisions regarding the exposure of sensitive paintings to vibrations.

Samenvatting

Het effect van trillingen op de conditie van gevoelige canvas schilderijen is een grote zorg voor musea en instituten voor kunst conservatie. De trillingen van het canvas kan progressieve delaminatie van de gescheurde verflagen en verlies van de verf veroorzaken. De mechanismen van het trillingsgedrag van het canvas en de optredende delaminatieschade in de verf worden nog onvoldoende begrepen en een relatie tussen beide is nog niet vastgesteld. Ten gevolge hiervan zijn veel van de voorzorgsmaatregelen en de besluiten over tolerabele trillingsniveaus gebaseerd op onvoldoende kennis in de wereld van het cultureel erfgoed over de aard van het probleem.

Het doel van dit onderzoek was het ontwikkelen van een model om het trillingsgedrag op canvas schilderijen te beschrijven aan de hand van eindige element methoden. De mechanische eigenschappen van het canvas en de verf-materialen zijn experimenteel gemeten en bepaald door semi-empirische methoden om zo data voor de materiaalinput the verkrijgen voor het model. Het model is gebruikt om de eigenfrequenties en eigenmoden te voorspellen van de canvas schilderijen onder biaxiale spanning dat de manier van gerekt canvas op een frame simuleert. Vibratie-experimenten zijn uitgevoerd zodat de eigenfrequenties en moden op proefstukken van biaxiaal opgespannen doek konden worden gemeten. De gemeten eigenfrequenties en moden zijn vergeleken met hetgene dat voorspeld was zodat het model kon worden geverifieerd en geoptimaliseerd.

De resultaten lieten zien dat canvas schilderijen het trillingsgedrag vertonen van dunne orthotrope platen die onder biaxiale trekspanning staan. De eigenfrequenties van schilderijen zijn sterk afhankelijk van de trekspanning die in het doek aanwezig is. De massa van de lagen is de dominante factor die bijdraagt tot de dynamiek van het schilderij, terwijl de buigstijfheid vanwege de kleine dikte van de lagen een verwaarloosbaar effect heeft op de frequenties. Het geoptimaliseerde model was in staat de eerste twee eigenfrequenties van de canvas schilderijen binnen een 5% afwijking van de experimentele waarden met voldoende nauwkeurigheid te voorspellen. De voornaamste redenen van

de afwijkingen tussen model en experimenten zijn de niet-uniform biaxiale spanning die tijdens de test werd aangebracht en het vereenvoudigde materiaal model dat is gebruikt voor de doeken. Vervolgwerk in deze gebieden is nodig om de nauwkeurigheid van het model te verbeteren, zeker voor de hogere moden. Om in de wereld van het cultureel erfgoed te voorzien met een complete basis voor het maken van besluiten ten opzichte van de blootstelling van schilderijen aan trillingen is er ook vervolgonderzoek nodig om de vermoeiingsdelaminatie van de verffilm te beschrijven.

Acknowledgments

Many memories and emotions arise while writing this final part of my thesis. One realizes the sheer number of people who in one way or another have contributed both intellectually and personally to make this journey such an interesting and enriching learning experience.

I would like to express my sincere gratitude to my promotor: Prof. Rinze Benedictus for welcoming me in such an extraordinary group. Thank you for your wise guidance and support while at the same time giving me the trust and freedom to find my path and develop my skills as a researcher.

This project would not have been possible without the invaluable guidance of my daily supervisor Bill Wei. Bill, thank you for having confidence in me and supporting me all the way. More than a supervisor, you have been a mentor and a friend. I will be forever grateful for all of the things that you have taught me not only in the realm of science but also professionally and personally.

My sincere thanks also go to Jan Hol and Eelco Jansen from the Aerospace Structures group. Mr. Hol, thank you for welcoming me in your student room at the beginning of the project and for teaching me so much about finite elements. Eelco, thank you for imparting your knowledge on vibrations and for your useful feedback about my research.

A key figure in the Structural Integrity Group is Ms. Gemma van der Windt. Thank you Gemma for all of your help with administrative issues and for making things happen in such an efficient way. Your personality and positive attitude bring a good vibe to the group.

There were many people that made the experimental part of my research possible. I would like to express my sincere appreciation to the technicians: Kees, Hans, Berthil, Bob, Frans and Niels from the Structures and Materials Lab, for their assistance and outstanding practical expertise. I am particularly grateful to Roger Groves and Dênis Goto from the Optical Non-destructive Testing Lab for their assistance with the setup for shearography measurements. Many thanks to Kaspar Jansen and Jan de Vreugd from the Precision and

About the Author

Patricio Gabriel Chiriboga Arroyo was born on August 28, 1981 in Quito, Ecuador. He attended primary and secondary school in his hometown at Liceo Internacional, graduating in 1999. He then started his studies in Mechanical Engineering at Escuela Politécnica Nacional University in Quito. After his graduation in the summer of 2006, he was awarded with a Marie Currie Actions fellowship on the project EPISCON – European PhD in Science for Conservation. The project started with a six-month training program in cultural heritage conservation at the University of Bologna in Ravenna, Italy. In February 2007, Patricio moved to the Netherlands to work on his PhD project: "Finite Element Modeling of Vibrations in Canvas Paintings" under daily supervision of Dr. ir. W. Wei at the Instituut Collectie Nederland (ICN), EPISCON partner institution in Amsterdam. In September 2009, Patricio joined the Structural Integrity Group in the Faculty of Aerospace Engineering at the Delft University of Technology to continue his PhD research under the supervision of Prof. dr. ir. R. Benedictus. From June 2011 to November 2012, Patricio worked at DAF Trucks as a Noise Vibration & Harshness Test Engineer at the Engine Development Department in Eindhoven.

Preventing vibration damage from occurring to valuable and sensitive canvas paintings is of main concern for museums and art conservation institutions. This concern has grown in recent years due to the increasing demand of paintings for exhibitions worldwide and the concomitant need for their handling and transport. The vibration of the canvas can produce progressive delamination of cracked paint in aged paintings which may cause paint loss after repetitive vibration exposure. In the cultural heritage world, there is limited knowledge about the vibration behavior of the canvas and its relation with the damage produced in the paint. The goal of this investigation was to improve this understanding about the vibration behavior of canvas paintings through the use of finite element modeling. A model was developed with the capability of predicting the natural frequencies and mode shapes of canvas paintings, and providing a fundamental understanding of the parameters that influence their dynamic behavior. Canvas paintings exhibit vibration behavior of thin orthotropic plates dominated by the tension and mass of the canvas with negligible bending stiffness. The model was verified and optimized experimentally using a specially designed vibration testing system for canvasses, showing differences within 5% between the first two predicted and measured natural frequencies. Follow-up work to study the non-uniform biaxial tension and to improve the canvas textile material model is needed in order to improve the accuracy of the vibration model for higher modes. Further research is also required to better understand the delamination of paints due to vibration (cyclic) loading. Combined with this model, this will better assist museums and conservators taking precautions and making decisions about vibration exposure and tolerable levels.

TU Delft

Rijksdienst voor het Cultureel Erfgoed
Ministerie van Onderwijs, Cultuur en Wetenschap